AD-A269 999

DEFORMATION, FRACTURE
AND EXPLOSIVE PROPERTIES
OF REACTIVE MATERIALS

Principal Investigator: Dr J E Field

EUROPEAN RESEARCH OFFICE

United States Army
London W1, England

Contract No. DAJA 45-90-C-0025
Final Report June 1993

Physics & Chemistry of Solids
Cavendish Laboratory
University of Cambridge
Madingley Road, Cambridge. CB3 0HE, UK

1

REPORT DOCUMENTATION PAGE

Form Approved
OMB No. 0704-0188

1a. REPORT SECURITY CLASSIFICATION		1b. RESTRICTIVE MARKINGS
UNCLASSIFIED		
2a. SECURITY CLASSIFICATION AUTHORITY		3. DISTRIBUTION / AVAILABILITY OF REPORT
2b. DECLASSIFICATION / DOWNGRADING SCHEDULE		APPROVED FOR PUBLIC RELEASE; DISTRIBUTION UNLIMITED

4. PERFORMING ORGANIZATION REPORT NUMBER(S)	5. MONITORING ORGANIZATION REPORT NUMBER(S)
	R & D 6499-AN-01

6a. NAME OF PERFORMING ORGANIZATION	6b. OFFICE SYMBOL (If applicable)	7a. NAME OF MONITORING ORGANIZATION
UNIVERSITY OF CAMBRIDGE		USARDSG-UK

6c. ADDRESS (City, State, and ZIP Code)	7b. ADDRESS (City, State, and ZIP Code)
CAVENDISH LABORATORY, MADINGLEY ROAD, CAMBRIDGE, CB3 0HE, UK	PSC802 BOX 15 FPO AE 09499-1500

8a. NAME OF FUNDING / SPONSORING ORGANIZATION	8b. OFFICE SYMBOL (If applicable)	9. PROCUREMENT INSTRUMENT IDENTIFICATION NUMBER
USARDSG-UK	AMXSN-UK-RA	DAJA45-90-C-0023

8c. ADDRESS (City, State, and ZIP Code)	10. SOURCE OF FUNDING NUMBERS			
PSC802 BOX 15 FPO AE 09499-1500	PROGRAM ELEMENT NO.	PROJECT NO.	TASK NO.	WORK UNIT ACCESSION NO.
	61103A			

11. TITLE (Include Security Classification)

DEFORMATION, FRACTURE AND EXPLOSIVE PROPERTIES OF REACTIVE MATERIALS

12. PERSONAL AUTHOR(S)
JOHN FIELD

13a. TYPE OF REPORT	13b. TIME COVERED	14. DATE OF REPORT (Year, Month, Day)	15. PAGE COUNT
FINAL	FROM MAY 92 TO MAY 93	JUNE 1993	66

16. SUPPLEMENTARY NOTATION

17. COSATI CODES			18. SUBJECT TERMS (Continue on reverse if necessary and identify by block number)
FIELD	GROUP	SUB-GROUP	EXPLOSIVE, IGNITION, IMPACT, SENSITIVITY, HOT SPOTS, HIGH SPEED PHOTOGRAPHY, OPTICAL TECHNIQUES, DEFORMATION FRACTURE, PBX's, PROPELLANT
	01		
	09		

19. ABSTRACT (Continue on reverse if necessary and identify by block number)

A range of optical techniques, based on moire and speckle, have been developed at Cambridge for studies of the deformation, strength and fracture properties of materials including PBXs and propellants. In some cases, these high spatially sensitive methods (micron resolution) have been combined with high speed photographs (microsecond timing intervals). A review paper has been prepared for the 10th Detonation Symposium and this is given as Appendix 1. Section 2 describes a study of the deformation of inert propellant grains; cylinders with seven axial holes. The grains were stressed to failure in three geometries. The optical technique chosen for the study was the "fine grid" method. An important advance was the development of methods to add a fine grain grid to the surface of the grains (spatial period 80 μm). The results show the detailed deformation, for the whole viewed surface, up to failure. Section 3 is concerned with fragment attack of propellant grains. A gas gun has been used to fire projectiles of various shapes into different arrays and types of propellant grains; the whole process is recorded with an image converter camera at microsecond framing intervals. The results show the way the propellant deforms and the sites at which any ignition takes place. This report presents results on uncased propellant. Appendix 2, a preprint of a paper presented at the 10th

20. DISTRIBUTION / AVAILABILITY OF ABSTRACT	21. ABSTRACT SECURITY CLASSIFICATION
☐ UNCLASSIFIED/UNLIMITED ☐ SAME AS RPT. ☐ DTIC USERS	

22a. NAME OF RESPONSIBLE INDIVIDUAL	22b. TELEPHONE (Include Area Code)	22c. OFFICE SYMBOL

DD Form 1473, JUN 86   Previous editions are obsolete.

19. ABSTRACT continued:

Detonation Symposium, gives results on cased propellant. Finally, Section 4 gives recent results obtained with our transparent anvil drop-weight apparatus. This technique allows high-speed photographic recording of layers of propellant or arrays of propellant grains being impacted. Data are presented for four propellants.

Accesion For		
NTIS CRA&I	☑	
DTIC TAB	☐	
Unannounced	☐	
Justification		
By		
Distribution /		
Availability Codes		
Dist	Avail and / or Special	
A-1		

DTIC QUALITY INSPECTED 1

1. INTRODUCTION

A range of optical techniques, based on moiré and speckle, have been developed at Cambridge for studies of the deformation, strength and fracture properties of materials including PBXs and propellants. In some cases, these high spatially sensitive methods (micron resolution) have been combined with high speed photographs (microsecond timing intervals). A review paper has been prepared for the 10th Detonation Symposium and this is given as Appendix 1. Section 2 describes a study of the deformation of inert propellant grains; cylinders with seven axial holes. The grains were stressed to failure in three geometries. The optical technique chosen for the study was the "fine grid" method. An important advance was the development of methods to add a fine grain grid to the surface of the grains (spatial period ~ 80 μm). The results show the detailed deformation, for the whole viewed surface, up to failure. Section 3 is concerned with fragment attack of propellant grains. A gas gun has been used to fire projectiles of various shapes into different arrays and types of propellant grains; the whole process is recorded with an image converter camera at microsecond framing intervals. The results show the way the propellant deforms and the sites at which any ignition takes place. This report presents results on uncased propellant. Appendix 2, a preprint of a paper presented at the 10th Detonation Symposium, gives results on cased propellant. Finally, section 4 gives recent results obtained with our transparent anvil drop-weight apparatus. This technique allows high-speed photographic recording of layers of propellant or arrays of propellant grains being impacted. Data are presented for four propellants.

2. DEFORMATION OF INERT PROPELLANT GRAINS

2.1. Introduction
The objective of the work described in this report was to develop and apply a suitable optical technique to determine the in-plane displacement fields associated with the quasi-static compressive deformatio 1 of inert propellant grains up to the point of failure.

2.2 Experimen' il
The propellant , rains are cylinders with typical dimensions of 7.4 mm in diameter by 8.0 mm in length containing seven perforations, with diameters of about 0.7mm aligned parallel to the long axis of the cylinder, six arranged in a hexagonal array together with a perforation through the centre of the grain.

Individual grains were loaded in compression between a fixed and a moving brass anvil in an Instron 1122 Universal testing machine with crosshead speeds of 0.05 and 0.20 mm/min. The applied load was measured with a tension/compression load cell with a maximum load capacity of 500 kg. In two of the loading configurations individual grains were compressed across their diameters with the three perforations along the grain's diameter aligned either parallel or perpendicular to the axis of loading. In the remaining configuration the propellant grain was axially split along three diametrial perforations and mounted with the long axis vertical.

Previous work has shown that under quasi-static compression the grains deform plastically before fracturing. The in-plane displacements up to the point at which the

grain fractures are quite large, typically up to ~ 1mm. In view of these large displacements, the optical technique chosen was based on the "Fine Grid" method. In this technique a crossed grating with a suitable pitch is created on the surface of the specimen. The deformation of the grating is monitored whilst the sample is loaded and the data obtained is then used to determine the in-plane displacement fields. The experimental arrangement used to monitor the deforming grating and the methods used to process the data are described more fully in section 2.2c.

2.2a Specimen preparation

A convenient method of producing a crossed grating pattern on the surface of a propellant grain containing perforations, is by stenciling using a fine mesh A stencilled pattern was created using a 25 μm thick electroformed nickel mesh, with a mark to space ratio of 1:4 and spatial period of 76.3 μm. The surfaces of the propellant grains were prepared by first hand grinding to produce flat faces using wet and dry paper, followed by polishing with a 12 μm white ceramic grit to obtain a smooth surface free from protuberances, for example raised edges around the perforations, as these can produce gaps in the stencilled pattern where displacement data can not be obtained. The split-grain specimens were prepared in the same manner, after the grains had been cut with a diamond saw. The axial perforations through the length of the cylinder were carefully exposed in the hand grinding process, followed by polishing as described above.

A high contrast stencilled pattern is required if the the lines of the grating are to be easily resolved by an imaging system. The specimen surface was first sprayed with a black liquid acrylic paint through a airbrush photographic retouching pen. After allowing the paint to dry a second layer was then applied, whilst the paint was still wet a small square of the mesh is laid gently on the specimen surface, after being oriented with respect to the perforations with the aid of a high magnification stereo microscope. The application of the mesh to the specimen surface must be done very carefully in order to avoid the wet/damp layer of acrylic paint flowing into the spaces of the mesh and thereby blocking them. The purpose of the latter step was to adhere the wire of the mesh to the specimen surface in order to prevent subsequent paint sprayed through the spaces from spreading underneath the mesh and destroying the pattern. The specimen with the mesh in place was then allowed to dry. Finally white acrylic paint was sprayed through the mesh using as fine a spray as possible with the airbrush to minimise wetting the stencil. This process was repeated several times, in which successive layers were allowed to dry before applying the next. When the surface appeared completely white the mesh was gently removed by lifting it away at one corner. The stencilled pattern was then revealed as white blocks of paint against a black background.

2.2b Photographic studies

Initial experiments to test the effectiveness of the grating in revealing the deformation of propellant grains under load, were performed using a conventional 35 mm camera system. An Olympus OM 2 camera and motor drive, together with a 50 mm F/3.5 Zuiko Macro lens and extension bellows were used to image the specimen onto FP4 (iso 125) black and white film. The image of the specimens were magnified by typically 2.8× for the circular face configurations, and 2.3× for the split-grain configuration. Photographic frames were recorded, whilst the sample was being loaded, with automatic exposure after which the film was advanced to the

next frame by the motor drive. The specimen was illuminated obliquely with an Olympus white light source. As this light source can produce significant heating at the surface of the object over the duration of the experiment, a heat filter was used to prevent heating of the sample.

The alignment of the crossed specimen grating with the axis of loading for the circular face configuration was achieved by removing the loading jig containing the brass anvils, from the Instron and placing it under a travelling microscope. The stencilled surface of the sample was then moistened by pressing against a damp absorbent tissue and attached to a small glass plate where it was held in position by surface tension forces.

The specimen could then be introduced into the space between the anvils and the horizontal grating lines aligned parallel to the fixed anvil by rotating the glass plate whilst being observed through the travelling microscope. The sample was then held firmly in position between the anvils by means of a spring which applied a small compressive load to the sample. The the jig was then replaced in the Instron. Using this method it was possible to align the specimen grating to within an uncertainty of one grating pitch over a sample diameter, corresponding to an angular error of ±0.3 degrees.

2.3c Image processing system studies

The method chosen to analyse the images obtained as described is derived from the "Fine Grid Method", in common use by engineers. The image of the crossed grating described above is used to provide a series of markers, the movement of which is traced by a computer. The computer can then map the deformation across the whole of the surface of the sample.

The apparatus used is illustrated in figure 2.1. The sample is loaded as before in an Instron tensometer. A video camera is arranged with suitable optics to record images of the deforming sample. The output from the camera can be digitised on demand at intervals to provide a permanent record of the specimen from time to time. An inter-frame time of about 30s was found to be adequate, dropping to as little as 10s when the specimen begins to yield rapidly. The output from the load-cell of the testing machine is also digitised and recorded, but at a frequency of once per second. The computer in use is a Sun SPARCstation II (20 MIPS, 4.2 MFLOPS), with a Digital Imaging Systems DIS-3000 frame-grabber, an EEV P46580 CCD video camera, and a Biodata Microlink analogue-to-digital converter. Experiments have been carried out on samples in configurations I and II of the sample (described in section 2.3a), but not of the split grain-geometry, configuration III.

The method chosen for the analysis uses a suite of pre-existing programs written in-house to perform various image-processing tasks, as well as several purpose-written programs.

The images are processed according to the following scheme. Along each axis, the intensity of the image will vary as a square wave if the grating is perfect. This can be approximated as a sine wave if necessary. If we plot a graph of intensity against pixel location, along, say, a line parallel to the horizontal axis, we can represent the intensity variation as a sine-wave. Thus we could use as a measure of distance along this sine-wave, the "phase" of the wave, which will increase by 2π per grating pitch. This phase will then give a measure of position on the surface of the sample along the line we have been measuring. The same phase value will always correspond to the same point on the surface of the specimen, regardless of how the grating

deforms, so long as it remains resolvable, and provided we always start counting phase at the same place.

However, in the image, each time the phase increases past 2π, the phase will return to zero. The phase is said to be "wrapped" on to the space 0 to 2π. To provide a monotonically increasing measure of distance across the specimen surface, the phase must be "unwrapped". This is performed using algorithms described by Huntley.

If we extend this argument to two dimensions, we can produce a map of phase increasing in the $+x$ direction, and a separate map of phase increasing in the $+y$ direction. If the sample deforms, then we can follow the movement of every point on the specimen surface by locating a point with identical x and y phase in a subsequent frame, and calculating the movement which has occurred between the two frames. Thus the deformation can be determined across the whole specimen surface.

The x and y components are separated by performing a two-dimensional fast-Fourier transform on the image, and spatially filtering either the x or the y component of the grating before performing an inverse Fourier transform, and then unwrapping the phase in each direction.

Since this method effectively counts every square in the grating on the specimen surface, it is essential that the grating is of very high quality. If single blocks are missing, or contrast is low in some regions, the unwrapping process gives ambiguous answers, and the method fails. It is thus essential to show that the gratings in use are of adequate quality.

Figure 2.2 shows a set of six images recorded by the computer during loading in configuration I. Consider the example of frame (a), where the sample is undeformed. This picture is produced from the digitised image. After spatial filtering, and phase unwrapping the x component of the phase, is shown as a contour map in figure 2.3a. This can be seen to be composed of straight lines, stretching from phase 0 on the left (chosen arbitrarily) to about 600 on the right, corresponding to just under 100 lines on the specimen surface. The same procedure can be performed on the y component of the phase, yielding a similar contour map, illustrated in figure 2.3b If the method is to be successful, it must also be possible to draw unambiguous unwrapped phase maps of the deformed specimens . Using frame (f) of figure 2.2, the same processing has been performed, to yield the contour maps shown in figures 2.3c and 2.3d. Here the contours are curved, to mirror exactly the deformation of the grid on the specimen surface. There are some discontinuities in the contour maps, where the specimen has failed, however this is to be expected in regions close to tears in the specimen surface.

The final stage of writing a program which will enable the phase maps to be followed from frame to frame, tracking a given x, y pair of phase values at each pixel as they move across the image is yet to be completed. It should then be possible to evaluate the in-plane strain fields over the whole specimen surface. The feasibility of the method, which is critically dependent on being able to produce very high quality, high contrast gratings has been amply demonstrated. The additional software required is under development, and is expected to be completed soon.

The load-time curves produced from these experiments have been recorded. Two such curves are plotted in figure 2.4, where the continuous line represents the data from an experiment with the specimen aligned in configuration I, in which the load was measured every second, the discrete points are from a second experiment, where load was measured at the times when an image was digitised. It can be seen that they are in very good agreement. The load-time curve for a sample loaded in

configuration II is shown in figure 2.5. Six of the images recorded by the computer in this experiment are illustrated in figure 2.6.

2.3. Results

2.3a Photographic studies

A sequence of six photographic frames showing the deformation and compressive failure of a propellant grain with three perforations aligned parallel to the loading axis, configuration I, is shown in figure 2.7. The initial sample dimensions were 7.38 mm in diameter by 8.19 mm in length. Photographs were recorded at F/8.0 with automatic exposures, as the sample was loaded at a constant rate of 0.05 mm/min. In this configuration all the perforations become increasingly distorted as the loading continued and appeared initially to start at the boundaries of the perforations closest to the anvils, as shown by the curvature of the grating lines in this region. As the loading continued, these perforations were deformed into triangular shaped holes with rounded vertices, whereas the central perforation became increasingly ellipitical in shape. The remaining perforations away from the loading axis, were distorted into increasingly pear drop shaped holes. The corners of the deformed perforations became sharper as the load was slowly increased to a maximum value of 116 kgs, corresponding to figure 2.7(e), after which the load steadily decreased as the sample was further compressed. The decreasing load coincided with the onset of failure, which can be clearly seen in figure 2.7(f), where cracking can be seen starting from the sharp corners of the central perforation. In addition there is also evidence of shear failure along directions connecting the corners of the triangular holes at the top and bottom of the grain adjacent to the pear shaped holes.

In the second configuration three perforations were aligned parallel to the horizontal axis. This sample was again loaded at a constant crosshead speed of 0.5 mm/min. A sequence of six photographs showing the deformation and failure is shown in figure 2.8. In this configuration, the two outermost perforations on the horizontal axis appear to have remained almost undeformed or distorted as shown in figure 2.8(f). By contrast the central perforation is distorted from a circular hole into an almost retangular hole with rounded corners. This sample reached a maximum loadof 87 kgs, corresponding to figure 2.8(e), at which point the load decreased steadily as the grain was further compressed. As in the previous example the decreasing load coincided with the onset of failure. Close inspection of figure 2.8(e) shows the formation of shear cracks along the directions connecting the top left and bottom right corners of the central hole with the adjacent pear shaped holes located at the top left and bottom right of the sample. These cracks are more clearly shown in figure 2.8(f).

The deformation and compressive failure of a split propellant grain is shown in the sequence of six photographs presented in figure 2.9. The initial specimens were 7.75 mm in height by 7.35 mm in diameter corresponding to the unloaded grain shown in figure 2.9(a). The sample was loaded at a constant crosshead speed of 0.05 mm/min. From the sequence it can be seen that as the sample is compressed the perforation walls are bent outwards. In addition at the mid-point height the spacing of the horizontal grating lines became successively smaller until they could not be resolved. This was partly due to an out of plane displacement of the grain, however examination of the specimen after loading,showed that the reduced spacing of the

grating lines at the mid-height was a real effect. In contrast the sequence shows that the grating appears to have undergone relatively little deformation immediately underneath the anvils. At a load of 134 kgs, corresponding to figure 2.9(f), the load started decreasing as the sample was compressed. As before, this co-incided with the onset of failure which in this case occurred in the form of axial cracking of the grain, at the rear mid-height of the perforations. At failure the bulk compressive strain was estimated as approximately 60%.

2.4. Discussion

The results obtained to date show that it is possible to produce crossed gratings of sufficiently high quality and contrast to allow the deformation of the propellant grains up to the point of failure to be established. The photographic studies have shown that there appear to be regions within the deforming grain in which the material behaves in an almost rigid manner. Such regions appear to be located in the vicinity of the loading anvils. This is particularly evident in the deformation of the grains in the configuration II arrangement, in which the central perforation is changed from a circular into a rectangular hole as the grain is compressed. It appears to be possible to liken the deformation to the insertion of rigid wedges into the grain from above and below the grain where it is in contact with the anvils. Such "dead zones" may be typical of this loading geometry. These observations are common to several experiments, not all of which are presented here.

To date all data relating to the deformation of the grains has been extracted by visual analysis either of the developed photographs from the photographic studies, or of computer-generated animation sequences. Whilst this has given a very good qualitative insight into the deformation processes, the real objective is to analyse these pictures to obtain the in-plane displacement fields by using the fine-grid method. It has been shown that the gratings and optical arrangement are of sufficient quality to allow the extraction of the relevant data. The final processing of this data has not yet been achieved, but the principle has been amply demonstrated. Further work to produce animated sequences of strain distributions within the deforming grain offers the prospect of excellent results in the very near future.

3. SIMULATED BULLET ATTACK OF SOLID GUN PROPELLANTS

3.1 Introduction

Much research is currently being undertaken into the hazard response of propellant materials to bullet or fragment attack. No longer is the explosive filling of a munition considered to be the only part sensitive to accidental or intentional fragment attack; the propellant component has been found to be similarly vulnerable. Unfortunately, at least from the point of view of minimizing hazard response, propellant is *designed* to burn and may do so after a stimulus that will not induce any response in an explosive filling. In general, the shock-to-detonation transition ("SDT") is less of a potential hazard with conventional gun propellants than for explosive fillings though the trend towards low vulnerability (LOVA) compositions for gun propellants which often include secondary high explosives as part constituents prevents this from being an assertion. The concept behind including explosives in propellant compositions is, perversely, to reduce their vulnerability whilst ensuring similar or greater performance. The resulting compositions can be less sensitive to burning stimuli but, as the proportion of

explosive is increased, the composition can become more susceptible to stimuli capable of producing SDT. In addition, should a propellant charge in the form of loose packed grains, aligned sticks or cast motor be caused to burn accidentally, the effect this may induce in the other components of the munition may be just as catastrophic as if the high explosive itself had suffered an initiating stimulus. To a large extent, the lower susceptibility to burning exhibited by the LOVA propellants has been the impetus behind this compositional research as the common single, double or triple based propellant compositions are very vulnerable under this type of unintentional stimulus.

Much of the work now concentrates on designing the propellant material *and* the casing as a combination. This has allowed well-characterised propellant materials to be hazard tested and the effects of casing changes easily discernible.

The aim of the experiments detailed in this report was to compare the ignition response of four gun propellants (though the technique could be used to assess the impact response of any type of propellant) to a simulated bullet attack. The compositions were impacted to identify the prevalent ignition mechanisms and the subsequent propagation of reaction using either a sabot-driven metal projectile or a nylon projectile.

In addition to single grain impacts, most of the compositions were tested in geometric arrays representing one layer of close-packed and one layer of column stacked array. These experiments were to determine the effect that packing has on the hazard response of the material. In some munitions, the geometric packing of the grains is carefully controlled (eg. strand burning rocket motors) and in others, the propellant grains are allowed to adopt any orientation.

Unlike earlier work carried out by the author into sectioned, cased explosive charges, (Ref Appendix iii), the compositions were not cased as it was thought that there would be considerable difficulty in manufacturing good-fit cases and keeping the propellant quantity between tests uniform. In addition, the impact geometry would not be so well known since some impacts could occur fully through casing onto a grain, whilst others could occur through the casing but at the intersticies between grains thus reducing the effect of the impact and making the outcome mechanistically uncertain.

The mechanisms envisaged to play a role in the ignition of propellants which are uncased and subject to simulated bullet attack by projectiles are heating due to rapid viscous flow ahead of the projectile, adiabatic shear band formation and, in the case of the multi-cored propellants under test, heating of the propellant by shock induced adiabatic collapse of the holes. Walley and co-workers (1992), after studying high-speed photographs of the rapid deformation of cast double-based propellants under drop-weight impact, suggested that ignition occurs through additive processes such as bulk heating, viscous heating and adiabatic heating of gas trapped at the peripheries of the specimen leading to "hot spot" production. Fong (1985), using a Hopkinson Bar arrangement, investigated crack initiation in multi-cored propellants by impacting the grains side- and end-on and found that single- and triple-based propellants were more resistant to crack initiation than double-based propellants. II also suggested that the holes were sites of localised stress. Goldrein and co-workers (1993) also found, by analysing contour plots of in-plane displacements, that there are stress concentrations *between* these holes. Work by Boyle *et al.* (1989), showed that both pressure and shear velocity have a strong effect on ignition and that in their experiments on a range of explosives and propellants, the composite-

modified, double-based propellant was by far the most susceptible to shear forces but the least sensitive to shock. Further work on ignition mechanisms has been carried out by Ho and Fong (1989) who investigated the relationship between impact ignition sensitivity and the kinetics of thermal decomposition of solid propellants. They suggested that two distinct mechanisms are involved in impact ignition. Firstly, there is an initiation step where fracture, visco-elastic/plastic deformation and cracking occur and are the means by which "hot spots" are formed; the mechanical properties of the propellants predominate in this step. Secondly, there is a flame propagation step which is governed by several inter-related factors such as the decomposition kinetics, thermal stability and burning rate of the propellant i.e. propellants with low decomposition temperatures and low activation energies showed high ignition sensitivities.

In this study, high-speed photography has been used to give an insight into the reactiveness of four types of gun propellant under simulated bullet attack and in addition has compared solid gun propellant with that of its multi-cored equivalents..

3.2 Experimental

The samples of propellant were impacted using two types of projectile. (See Table 3.1) The silver-steel projectiles, (density 7.8 g cm^{-3}) were sabot-driven to allow relatively small diameter projectiles to be used so that the mass of propellant was kept to a minimum to comply with safety constraints. The sabots were made of nylon 666 rod (density 1.1 g cm^{-3}), with a recess for the projectile at the front and material reamed out at the rear to reduce the weight of the combination. The projectiles were fired at the target at velocities of 400 to 580 m s^{-1}. Although the sabot would impact the target approximately 15 μs after the projectile, it was not expected to affect the initial mechanisms that might cause ignition in the propellant. However, early high-speed photographs for this work showed that the subsequent impact of the sabot had, in some cases, a considerable effect on the later ignition response and it was decided to also investigate the effect of this second shock on the propellant grains. Nylon projectiles were used because of their good impedance matching with the target and light weight. which permitted high impact velocities at relatively low firing pressures. The nylon projectiles were fired at between 600 and 720 m s^{-1}.

Table 3.1. *Type, front-end geometry and dimensions of projectiles*

Projectile material	front-end geometry	diameter (mm)	length (mm)	mass (g)
silver steel	flat	5.2	16	2.6
silver steel	30° cone*	5.2	20	2.3
nylon 666	flat	12.75	25	2.2

* used in JA2 experiments only

There were four types of experiment performed on the propellants:-

(i)   steel projectile impact on a single grain
(ii)   nylon projectile impact on a single grain
(iii)   steel projectile impact on a close-packed array of grains
(iv)   steel projectile impact on a "columned" array of grains

Steel projectile experiments

The steel projectile impact on the arrays and single grains was carried out on 6 mm thick parallel-faced cylinders. Sectioning and facing marks can be seen on some of the materials. The grains were sandwiched between two 10 mm thick blocks of polycarbonate as shown in Figure 3.1. The thickness of the propellant for the steel projectile impacts allowed the blocks to act as sabot-strippers. The effect of the sabot has been discussed earlier. Figure 3.1 is a picture of the target arrangement and Figure 3.2, a picture of the target in the experimental set-up.

Nylon projectile experiments

The nylon projectile impacts were carried out on single grains of the propellants which were sectioned to be 11 mm thick. The dimensions of XM43m (refer to Table 3.2) prevented the single grain impacts from being readily carried out. The propellant types, dimensions and geometries are detailed in Table 3.2 and are shown for comparison in Figure 3.3.

Table 3.2. Type, dimensions and geometries of the propellant.

Propellant	Type	Geometry tested	diameter(mm)	length (mm)
JA2	standard double base	solid stick	8	as required
XM43	nitramine based	solid stick	8	as required
JA2 equivalent	standard double base	7 holes	9	as required
XM43 equivalent	nitramine based	7 holes	5	11

The two multi-cored propellants have been referred to as JA2m and XM43m. The dimensions of the US and the equivalent multi-cored propellants are not exactly similar because in general, propellants are designed and manufactured with a specific use in mind. It was therefore very difficult to obtain multi-cored propellants that were exactly the same diameter as the solid sticks. The chemical compositions of the US propellants and their equivalents are however very similar.

The projectiles were fired using a helium-driven, single-stage gas-gun at pressures of between 20 and 50 bar, which produced velocities (depending on the projectile used) of between 400 and 720 m s^{-1}. The impacts were photographed using an IMACON 792 image converter camera in framing mode, with interframe times of either 2 or 5 μs.

The photographs were lit using Bowen flashes and arrangments of front and rear lighting as appropriate. The velocity of the projectile was measured by timing it between two laser beams a known distance apart. The timer was connected to an up-down counter which was used to fire the camera at the correct time, irrespective of projectile velocity. The experimental layout is presented schematically in Figure 3.4.

3.3 Results
In this section, each material has been analysed in turn.

JA2 Gun propellant
Under steel projectile impact of a single grain, at up to 550 m s⁻¹, this material did not ignite on penetration by the projectile. In a few photographs there is some evidence of burning on sabot impact but as most of the propellant was retrieved, if in many fragments, bulk ignition presumably did not occur.
For the nylon projectile impact at velocities up to 670 m s⁻¹, there was no evidence of ignition.
These results are interesting as they suggest that the material is intrinsically insensitive to this type of impact and is also relatively insensitive if fractured (on projectile penetration) and then subsequently re-shocked by the following sabot.
The results are however significantly different for arrays of grains under projectile attack.
Fig. 3.5 shows steel projectile (p) impact of a close-packed array of JA2 at 575 m s⁻¹ with impact occurring in frame 1. The interframe time is 5 µs and it can be seen that the first impacted grain underwent considerable deformation resulting in ignition ahead of the projectile and in the surrounding interstices. On sabot (s) impact in frame 3, there is further reaction which builds in intensity in the subsequent frames until dying away after 35 µs, frame 8 (not shown). Although there has clearly been ignition in some of the grains, propagation between all the grains did not occur as some were recovered relatively undamaged. This could be due to the confinement of the system allowing movement of the more distant grains after approximately 30 µs and preventing further propagation of reaction or it could simply be due to the material being fragmented and ejected from the reaction zone.
Figure 3.6 shows a close-up of steel projectile (p) impact of a close-packed array at a faster framing rate with 2 µs interframe time. The impact was at 540 m s⁻¹, slower than for figure 3.5, and there does not seem to be ignition associated with projectile impact, though the initial impact grain (g) undergoes much plastic deformation, swelling to fill the interstices. As the grain boundaries came together, there was also no observed ignition. Further experiments at between 510 and 570 m s⁻¹ suggest that this result was on the border-line for ignition to occur for this array geometry. In other recent studies by the author into a different double-base composition, this plastic deformation to fill the available space has also been observed though again there was no ignition on grain boundary impact. There *is* light ahead of the projectile in frames 4 and 5, but further experiments and examination of the confining polycarbonate blocks after the experiment has shown that this is due to the steel projectile scoring the blocks rather than ignition of the propellant itself. Ignition *does* occur in frame 8 and the partly visible frames 9 and 10 though there does not seem to be bulk ignition or propagation of reaction between the propellant grains. This ignition is probably sabot-impact associated as clearly the shock imparted by the sabot into already fractured and heated propellant could cause ignition. Once again, some grains were retrieved after the experiment, showing little signs of damage and no signs even of surface burning.
Figure 3.7 shows pointed-ended projectile (p) impact of a close-packed array at 550 m s⁻¹ and there is no ignition associated with the projectile impact in frame 1. The interframe time is 5 µs. It is interesting to note that the material has been sufficiently disturbed and probably heated by this impact to ignite on the following sabot

11

impact in frames 5 and 6 though the ignition is neither as sustained nor as violent as has been observed with flat-ended projectile impacts at the same impact velocity. The sabot (s) can be seen to light up in frame 4, just at the moment of impact with the blocks. This is probably caused by adiabatic compression of the air trapped under the sabot on impact. These impact results suggest that the propellant is fairly sensitive after being fractured as a pointed-ended impact does not produce as much rapid flow ahead of the projectile as is the case with a flat-ended projectile impact. The amount of viscous and shear heating experienced by the propellant is also greatly reduced. Earlier studies by the author into cased explosive compositions and other propellants have found that some materials remain almost as insensitive after pointed-ended projectile impact as the un-impacted material and are consequently unaffected by the shock produced in the material by the following sabot impact.

It should be remembered that *no* ignition is seen in the propellant for single grain impacts with flat-ended projectiles even on the following sabot impact and that JA2 remains insensitive to faster nylon projectile impact although this should produce a stronger shock in the material than a sabot following a projectile.

Figure 3.8 shows steel projectile (p) impact of a columned array of JA2 at 540 m s^{-1} with a 5 μs interframe time. Although there is projectile yaw, causing the impact to be high in frame 1, luminescence can immediately be seen in frame 2. Jetting of the material is visible around the projectile and on sabot (s) impact in frame 4, bulk ignition occurs in the interstices and in the grains themselves. In frame 5, jetting (j) of material can be seen emanating from between two grains. In this and other experiments with these columned arrays, little material was recovered and there were no intact grains.

JA2m multi-cored Gun Propellant

Under steel projectile impact of a single grain at up to 550 m s^{-1}, ignition was observed at 540 m s^{-1} and above. The ignition is again sabot-associated; compression of the holes on projectile impact is observed but not luminescence. It is possible that luminescence was missed because of the 5 μs interframe time as this type of collapse is followed better with a faster framing rate. On the following sabot impact, adiabatic compression of the holes nearest the impact is observed, followed by rapid fracturing of the grain between the holes and subsequent burning of the whole grain. No material was recovered.

Under the faster nylon projectile impact at up to 705 m s^{-1}, ignition was observed starting at the hole nearest the impacting projectile and leading to burning of most of the propellant grain. A small percentage of the material was recovered after these tests.

These results suggest that although JA2 and JA2m are compositionally very similar, the geometry of the grain has an important effect on its sensitivity to ignition under projectile attack. JA2m seems more sensitive under single grain impact.

Studies of this material impacted in arrays also shows increased sensitivity as compared to standard JA2.

Figure 3.9 shows a close-packed array of JA2m undergoing steel projectile (p) impact at 520 m s^{-1}. Impact occurred in frame 1 and burning between the interstices can be seen beginning in frame 1 and increasing in frame 2, 5 μs later. On full sabot (s) impact in frame 3, much greater reaction is observed and luminescence occurs in the hole (h) closest to the impact site due to adiabatic compression of the gas in that hole. The projectile does not hit squarely on impact and it is suggested that material

is scraped or sheared off into the interstices where it burns. This material would have absorbed much of the energy of impact and could be expected to have been rapidly heated in the process. Ignition continues in the later frames though some material was recovered after the test.

Figure 3.10 shows a columned array of JA2m impacted by a steel projectile (p) at 540 m s^{-1}. The interframe time for this picture was 5 μs. Projectile impact occurred in frame 1 and there does not seem to be ignition associated with this impact or the following sabot (s) impact in frame 3. In frame 5 luminescence is observed emanating from the holes (h) in the grain impacted first and bulk ignition has occurred by frame 6, increasing in intensity in the subsequent frames. That the ignition did not seem to occur on projectile or sabot impact is surprising and may reflect the fact little material was ejected into the interstices on projectile impact as this jetting in other experiments has been followed by intense burning in the interstices. There was little material recovered after this test, as might be expected from frames 7 and 8.

JA2m appears to be more sensitive to projectile impact than its solid counterpart and the differences in velocity of impact causing ignition, though not great are significant. Ignition would not have been expected in JA2 at 520 m s^{-1} and the threshold for ignition in JA2m may indeed be somewhat lower, perhaps around 500 m s^{-1}.

XM43 Gun propellant
On steel projectile impact of a single grain, no ignitions were observed at up to 550 m s^{-1} even after a test resulting in an oblique impact. There was considerable jetting on impact but no evidence of burning of this ejected material or any reaction associated with the subsequent sabot impact. The propellant grain was retrieved unburnt but shattered.

The faster nylon projectile impact of a single grain at up to 705 m s^{-1} produced no ignitions at an interframe time of 2 μs and the grain could be seen to shatter under impact.

Figure 3.11 shows steel projectile (p) impact of a close-packed array at 540 m s^{-1}; impact occurred in frame 1. 5 μs later in frame 2, the interstices between the grains can be seen to be closing up, though there is little reaction associated with this closure. Material can be observed jetting (j) backwards. In frame 3, sabot (s) impact induces reaction and in frame 4 it appears to be linked to the grain boundaries and positions of the original interstices. The reaction can be seen to be fading by frame 5. Figure 3.12 shows steel projectile (p) impact of a columned array at 550 m s^{-1}; impact occurred in frame 1. There is no reaction associated with projectile or sabot (s) impacts, though material can be seen to have been injected into the interstices between the grains in frame 4. The interframe time was 5 μs. All of the material was recovered unburned though fragmented after this test.

Fig. 3.13 shows steel projectile impact of another columned array at 520 m s^{-1}, with impact of the projectile having already occurred by frame 1. The interframe time was 2 μs. Both frames 1 and 2 show "feathering" (f) around the circumference of the initial impact grain (g) and jetting (j) of material into the top interstice. Ignition associated with this interstice can be seen in frames 4 and 5 though whether it is due to sabot shock promoted. The other interstices on closing can also be seen to sustain reaction. Some of the material was recovered.

Although these two results conflict, other tests around the 520-550 m s^{-1} impact velocity suggest that ignition does not usually occur at 520 m s^{-1} and that this was an unusual result. As more material than would be expected after an ignition was recovered, it suggests that propagation of reaction was not as extensive as for the 550 m s^{-1} impact.

XM43m multi-cored Gun propellant
Single grain impacts with steel or nylon projectiles were not performed because of the size of these propellant grains.
This propellant was tested in array form and steel projectile impact of a close packed array at 530 m s^{-1} resulted in bulk ignition of the material beginning with ejected material burning in the interstices as seen before. Ignition sites were also associated with the holes in the propellant.
Figure 3.14 shows steel projectile (p) impact of a columned array at 530 m s^{-1}. The interframe time is 2 µs and impact has already occurred by frame 1. Frame 2 is interesting as it shows luminescence from a hole (h) in a grain (g2) that has not been physically impacted by either the projectile or an adjacent grain. This suggests that the material that has been jetted from the initial impact grain (g1) into the interstices has impacted that grain (g2) and caused adiabatic heating of the gas in the hole causing it to luminesce. Material can be seen ejecting from the far propellant grains (g2 & g3) in frame 3 and if there had been a further layer, this material jetting could have caused a similar reaction in another grain. When the sabot (s) impacts in frame 4, the burning in the interstices is already significant, so the initial reaction was in this case completely due to the projectile. In later frames, the jetted material, in later frames spreads to the other interstices and burning is clearly evident.

3.4 Discussion

JA2 versus JA2m
JA2 is more insensitive to simulated bullet attack than its multi-cored composition JA2m in both single grain and array impacts. JA2 exhibits plastic deformation on impact, swelling to fill the available space without igniting through frictional heating on grain boundary contact. Both materials are sensitive to following sabot impact which re-shocks the material after it has first been distrubed by projectile impact, and JA2 is sensitive after pointed-ended projectile impact which is perhaps surprising as the front-end geometry of that type of projectile produces much less damage in the material in terms of viscous heating and shear than a comparable flat-ended one. JA2m, on impact, does not appear to plastically deform to the same extent as JA2 but the grains appear to fracture through lines of weakness which occur between the holes. The holes themselves are susceptible to shock induced collapse causing adiabatic compression of the gas in the holes leading to points of ignition.
Where light output can be seen in the interstices of the propellant grains, it is likely that this is due to material having been spalled off the grains during impact and ejected into interstices which have been heated by shock compression. As the spalled material has a large surface area to volume ratio with respect to the propellant grain, it is far more likely to ignite and evidence for this can be observed in many of the pictures. Indeed, asymmetric impacts which cause parts of grains to be sheared off and jetted into these interstices have caused ignition at lower

14

velocities than would have been expected for squarer impacts. For JA2m with its array of holes, a similar spalling process could happen (on a much smaller scale) in the holes themselves causing ignition.

XM43 versus XM43m

Not perhaps surprisingly considering the results for JA2/JA2m, XM43m was found to be more sensitive to simulated bullet attack than XM43. For single grain impacts, XM43 shattered but did not ignite. For the array experiments, much jetting or spalling of material into the interstices can be seen for both these materials with following ignition. Again, the multi-cored composition was more sensitive due to its holes for the reasons discussed earlier.

3.5 Conclusions

Single grain impacts at the velocities tested in these experiments do not give an insight into the behaviour of a typical multi-grained, propellant charge. The results of these single grain impacts suggest that the two materials are insensitive to projectile impact at these velocities when this is clearly not the case if the materials are tested in arrays.

Geometric arrangement of the propellant has an effect on its subsequent sensitivity to simulated bullet attack. It is possible that close-packed arrays are less sensitive than columned arrays as material that gets spalled off into the interstices can spread further in the larger interstitial distance of a columned array and impact other grain(s). This type of spall impact, where a physically unimpacted grain is ignited by spall from an impacted grain has been observed photographically. Burning of this spalled material will also occur because of its very large surface area to volume ratio and because the gas in the interstices have been heated by shock compression. In a close-packed array, the interstitial distances are smaller by comparison and it is suggested that although material can be spalled into these spaces, ignition is probably due mainly to the spalled material being heated and burning on contact with the heated gas in the interstices rather than also by spall impact onto another grain.

XM43 fractures in a brittle manner under impact whereas JA2 can deform plastically. XM43 shows a greater tendency to spall and this could be associated with its lower tensile strength. XM43 does however require higher velocities to cause ignition in array geometries than JA2 though the difference in velocities required between the two materials is not great. Both materials are susceptible to further shock compression if they have already been damaged though JA2 appears to be more sensitive to this and the subsequent ignitions are more violent.

As has been shown, angled impacts can cause more severe effects with array geometries than squarer ones. The grain experiences greater shear over a smaller area on impact and material is jetted outwards into the interstices where it burns in the heated gas spaces. There will always be jetting above a certain, critical contact angle.

Multi-cored propellants are more susceptible to simulated bullet attack than their solid equivalents. They are also more susceptible to shock compression without immediate penetration. The sites of ignition are the holes but in addition, the inclusion of an array of holes appears to "build-in" regions of weakness between these holes which have been shown to fail shortly after impact. It would be

interesting to determine the optimum size of hole that would allow an increased burning rate but not be (so) suceptible to shock compression.

Appendix (iii) summarises research into simulated fragment attack of cased munitions and discusses the effect of the casing and the casing material on the ignition mechanisms of several different explosive compositions.

4. DROP-WEIGHT IMPACT STUDIES ON PROPELLANTS

High-speed photographic sequences of the rapid deformation (strain rates *ca.* 2×10^3 s^{-1}) of discs cut from grains of XM43, JA2, F300/75 and LM1900 were obtained using the drop-weight apparatus shown schematically in figure 4.1. The drop hammer has a mass of 5.5kg and falls from a height of 1.3m. This apparatus was originally developed by Blackwood & Bowden (1952) and has more recently been extensively employed by Heavens, Field, Swallowe and others in the study of the sensitivity to impact of a wide range of energetic materials (see the references by Heavens & Field (1974), Swallowe & Field (1981), Field, Swallowe & Heavens (1982), Krishna Mohan & Field (1984), Krishna Mohan *et al.* (1984), Field *et al.* (1985, 1992), & Walley *et al.* (1992)). The field of view in all the sequences presented is 20mm in diameter.

Figure 4.2 shows the rapid deformation at room temperature of a solid disc of XM43. Although the periphery of the disc becomes ragged, no deflagration was observed. In previous (and published) work we have shown that enclosing air spaces within propellant samples sensitized them (Walley *et al.* (1992)). One way of enclosing an air space is to punch a hole in the disc. Thus figure 4.3 shows the rapid deformation of an annulus of XM43 at room temperature. Again deflagration was not observed. Another way of enclosing an airspace is to make arrays of discs. Figure 4.4 shows the rapid deformation at room temperature of a triangular array of small discs punched out from the larger discs of XM43. Again no deflagration was obtained. Three other drops on samples of XM43 were performed in this apparatus without using high-speed photography: two were on solid discs and one was on a fragment semicircular in shape. Neither of the two whole discs deflagrated but the semicircular fragment did deflagrate. So another high-speed photographic sequence was taken of the rapid deformation of a similar fragment (figure 4.5). But no deflagration was observed. To summarise, seven drops were performed on XM43 at room temperature and deflagration was observed only once.

Figure 4.6 is a high-speed photographic sequence of the rapid deformation at room temperature of a solid disc of JA2. Deflagration can be seen starting in the frame labelled 350µs as a small dark spot. This grows rapidly, tearing the disc until finally the gaseous products erupt from the edge of the disc at 399µs. Another crack can be seen growing from 420µs onwards until it too breaks out at 476µs. Further burning from 525µs onwards produced a pronounced 'two-fingered' scar on the surface of the glass anvil. Three other drops were performed on discs of JA2 at room temperature and all produced deflagrations.

Figures 4.7-4.9 present high-speed photographic sequences of the rapid deformation at room temperature of discs cut from grains of F300/75. These grains have a hexagonal array of burning holes which on past experience were expected to sensitize the propellant in this impact configuration. Two of the three sequences show strong deflagrations but it is not clear that the deflagrations started from the site of any of the collapsed holes (see the frames where overwriting produced double exposure of the initial and final states). One of the three (figure 4.9) did not

16

produce a deflagration. Three more drops were performed without high-speed photography. In all three cases, one or other of the glass anvils smashed part way through the deformation. No deflagrations were obtained in these extra three drops and it is possible that this was due to release of pressure before ignition caused by the breaking of the anvils.

Figure 4.10 is a high-speed photographic sequence of the rapid deformation at room temperature of a disc of LM1900. Again this has a hexagonal array of burning holes. These can be seen to close up during deformation appearing as dark spots (instead of light ones) in the frame labelled 525μs. Deflagration can be seen to have started in this frame just below one of the burning holes. By 560μs the burning hole it was close to has opened up and another burning site has started close to one of the other holes. At 630μs the central burning hole has started to open up and at 700μs a fourth hole starts. All four burning sites continue to deflagrate throughout the deformation. It should be noted that unfortunately the bottom eight frames were mounted wrongly: they are rotated by 90° counterclockwise with respect to the upper eight frames.

Another way of sensitising propellant compositions whose binder undergoes a glass transition is to cool them below their glass transition temperature (Walley *et al.* (1992)). JA2 and XM43 were tested in this apparatus at liquid nitrogen temperatures. Figure 4.11 is the sequence obtained for JA2. The deflagration was stronger than any of the ones obtained at room temperature. Unfortunately the camera triggered late so the initial fragmentation of the disc was not captured. The strong light emission of the deflagrating powder can clearly be seen. An attempt was made to obtain a similar sequence for XM43 but this was unsuccessful. The XM43 did not, however, deflagrate at this low temperature (one drop).

TABLE 4.1

Statistics on propellant discs at room temperature

Composition	Number of drops	Number of deflagrations
XM43	7	1
JA2	4	4
F300/75	6	2
LM1900	1	1

REFERENCES

Blackwood J.D. & Bowden F.P. (1952) "The initiation, burning and thermal decomposition of gunpowder" *Proc. Roy, Soc. Lond.* A 213 285

Boyle V., Frey B. and Blake O. (1989) "Combined pressure shear ignition of explosives", Ninth Symposium (International) on Detonation, Portland, Oregon, pp. 3-17.

Burch, J.M. and Forno, C. (1982) "High resolution moiré photography",*Opt. Engng* 21 602-614

Field J.E., Bourne N.K., Palmer S.J.P., Walley S.M., (1992) "Hot-spot ignition mechanisms for explosives and propellants", *Phil. Trans. R. Soc. Lond.* A339 269-283

Field J.E., Palmer S.J.P., Pope P.H., Sundarajan R. & and Swallowe G.M. (1985) "Mechanical properties of PBX's and their behaviour during drop-weight impact" in *Proc. 8th Int. Symp. on Detonation*, Albuquerque, U.S.A.

Field J.E., Swallowe G.M. & Heavens S.N. (1982) "Ignition mechanisms of explosives during mechanical deformation" *Proc. Roy. Soc. Lond.* A **382** 231

Fong C.W. (1985) "Crack initiation in perforated propellants under high strain rate impact conditions", *Propellants, Explosives, Pyrotechnics* **10** 91-96

Goldrein H.T., Huntley J.M., Palmer S.J.P., Whitworth M. B. and Field J.E. (1993) "Optical techniques for strength studies of polymer bonded explosives" , Tenth Symposium (International) on Detonation, Boston, Massachusetts.

Heavens S.N. & Field J.E. (1974) "The ignition of a thin layer of explosive by impact" *Proc. Roy. Soc. Lond.* A **338** 77

Ho S.Y. and Fong C.W. (1989) "Relationship between impact ignition sensitivity and kinetics of the thermal decomposition of solid propellants", *Combustion and Flame* **75** 139-151.

Huntley J.M. (1989) "Noise Immune phase unwrapping algorithm", *Appl. Opt.*, **28** 3268-3270

Krishna Mohan V. & Field J.E. (1984) "Impact initiation of hexanitrostilbene" *Combustion and Flame* **56** 269

Krishna Mohan V, Field J.E. & Swallowe G.M. (1984) "Effects of physical inhomogeneities on the impact sensitivity of solid explosives: A high-speed photographic study" *Combustion Sci. and Tech.* **44** 269

Parks V.J. (1982) "Strain measurement using grids" *Opt. Engng*, **21** 633-639

Swallowe G.M. & Field J.E.(1982) "The ignition of a thin layer of explosive by impact: The effect of polymer particles" *Proc. Roy. Soc. Lond.* A **379** 389

Walley S.M., Field J.E., Palmer S.J.P., (1992) "Impact sensitivity of propellants", *Proc. R. Soc. Lond.* A **438** 571-583
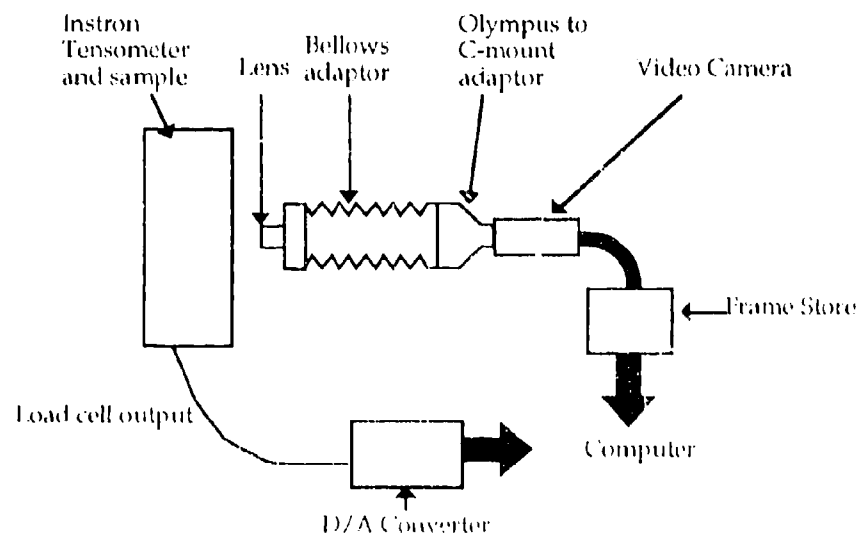
Figure 2.1. Set-up for image processing studies.
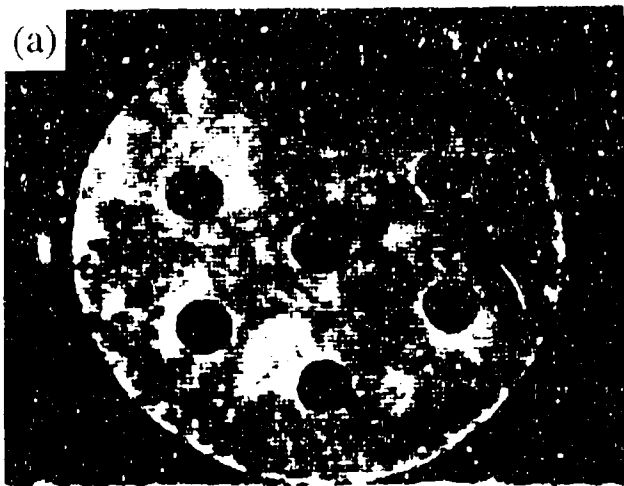
*Figure 2.2. Computer generated images of sample #4, loaded in configuration I.
Loads (a) 0.8 kg, (b) 75.35 kg, (c) 91.1 kg, (d) 102.0 kg, (e) 111.4 kg, (f) 102.25 kg*
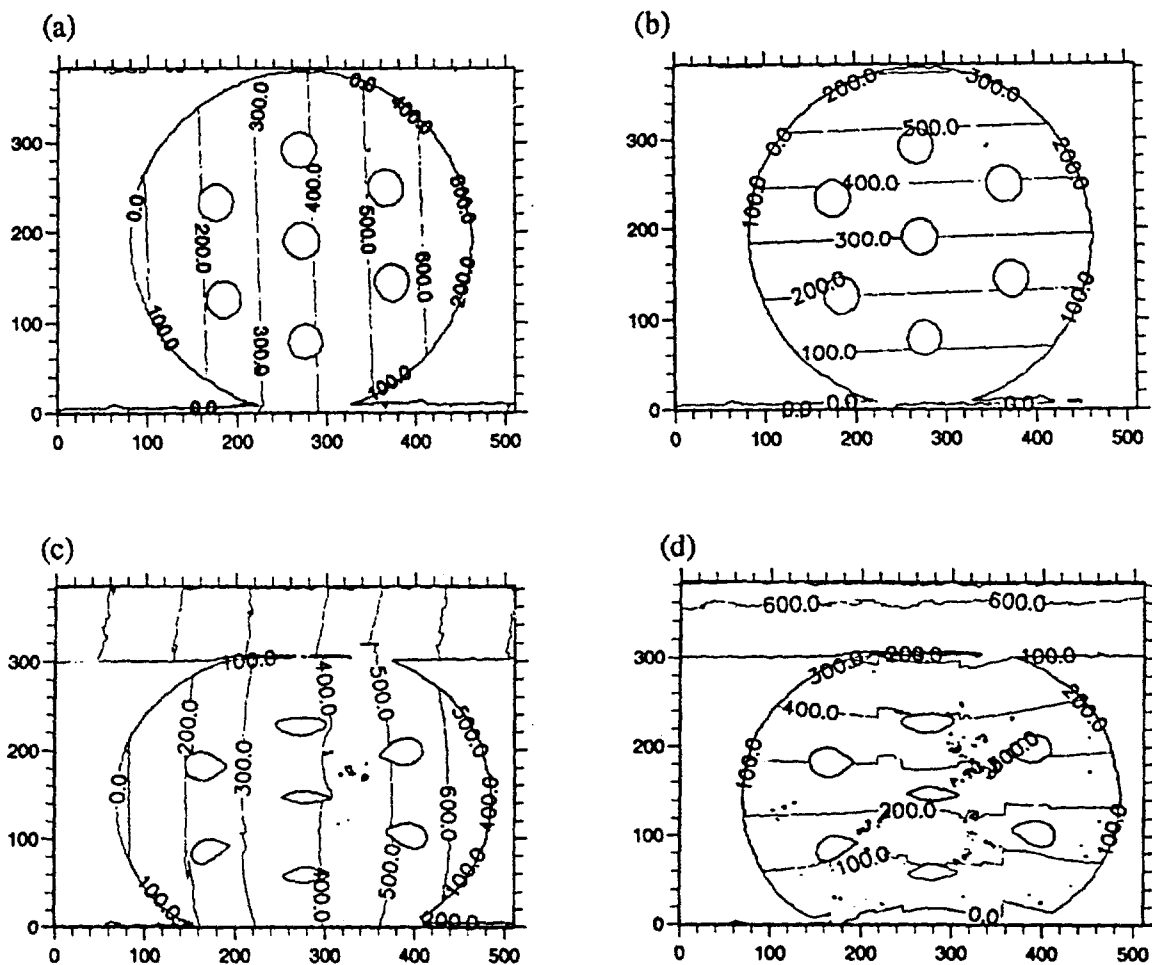
Figure 2.3. Contour maps of unwrapped phase. (a) undeformed sample, x phase,
(b) undeformed sample, y phase, (c) deformed sample, x phase, (b) deformed sample, y phase.
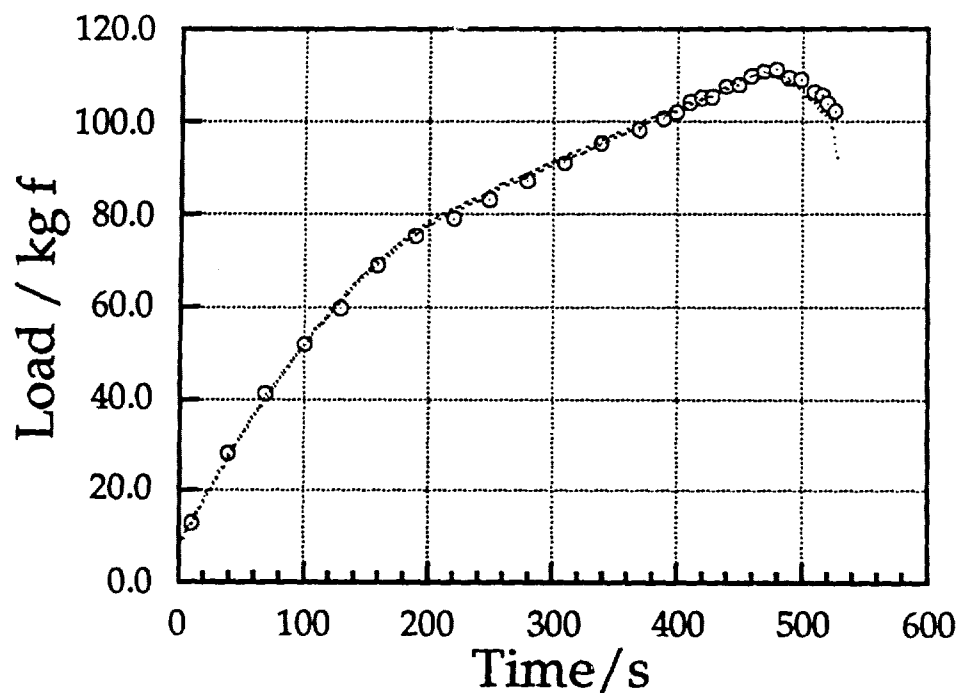
Figure 2.4. Samples #4 and #6, configuration I
Load versus Time
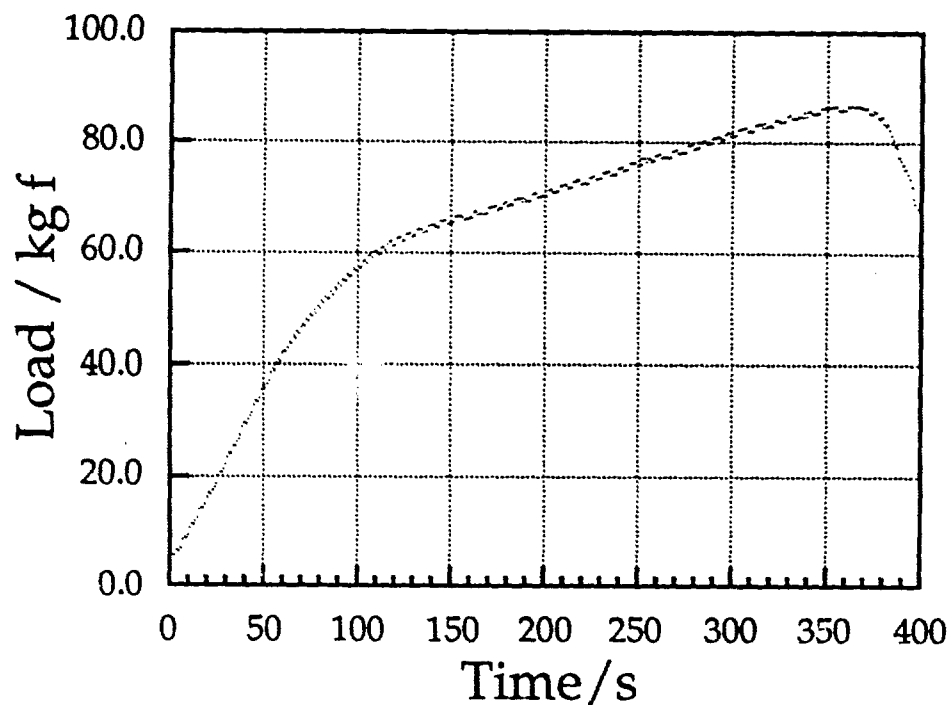
Figure 2.5. Sample #9, configuration II
Load versus Time
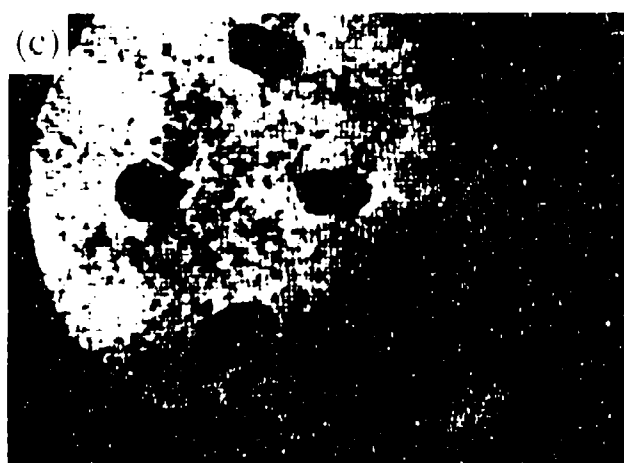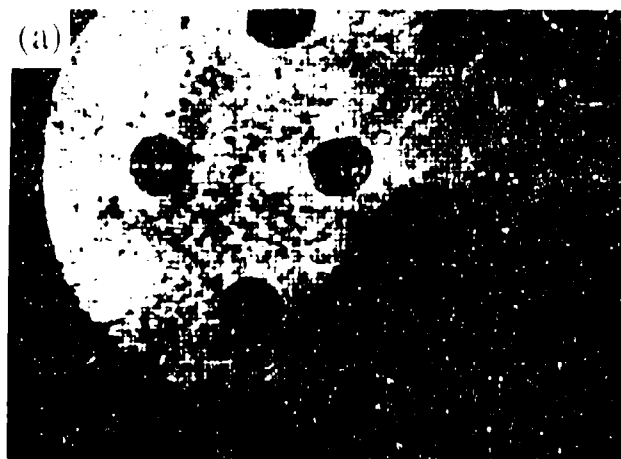
Figure 2.6. Computer generated images of sample #9, loaded in configuration II. Loads (a) 0.0 kg, (b) 55.2 kg, (c) 71.75 kg, (d) 84.5 kg, (e) 85.5 kg, (f) 75.0 kg (during unloading)
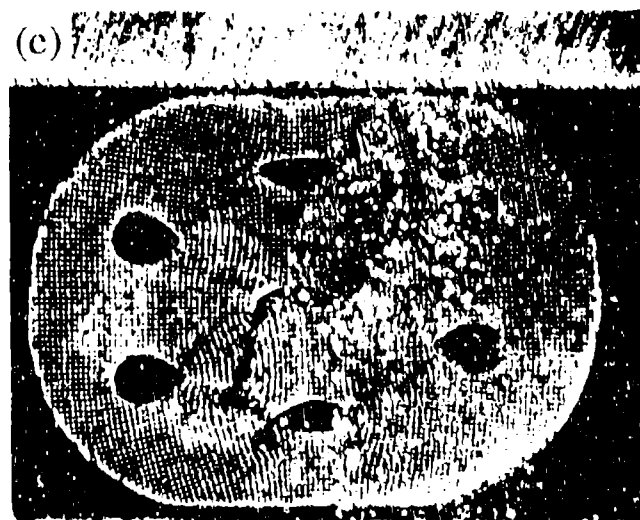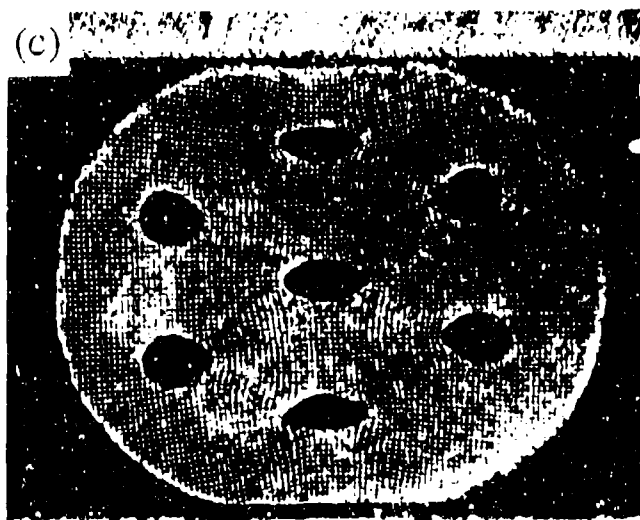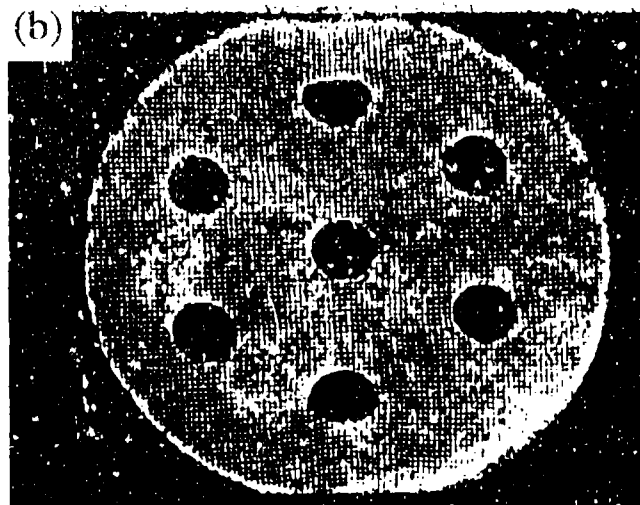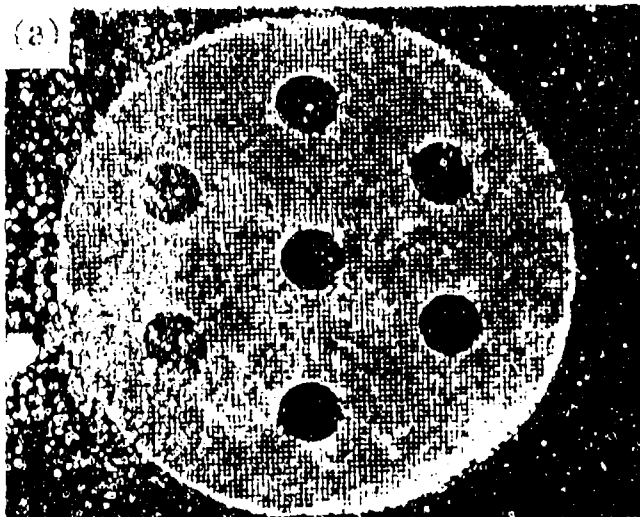
*Figure 2 7 Photographic images of sample #3, loaded in configuration 1.
Loads (a) 0.0 kg, (b) 76 kg, (c) 94 kg, (d) 105 kg, (e) 116 kg, (f) 0 kg (after unloading)*
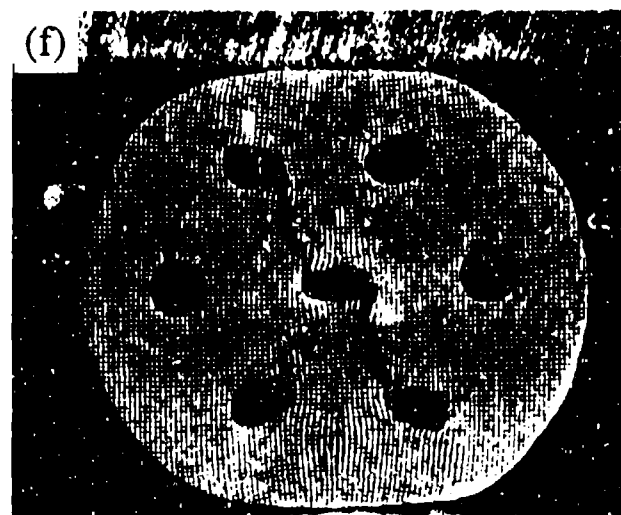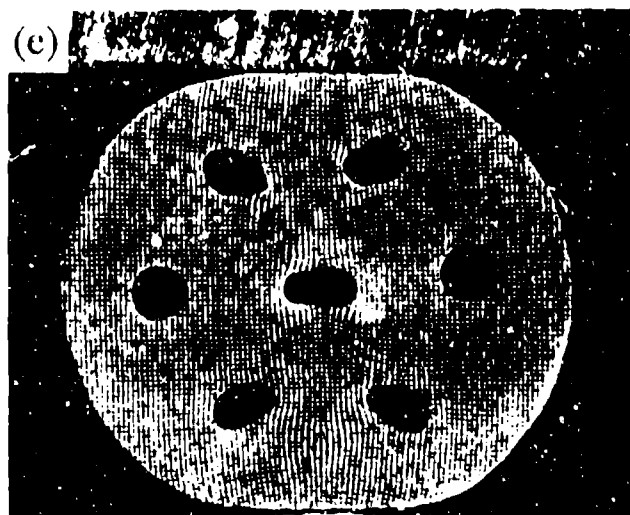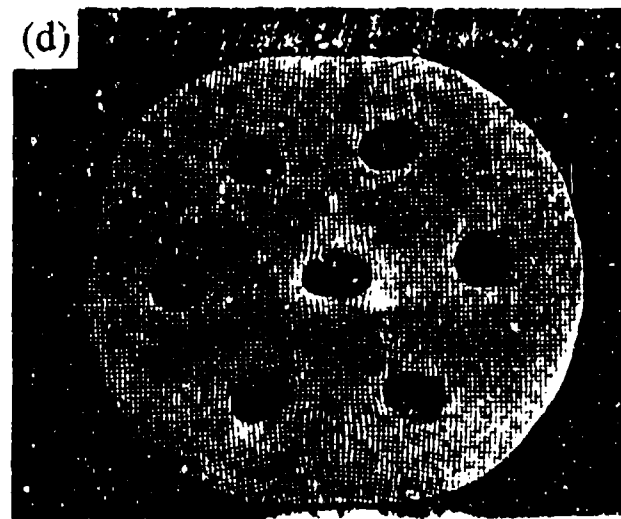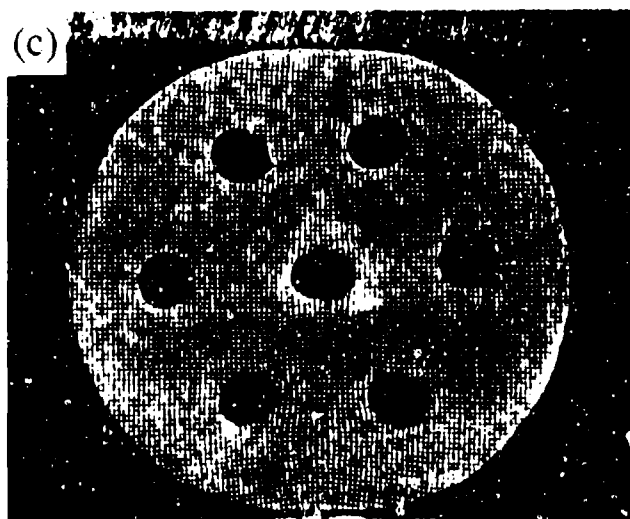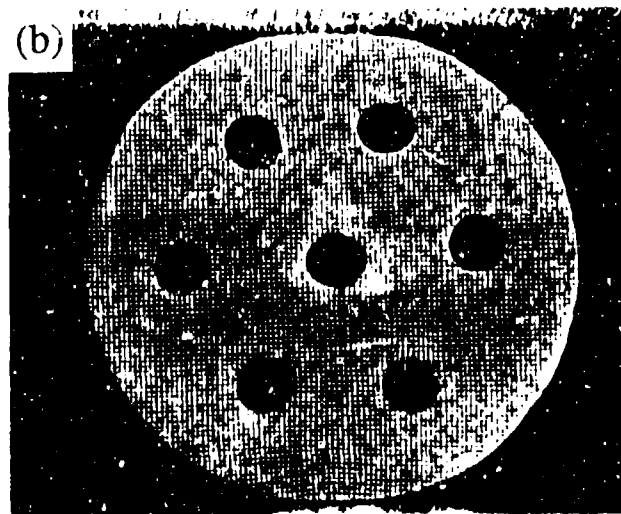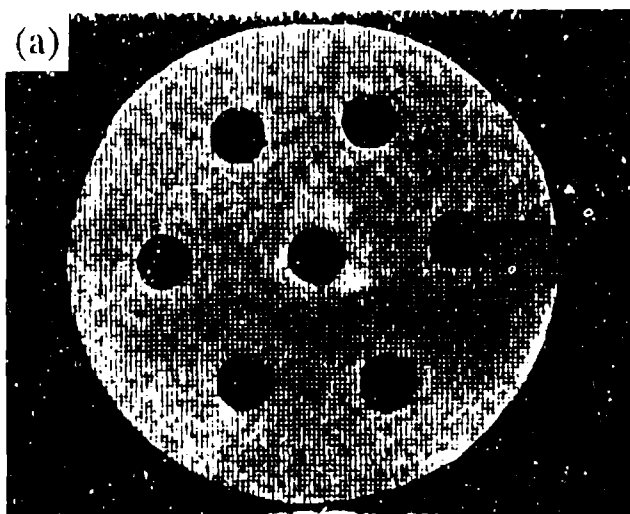
Figure 2.8. Photographic images of sample #2, loaded in configuration II.
Loads (a) 0.0 kg, (b) 60 kg, (c) 72 kg, (d) 80 kg, (e) 86 kg, (f) 0 kg (after unloading)
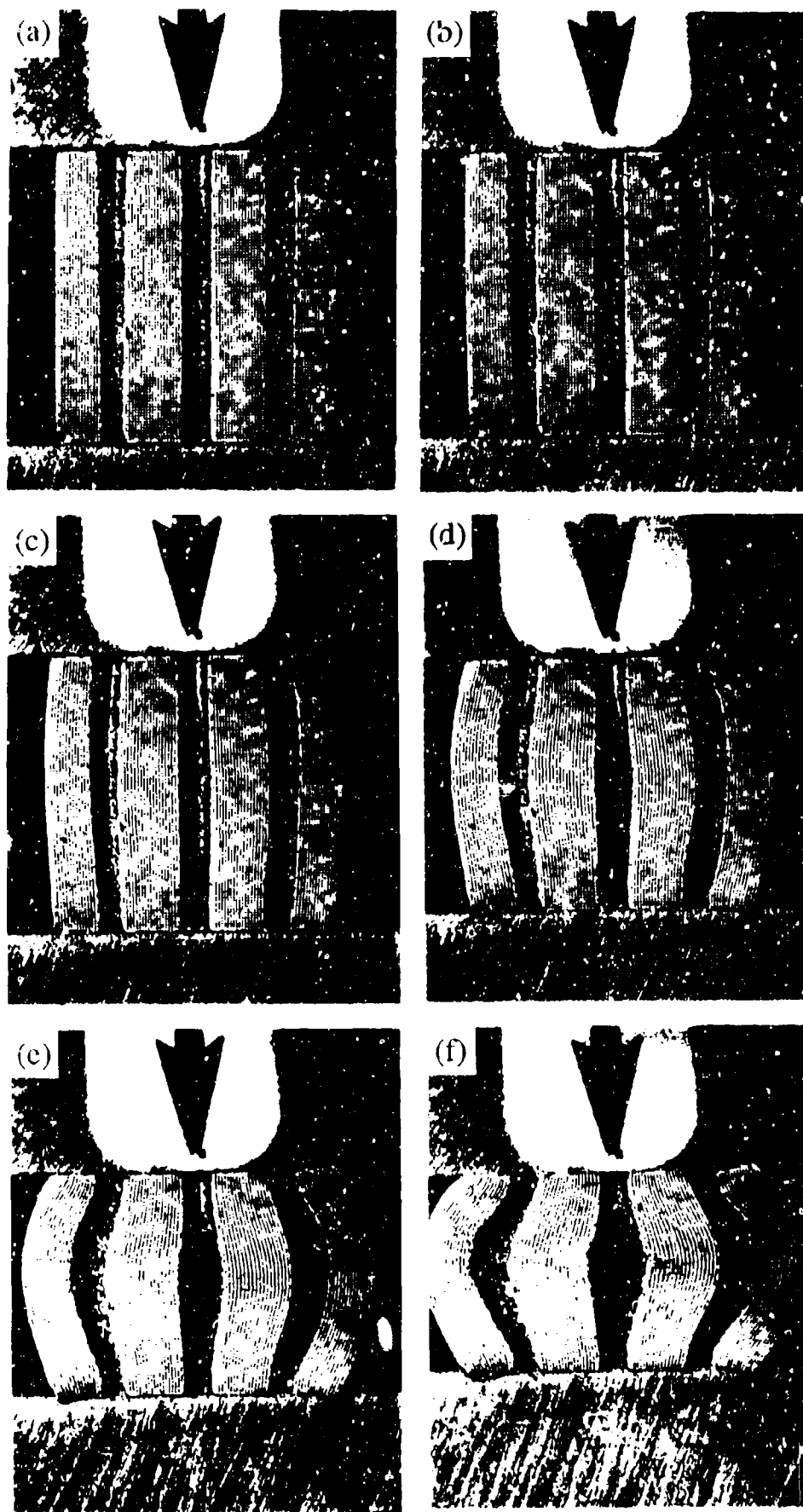
Figure 2.9. Photographic images of sample SP#2, loaded in configuration III. Loads (a) 0.0 kg, (b) 75 kg, (c) 83 kg, (d) 95 kg, (e) 118 kg, (f) 134 kg
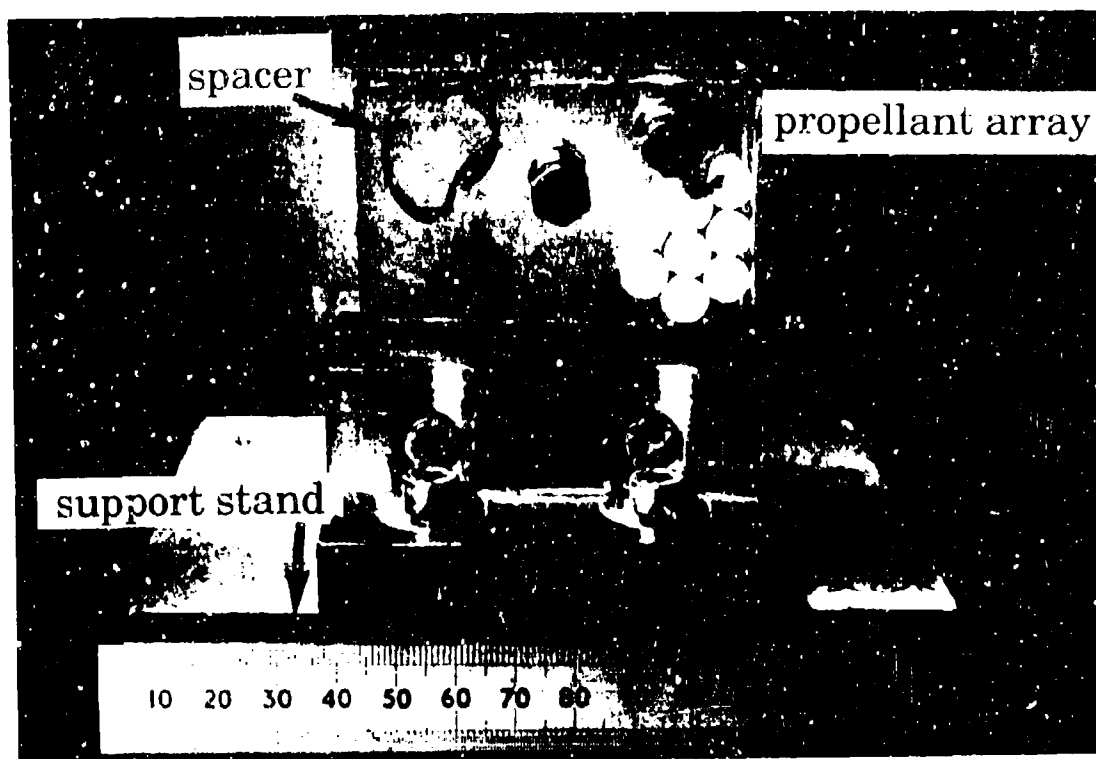
Figure 3.1 Photograph of the target arrangement showing propellant grains confined and in a close-packed array.
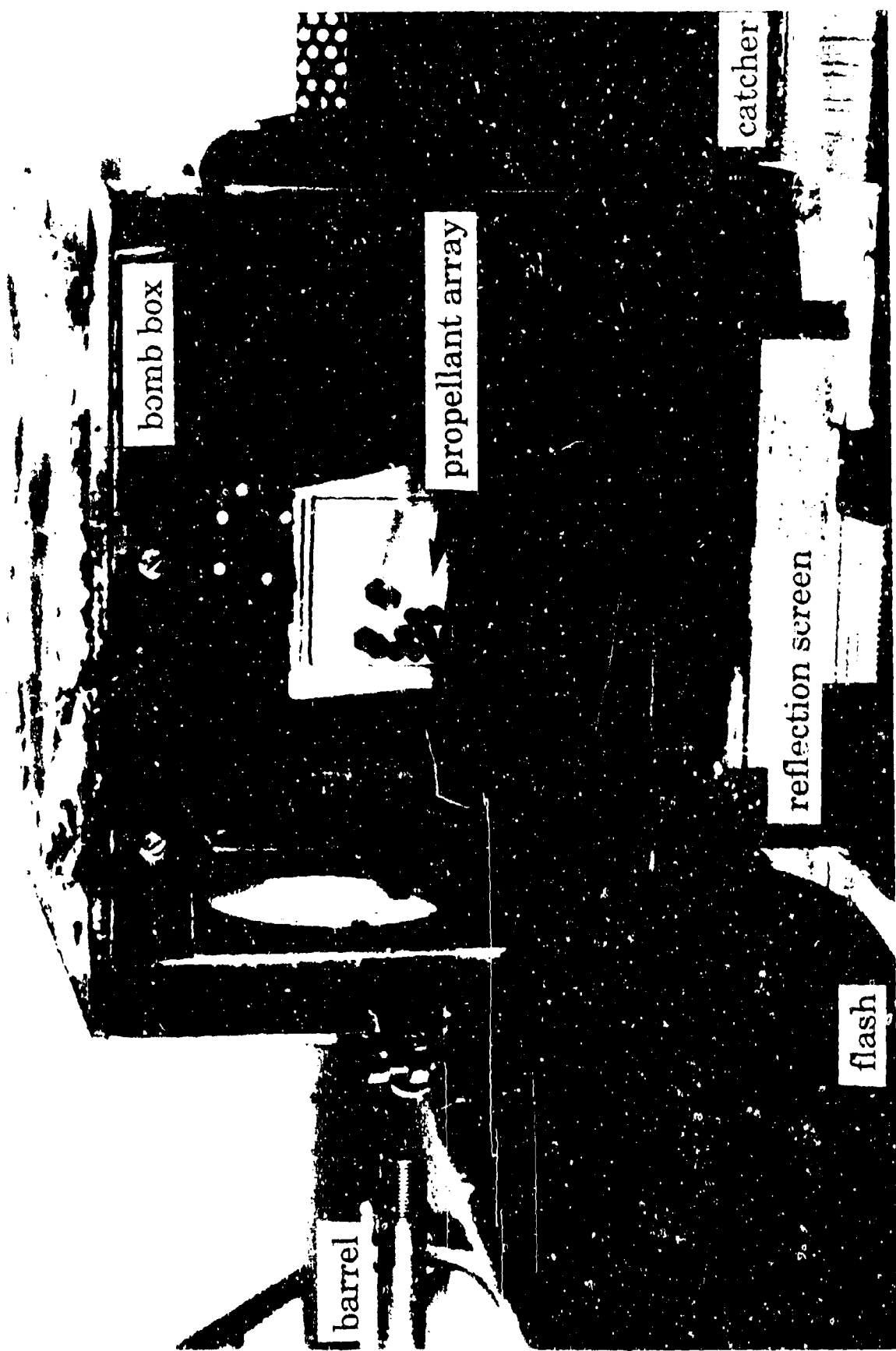
Figure 3.2 Photograph of the target arrangement within the experimental set-up.

JA2 stick

XM43

XM43 single grain

JA2m

XM43m

10 mm
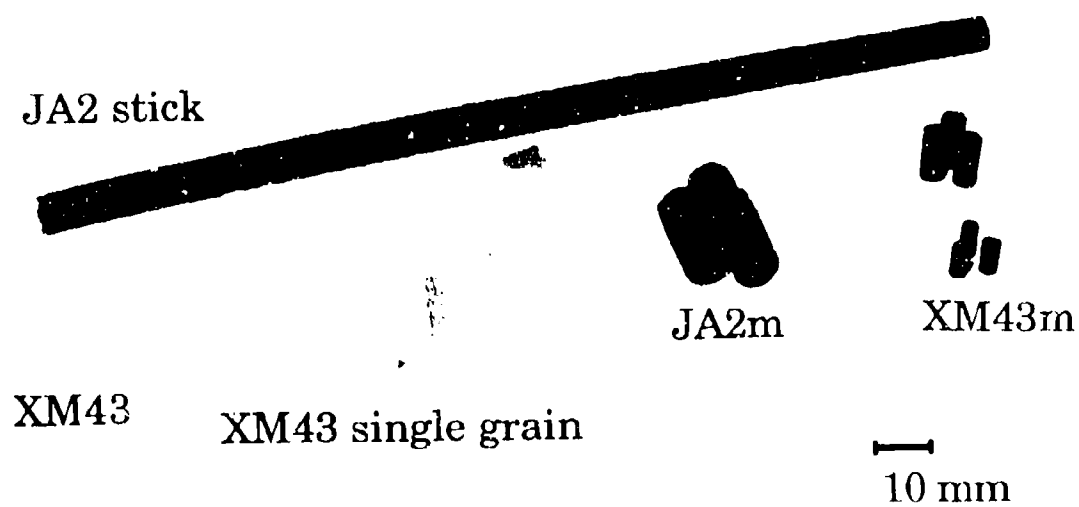
Figure 3.3 Photograph of the types of gun propellant tested for comparison.
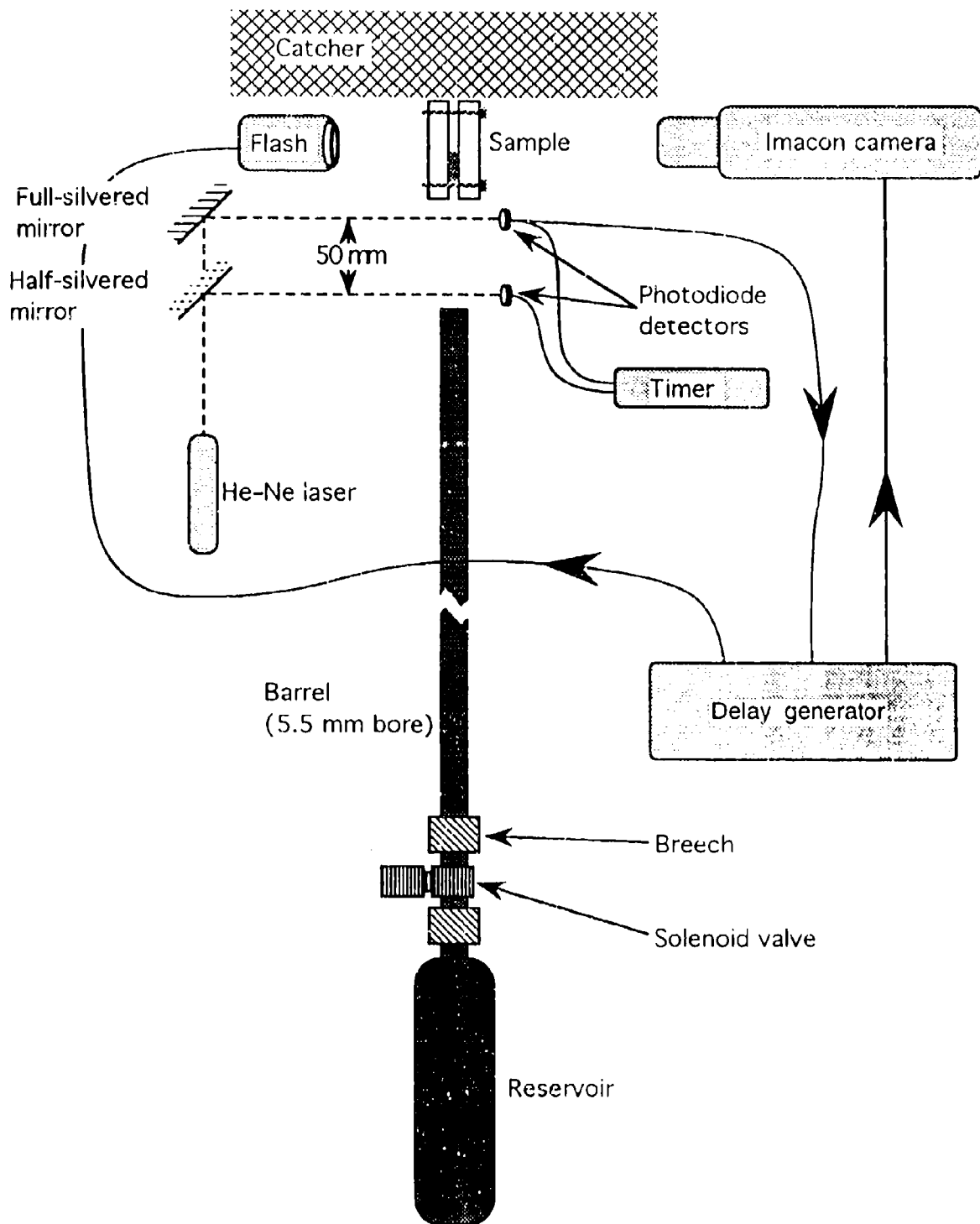
*Figure 3.4. Schematic diagram of experimental arrangement for simulated bullet attack.*

Figure 3.5 High-speed photograph of a steel projectile impacting a close-packed array of JA2 at 575 m s⁻¹. The interframe time was 5 μs.
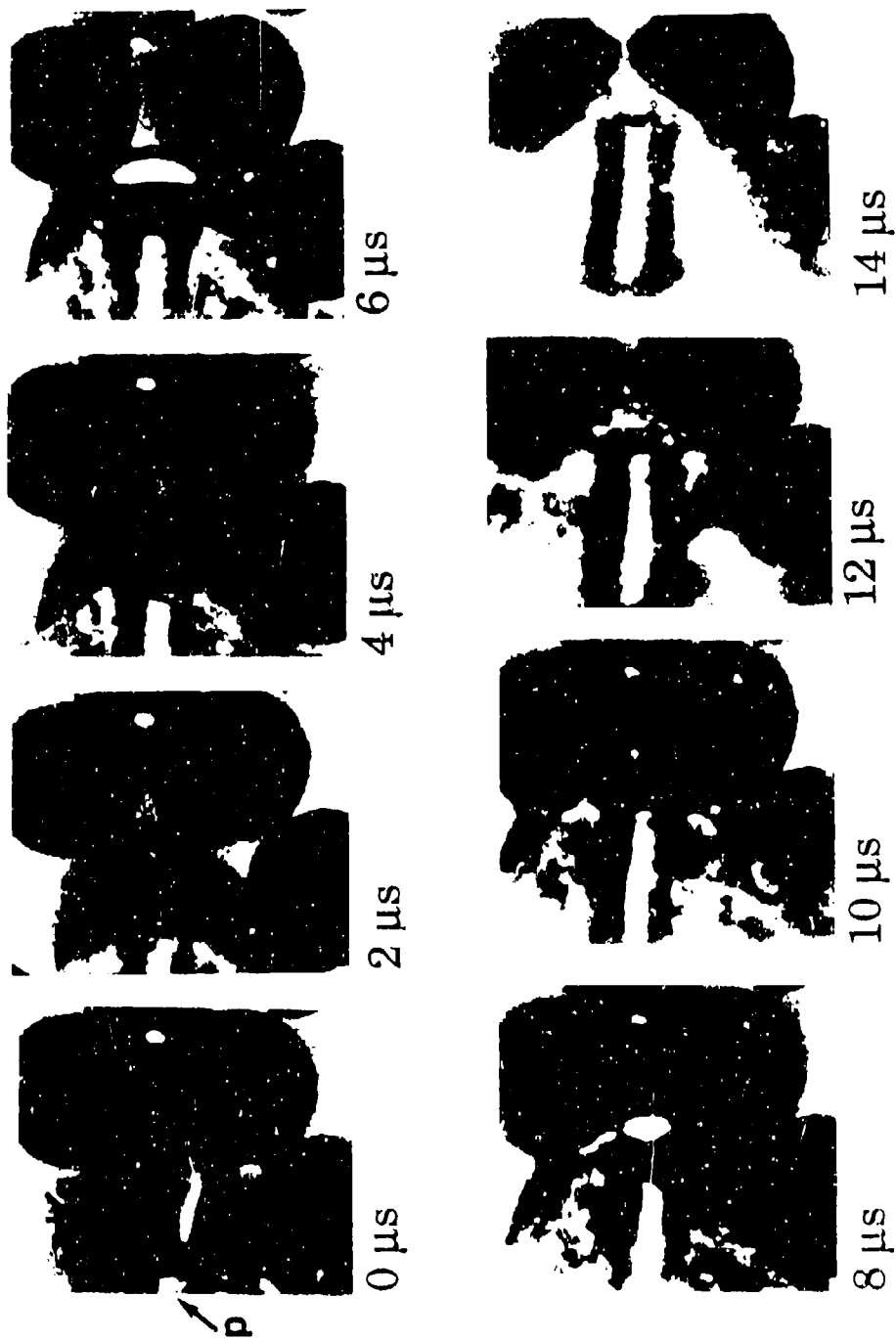
Figure 3.6 High-speed photograph of a steel projectile impacting a close-packed array of JA2 at 540 m s⁻¹. The interframe time was 2 μs.
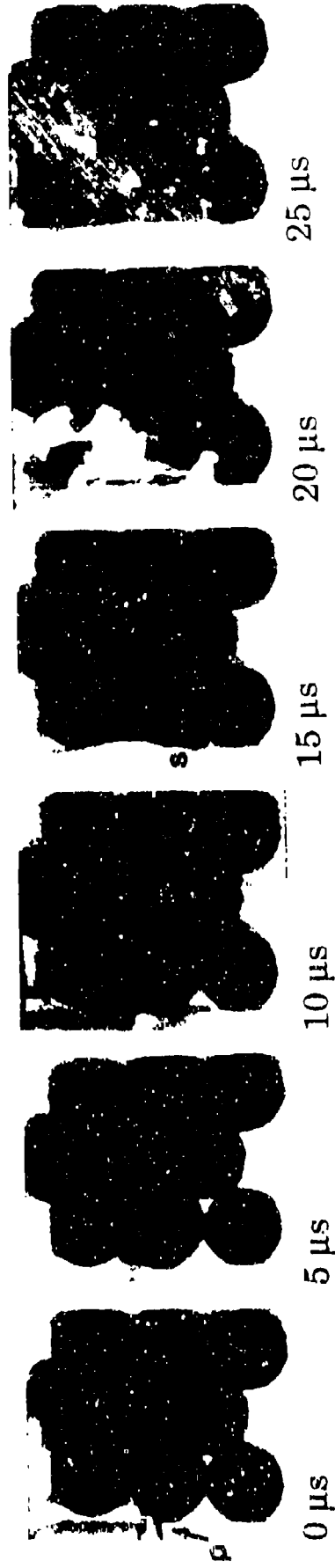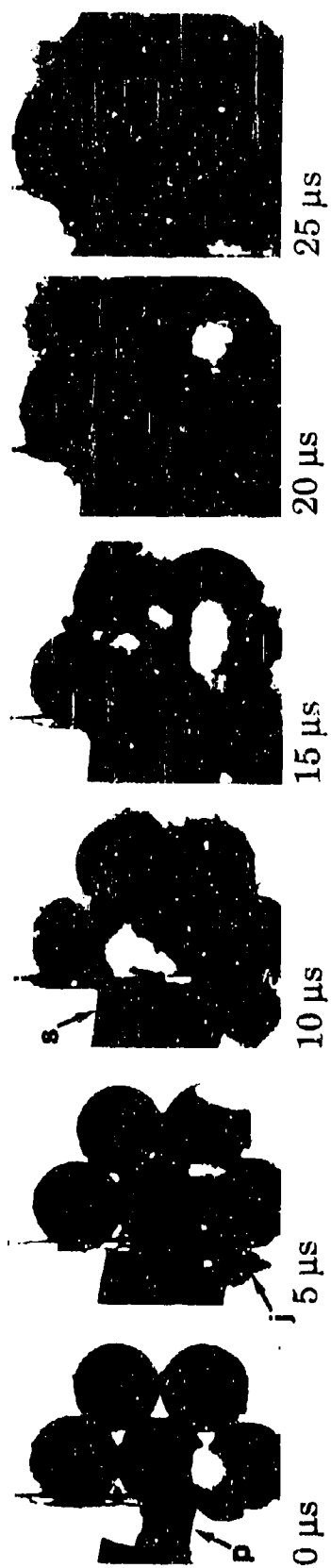
Figure 3.7 High-speed photograph of a pointed-ended steel projectile impacting a close-packed array of JA2 at 550 m s⁻¹. The interframe time was 5 μs.
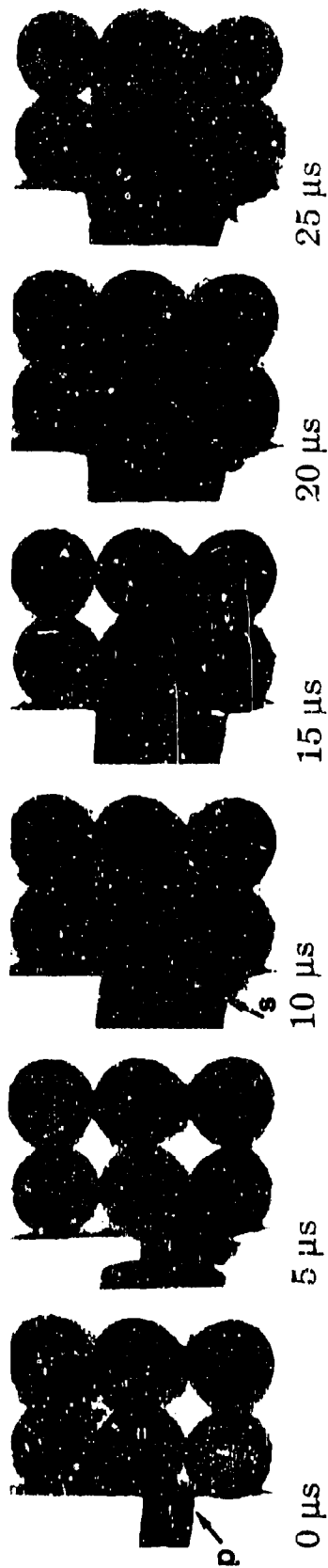
0 μs   5 μs   10 μs   15 μs   20 μs   25 μs
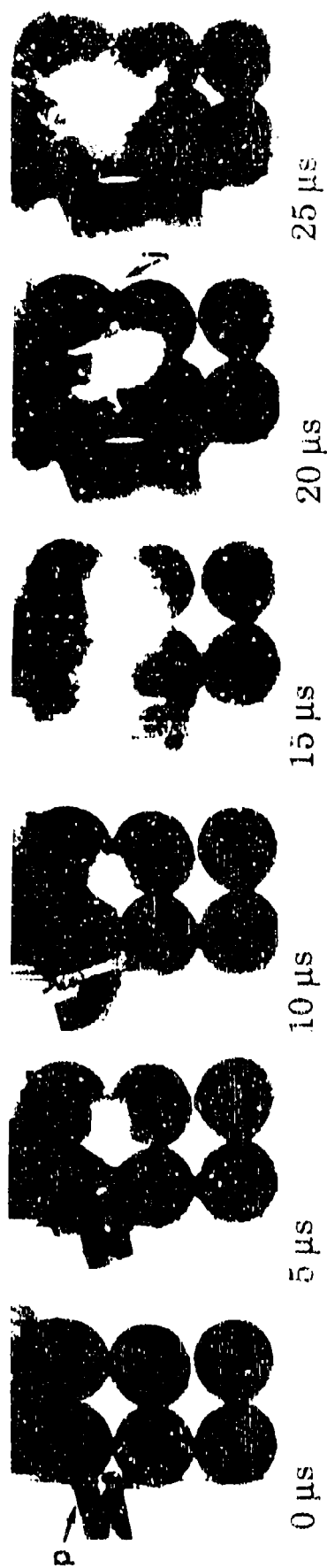
Figure 3.8 High-speed photograph of a steel projectile impacting a columned array of JA2 at 540 m s⁻¹. The interframe time was 5 μs.
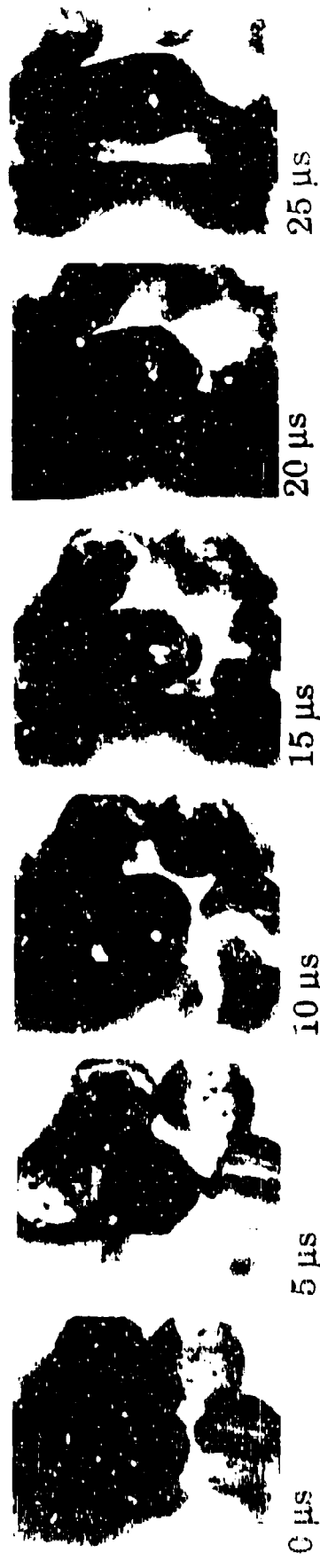
Figure 3.9 High-speed photograph of a steel projectile impacting a close-packed array of JA2m at 520 m s⁻¹. The interframe time was 5 μs.

0 μs 5 μs 10 μs 15 μs 20 μs 25 μs

Figure 3.10 High-speed photograph of a steel projectile impacting a columned array of [A2m at 540 m s⁻¹. The interframe time was 5 µs.

Figure 3.11 High-speed photograph of a steel projectile impacting a close-packed array of XM43 at 540 m s⁻¹. The interframe time was 5 μs.

Figure 3.12 High-speed photograph of a steel projectile impacting a columned array of XM43 at 550 m s⁻¹. The interframe time was 5 μs.
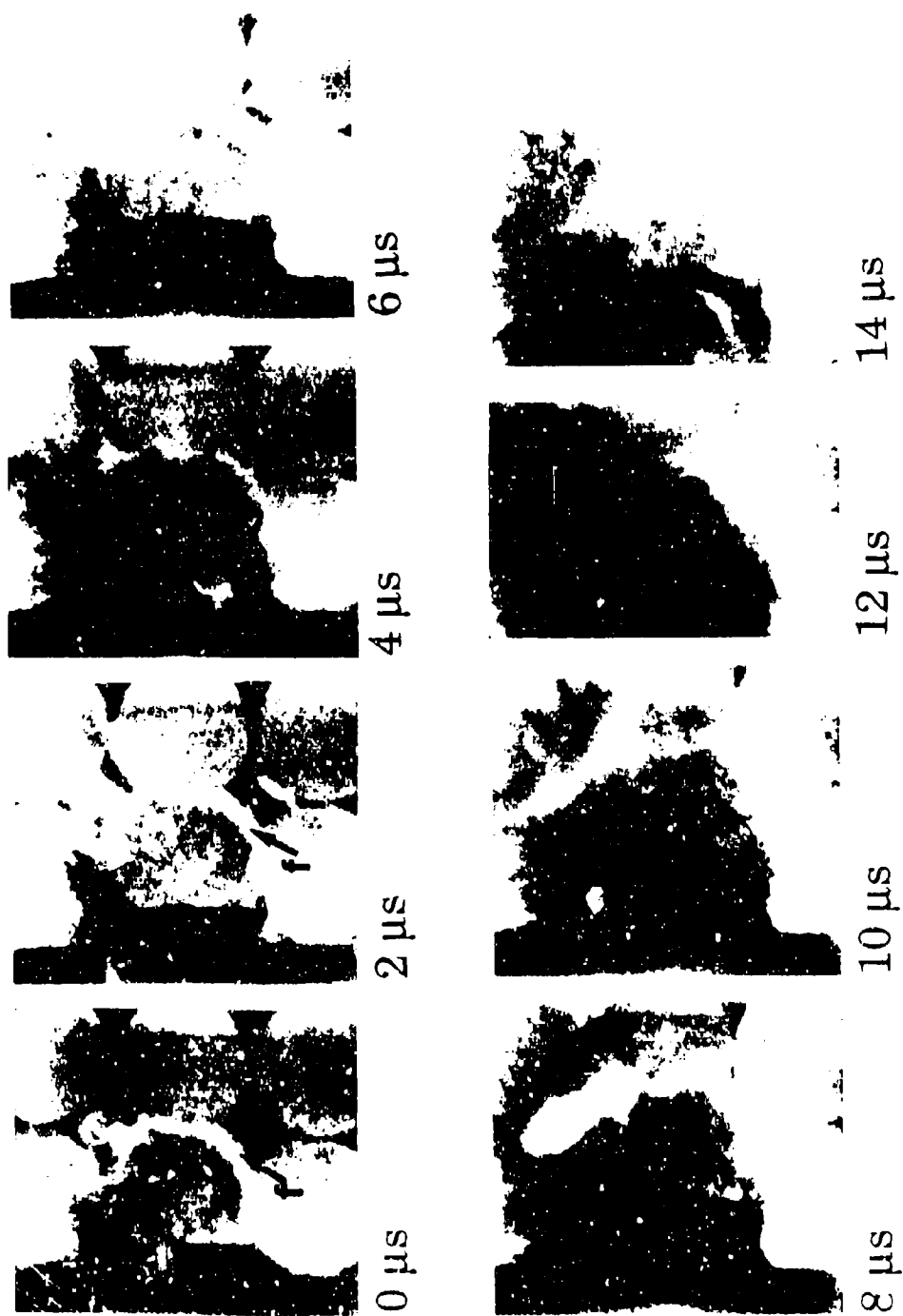
Figure 3.13 High-speed photograph of a steel projectile impacting a columned array of XM43 at 520 m s^{-1}. The interframe time was 2 μs.
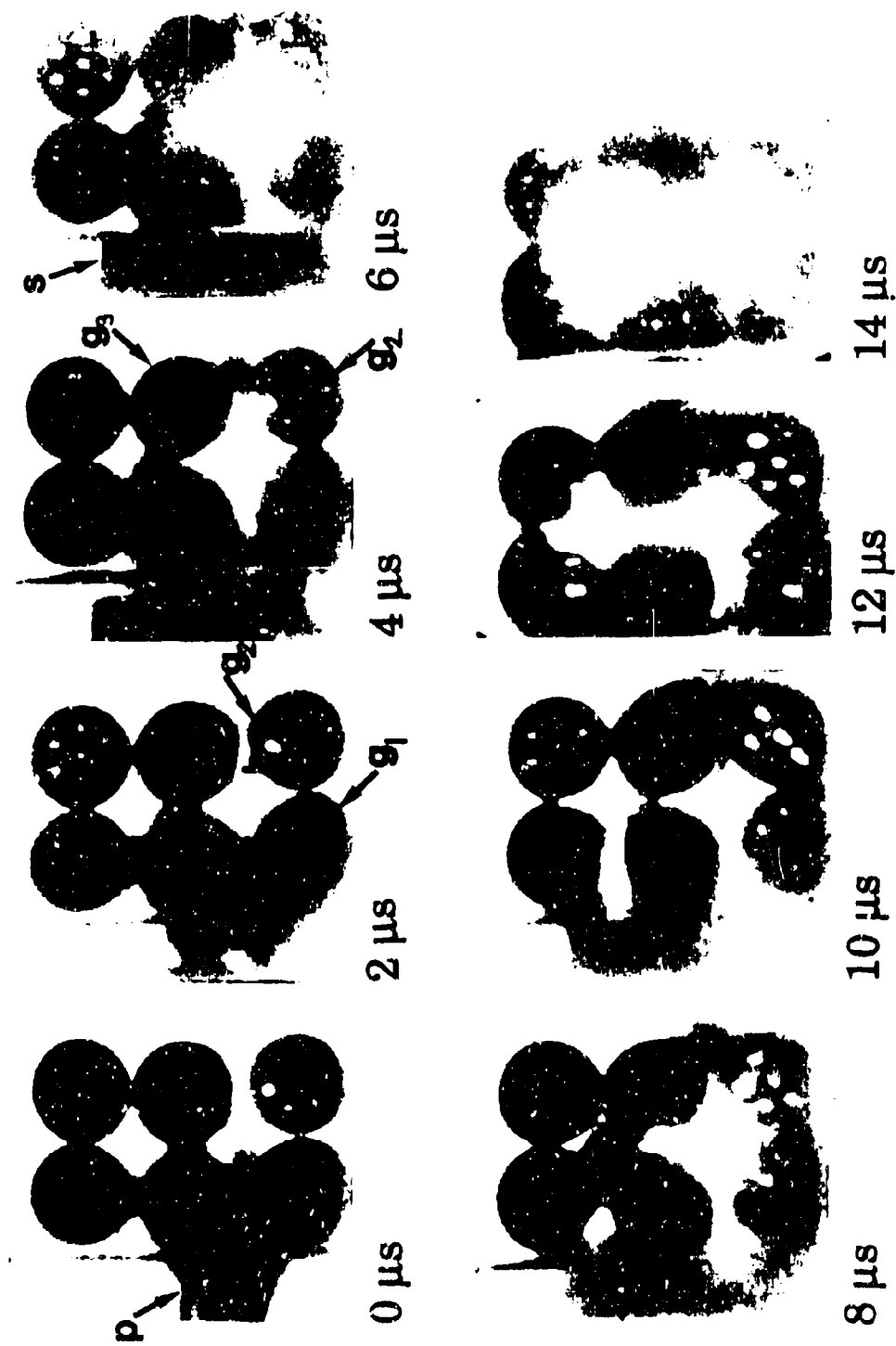
Figure 3.14 High-speed photograph of a steel projectile impacting a columned array of XM43m at 530 m s⁻¹. The interframe time was 2 μs.
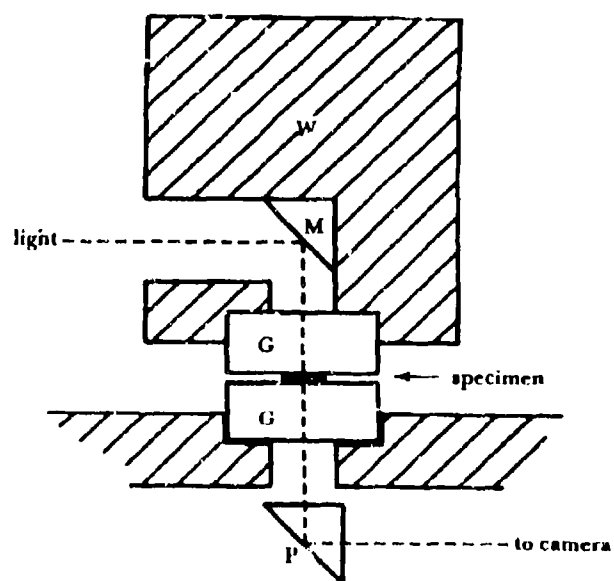
Fig. 4.1 Schematic diagram of the dropweight apparatus modified for high-speed photography. W, weight; M, mirror; G, glass anvils; P, prism.
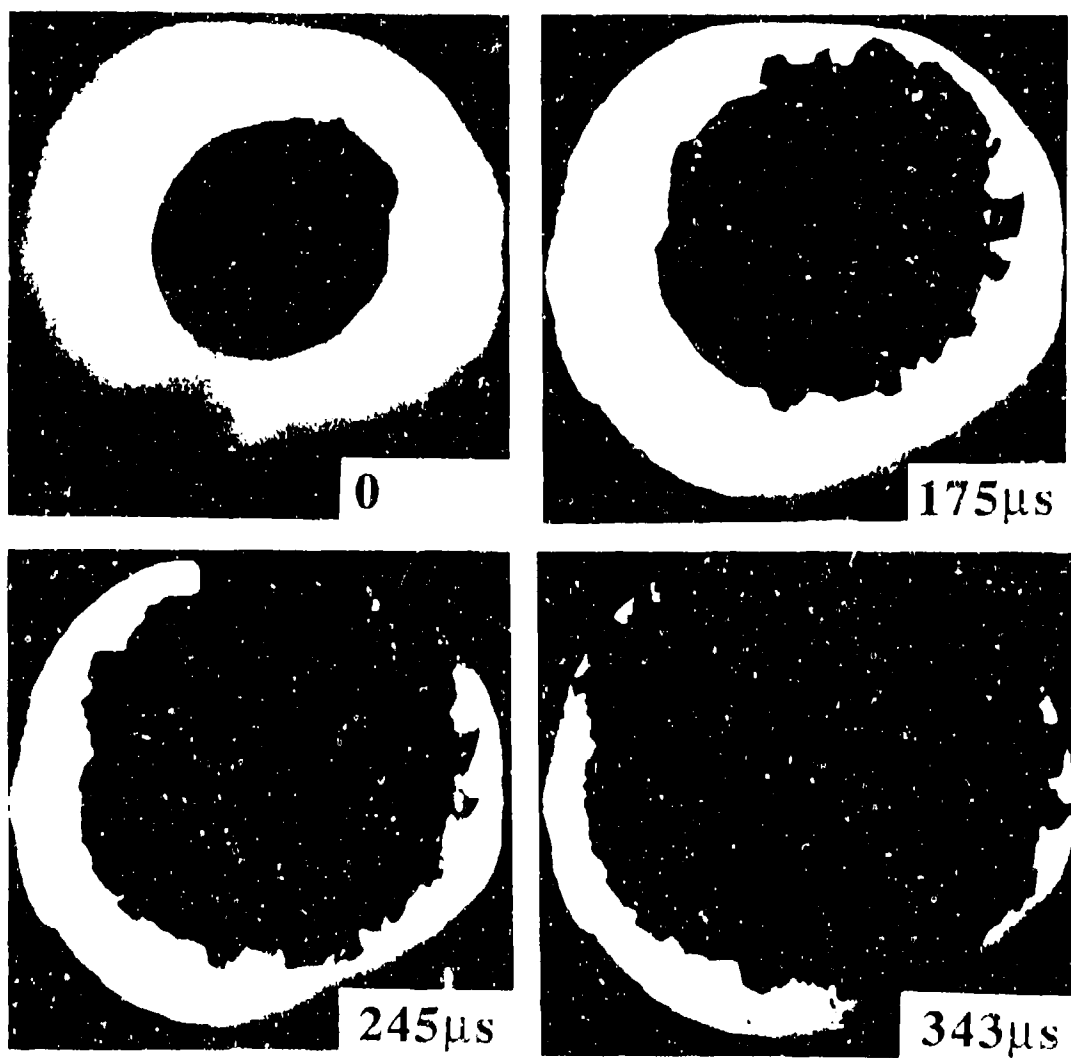
Figure 4 2. Selected frames from a high-speed photographic sequence of the rapid deformation of a disc of XM43 at room temperature.
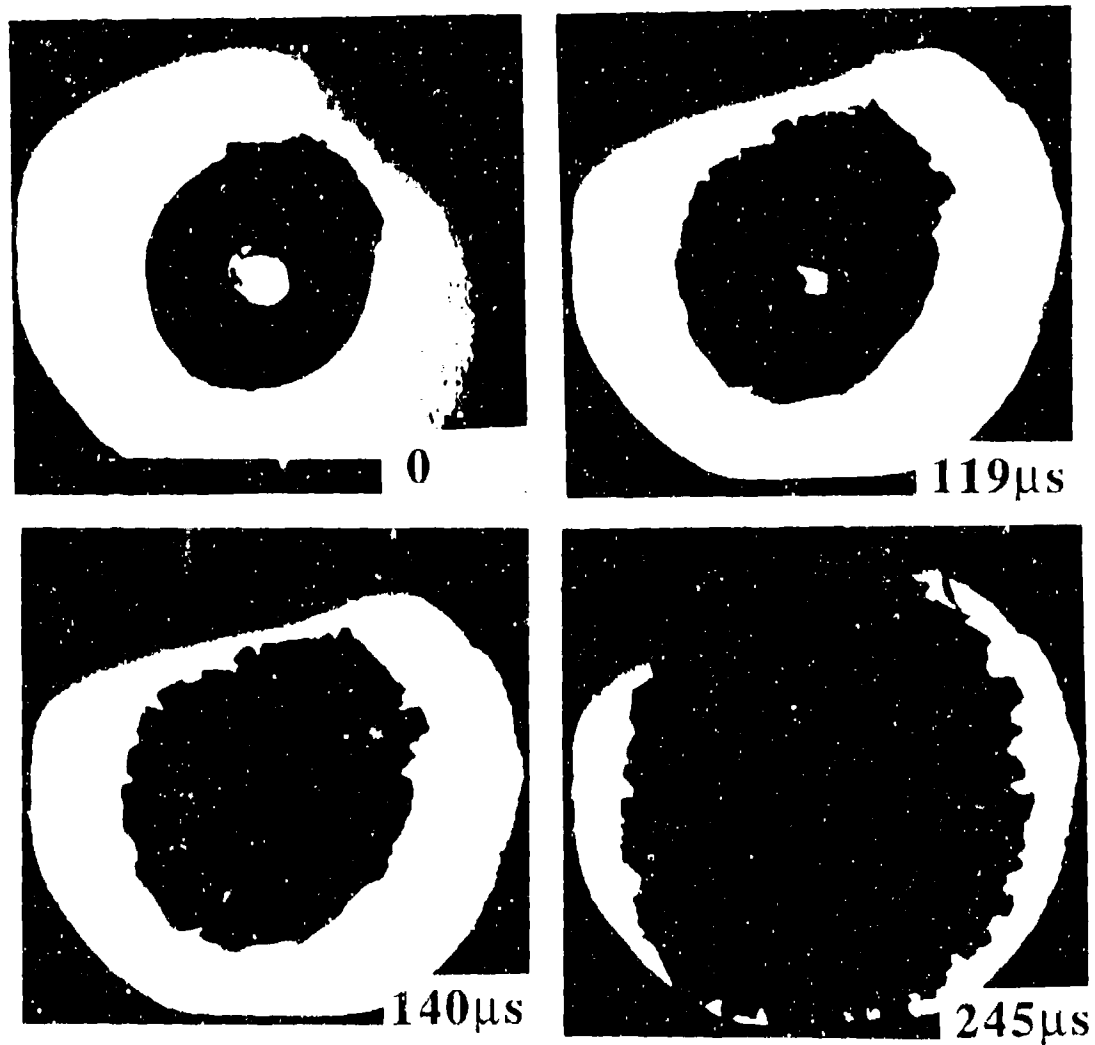
Figure 4.3. Selected frames from a high-speed photographic sequence of the rapid deformation of an annulus of XM43 at room temperature.
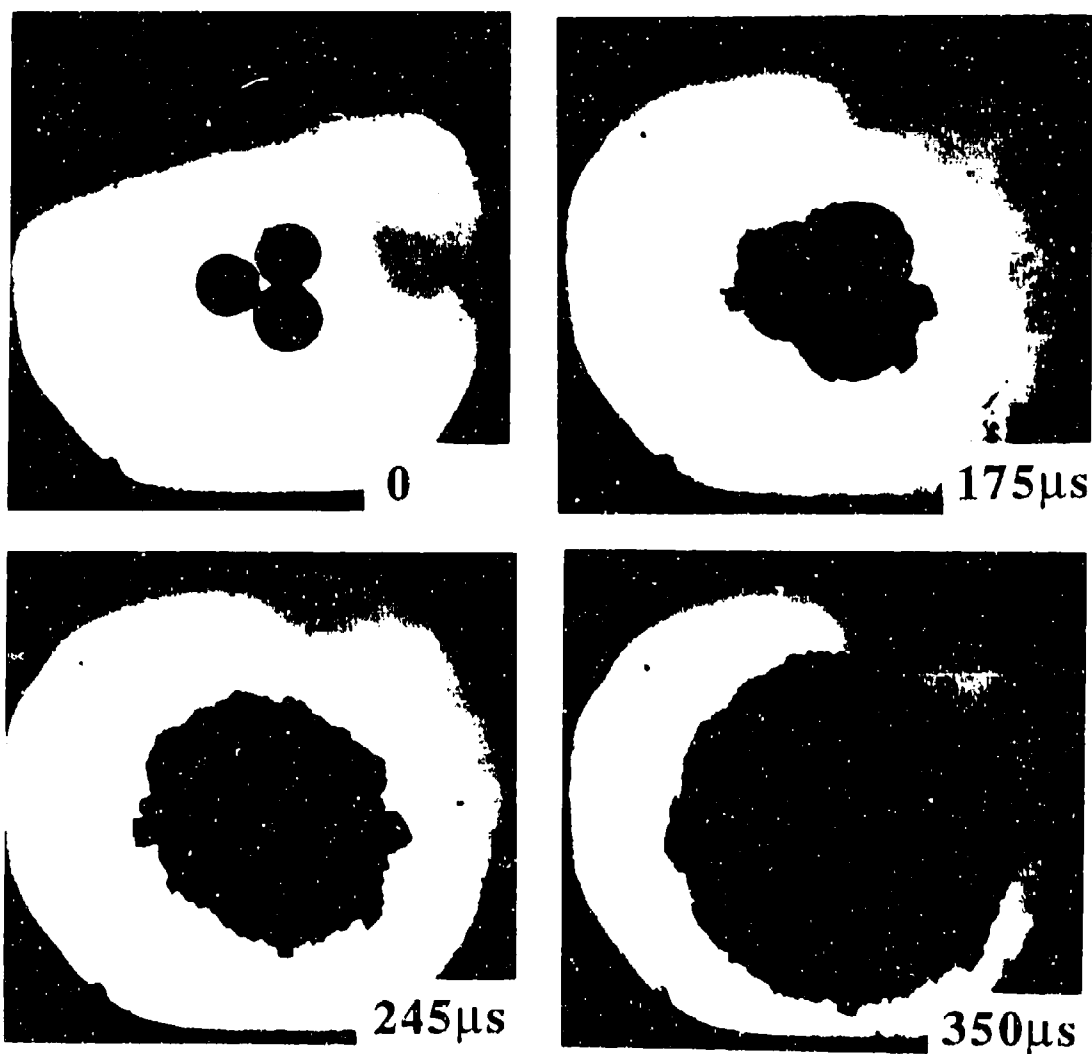
Figure 4.4. Selected frames from a high-speed photographic sequence of the rapid deformation of a triangular array of XM43 at room temperature.
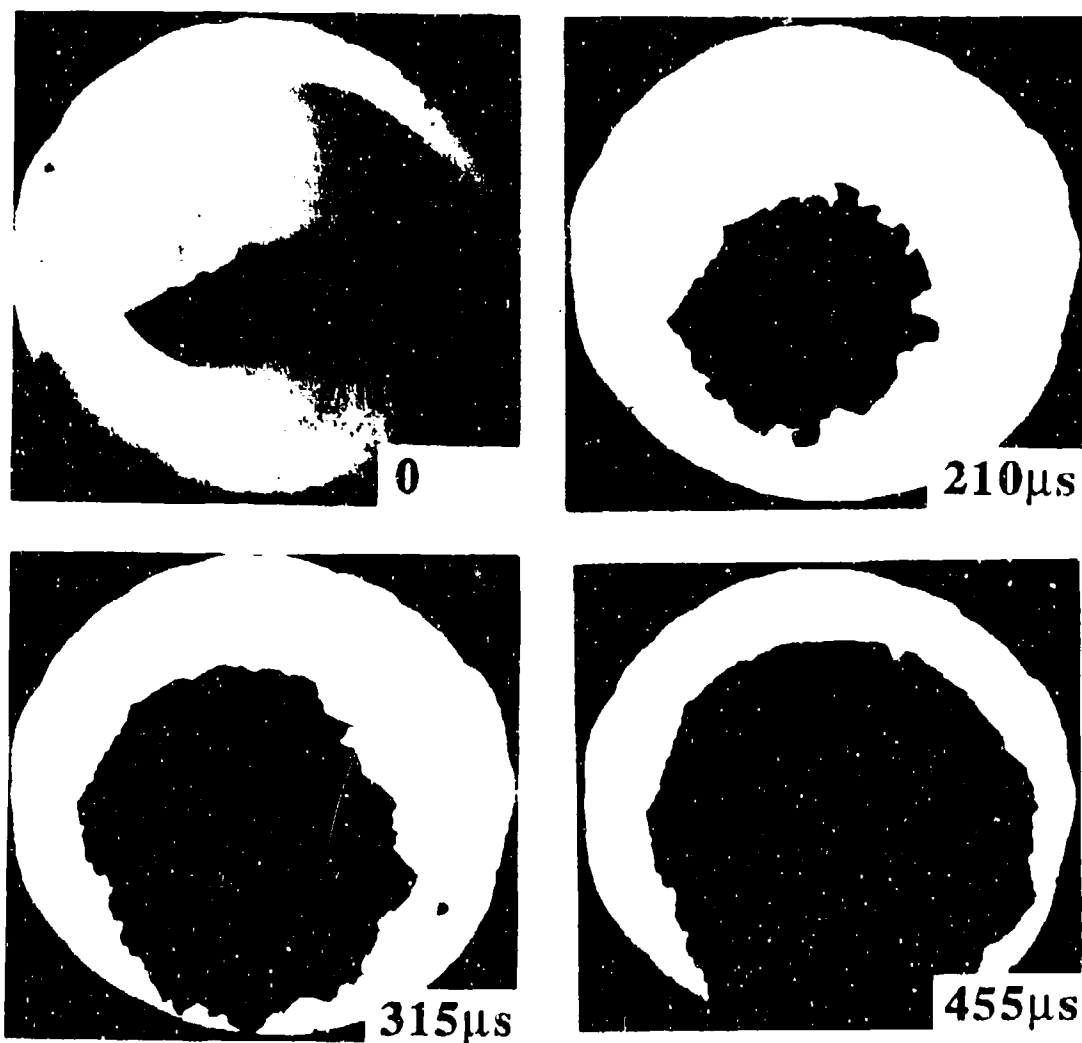
*Figure 4.5. Selected frames from a high-speed photographic sequence of
the rapid deformation of a semicircular fragment of XM43
at room temperature. The first frame shows overwriting.*

Figure 4.6. Selected frames from a high-speed photographic sequence of the rapid deformation of a disc of JA2 at room temperature.

*Figure 4.7. Selected frames from a high-speed photographic sequence of
the rapid deformation of a disc of F300/75 at room temperature.
The first and last frames show overwriting.*

Figure 4.8. Selected frames from a high-speed photographic sequence of the rapid deformation of a disc of T300/75 at room temperature. The first frame shows overwriting.

Figure 4.9. Selected frames from a high-speed photographic sequence of
the rapid deformation of a disc of 1300/25 at room temperature
The first frame shows overwriting.

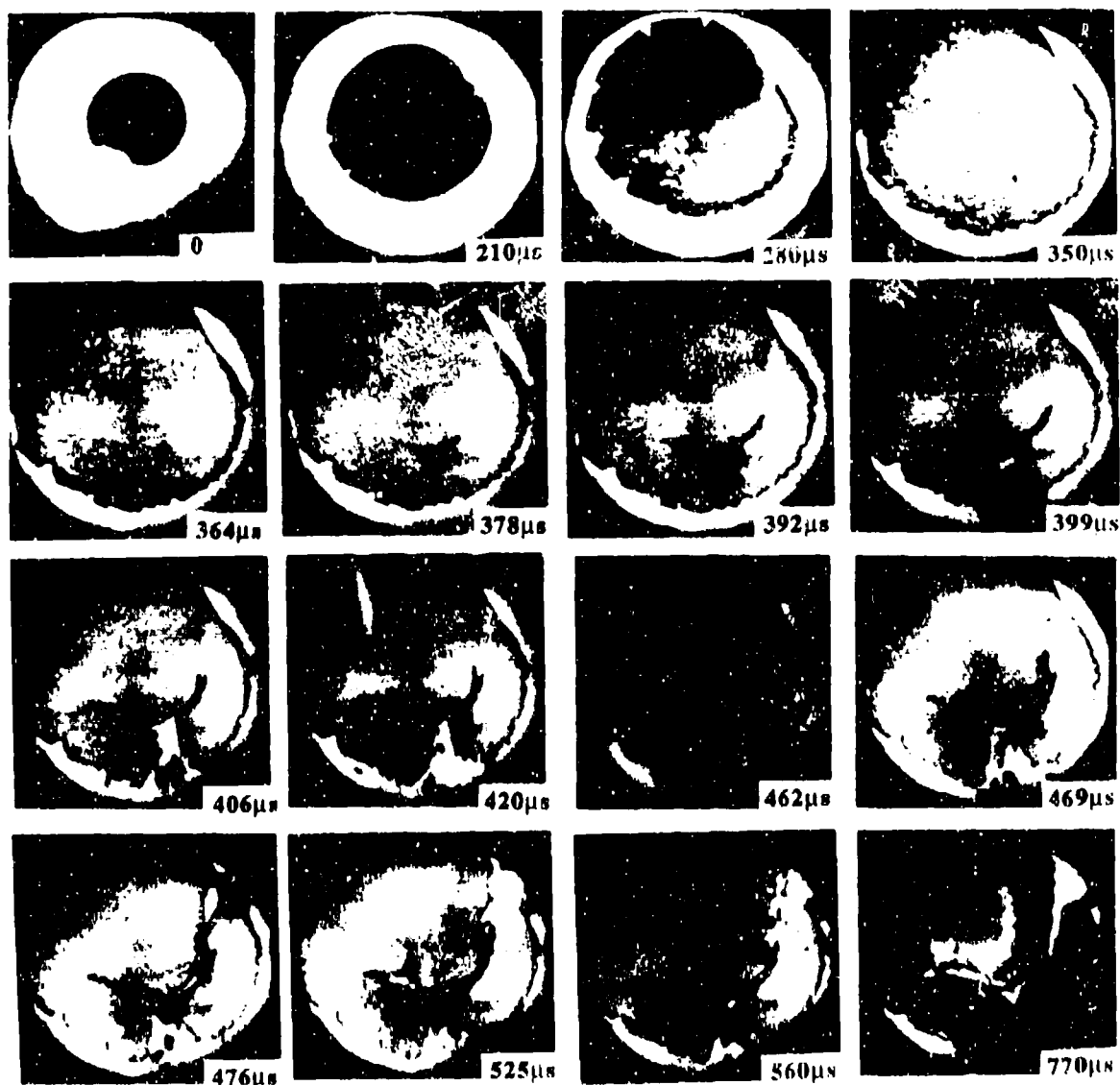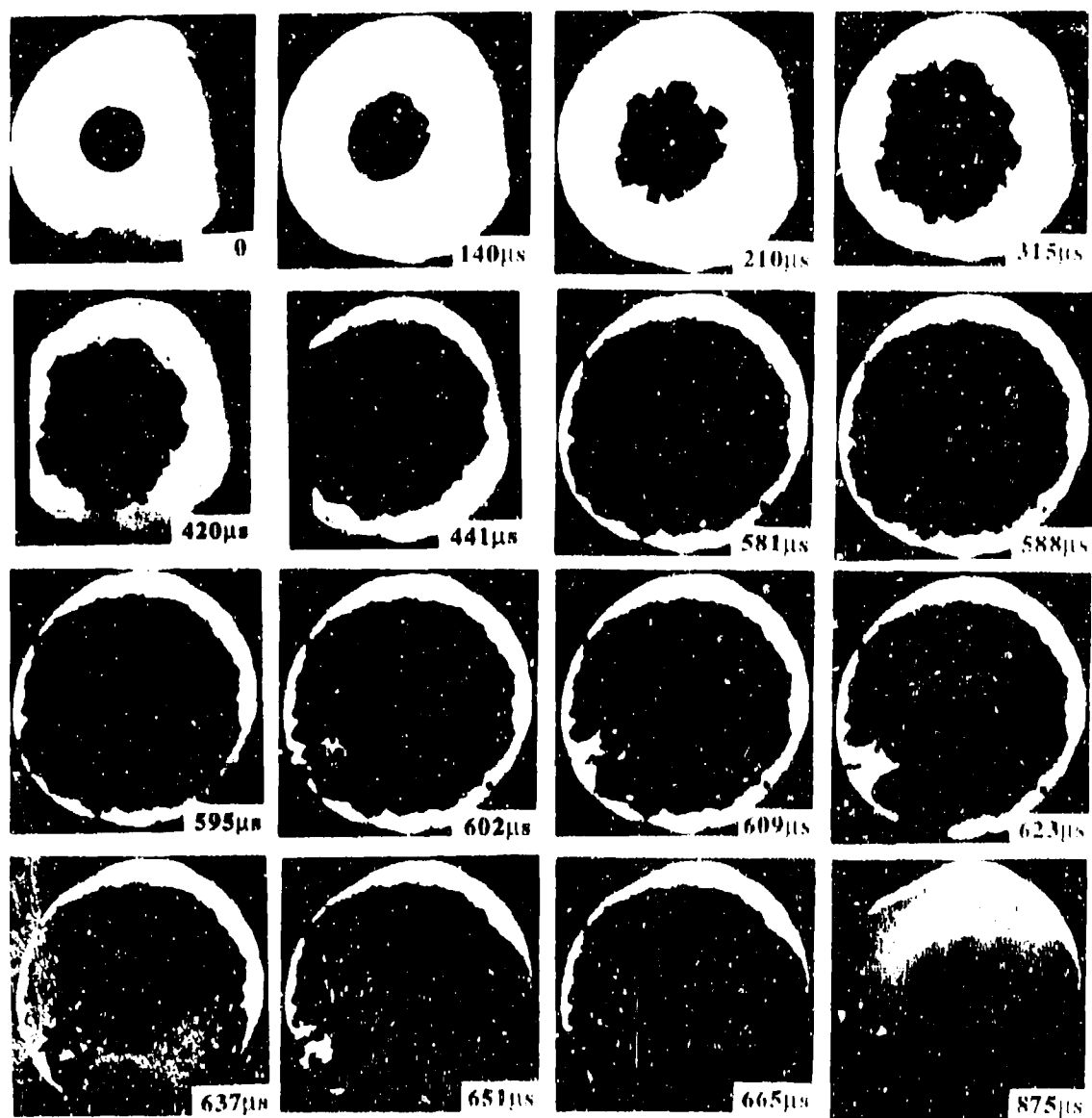Figure 4.10. Selected frames from a high-speed photographic sequence of the rapid deformation of a disc of LM1960 at room temperature. The first and last frames show overwriting.
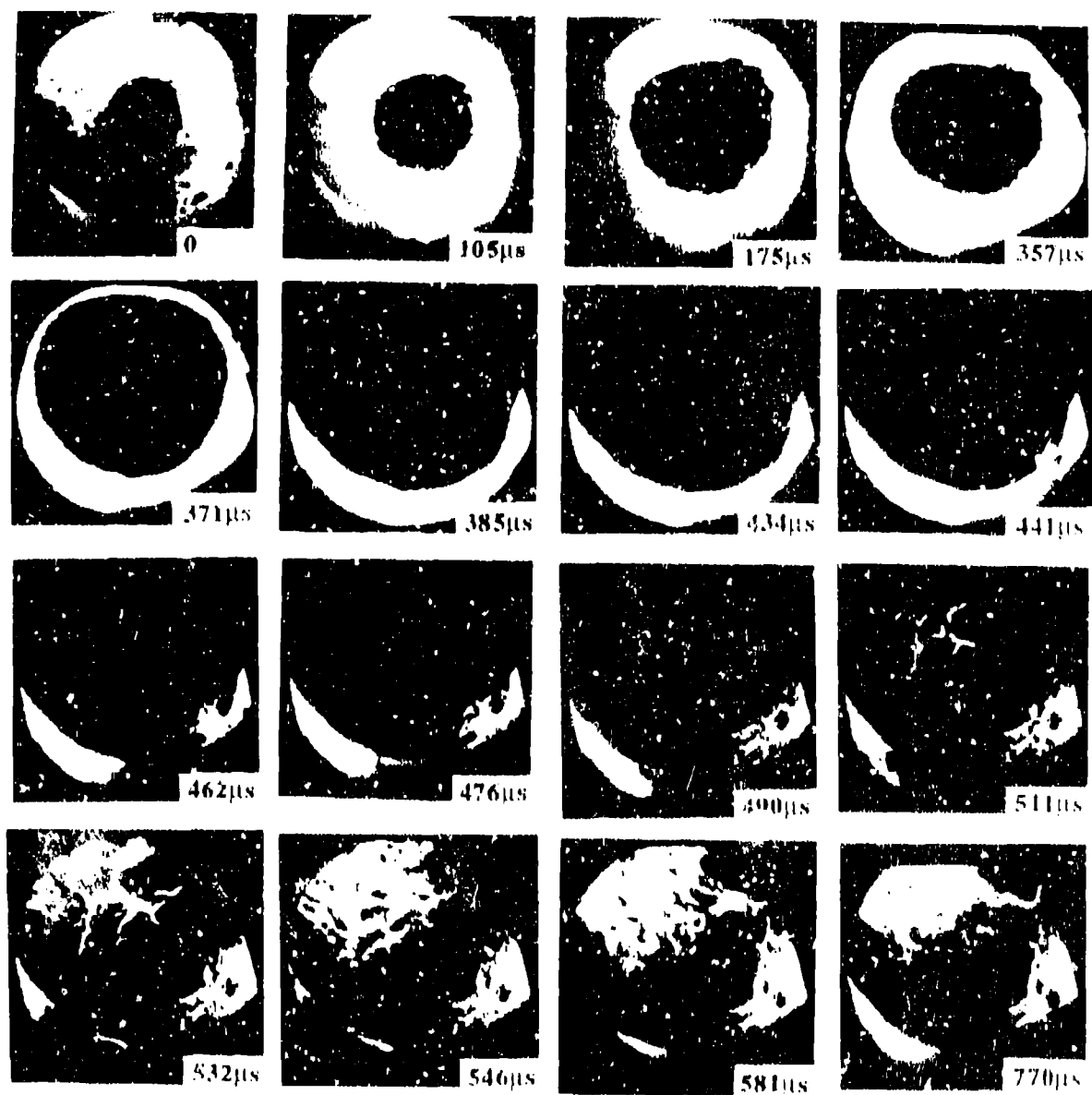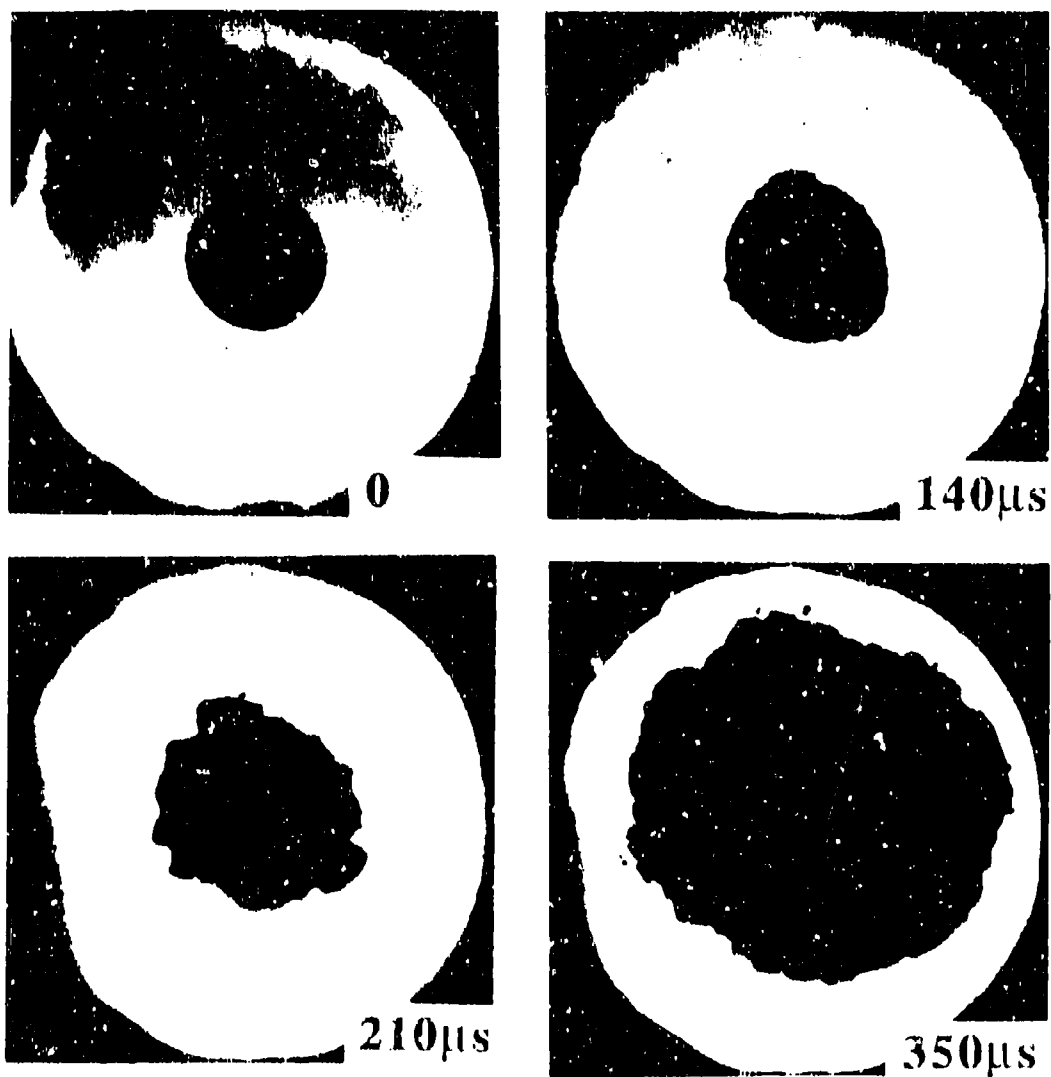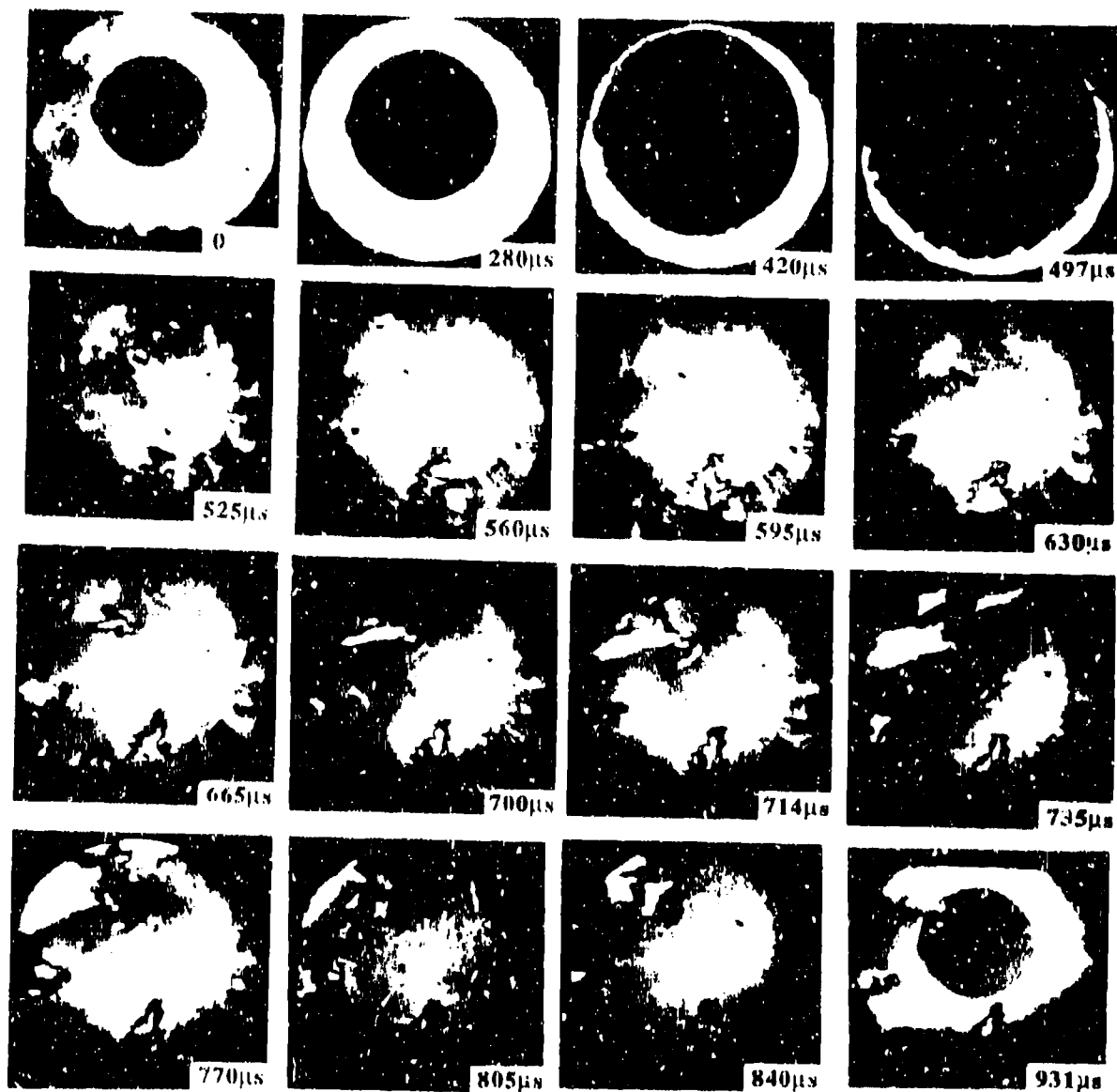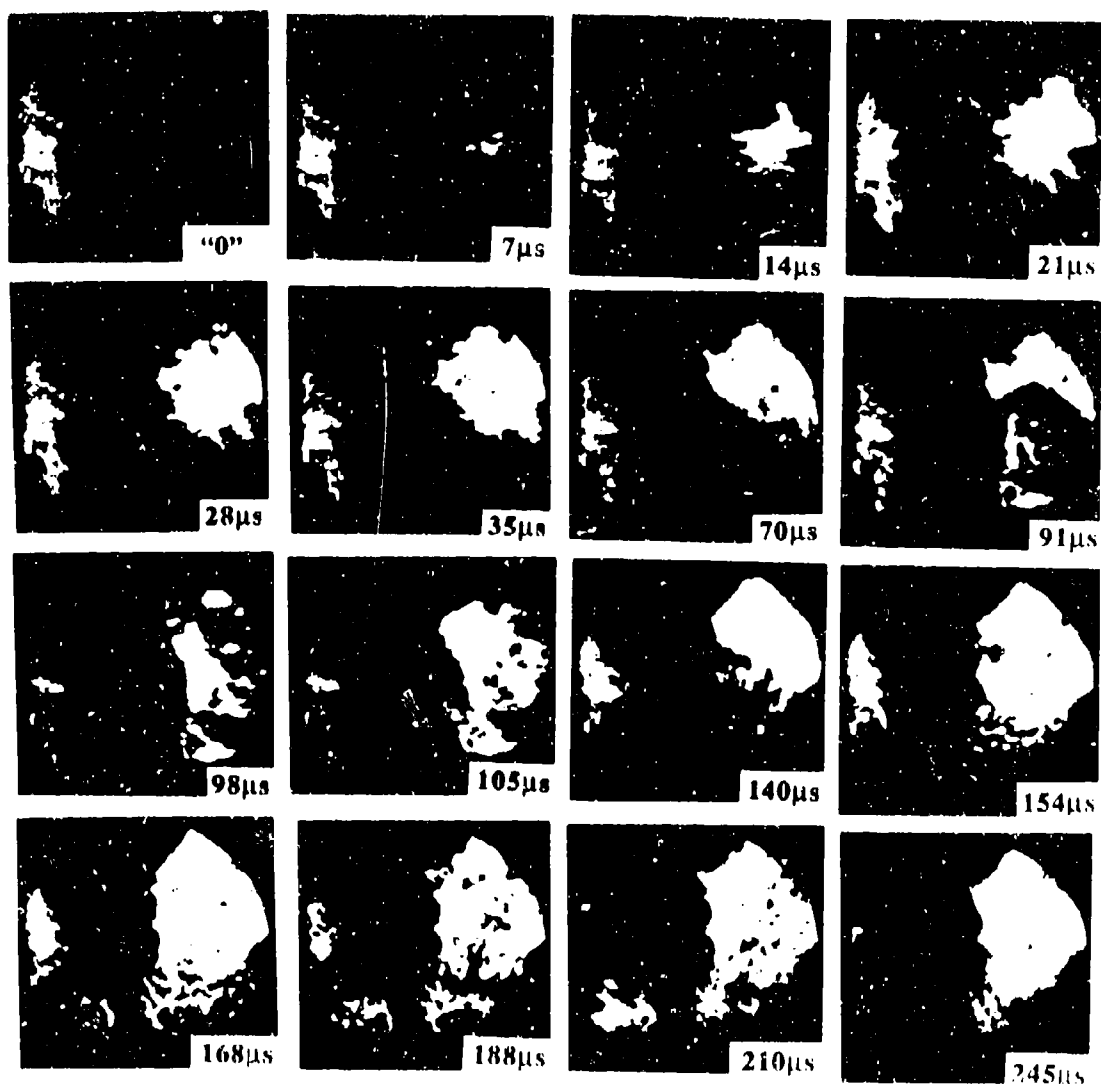
Figure 4.11. Selected frames from a high-speed photographic sequence of the rapid deformation of a disc of JA2 at liquid nitrogen temperatures. The camera triggered late, so the frame labelled "0" is not the true beginning of the deformation.

APPENDIX I

OPTICAL TECHNIQUES FOR STRENGTH STUDIES OF POLYMER BONDED EXPLOSIVES

H.T. Goldrein, J. M. Huntley,
S. J. P. Palmer, M. B. Whitworth,* and J. E. Field
Cavendish Laboratory, Madingley Road,
Cambridge CB3 0HE, U.K.

Optical strain measurement techniques have two significant advantages over conventional strain gauges: they provide whole-field information, and they can be non-contacting. Three techniques have been developed for both quasi-static and dynamic studies of polymers, polymer bonded explosives (PBXs) and propellants: laser speckle photography; high resolution moiré photography; and digital speckle pattern interferometry.

INTRODUCTION

The mechanical testing of materials conventionally involves the use of strain gauges or extensometers attached to the specimen to measure deformation. Extensometers provide an average value over a large section of material, while strain gauges provide a local measurement. Both methods involve attaching devices to the sample, and this often has a significant effect on the sample itself. It is also usually necessary to work with quite large samples (of dimension, say, a few cm) to be able to achieve a measurement.

When working with PBXs or propellants in particular, it is often useful to be able to study smaller samples (to minimise hazard risk), and to be able to measure strain with a non-contacting method. For these reasons the three techniques of laser speckle photography, high-resolution moiré photography and digital speckle pattern interferometry have been developed and applied to a variety of systems.

LASER SPECKLE PHOTOGRAPHY

This is a well-established technique[1] and is the oldest of the three described here, though it involves substantial analysis to extract displacement and strain fields.

The slightly rough surface of the sample is illuminated by an expanded laser beam. The specimen appears speckled, due to light scattered from points on the specimen surface interfering with light scattered from nearby points constructively in some places, and destructively in others. Since these speckles are artefacts of the surface relief, if the relief features move, so too will the speckles. Thus the speckles can be used as markers with which to measure surface displacement.

The tensile strength of the material is then calculated from

A double-exposure photograph of the speckle pattern on the surface of the specimen is taken, with one exposure before, and one after the sample is deformed. On the developed film, many pairs of dots are visible, the separation of the dots in each pair giving a measure of the in-plane displacement vector at that point on the sample. If a point on the film is now illuminated by an undiverged beam of laser light, then a classical Young's fringe pattern will be produced. This diffraction pattern is digitised, and processed by computer (by a two-dimensional fast-Fourier transform) to calculate the spatial frequency and orientation of the fringes.[2] This enables the local displacement vector at the point probed by the laser beam to be derived. The film is then moved (also under the control of a computer) so that the displacement at many points on the film can be determined. Typically, several hundred such fringe patterns have to be processed for each speckle photograph, and there may be many photographs in each deformation experiment. We have recently developed a parallel processing system which can analyse a fringe pattern in 160ms, and one photograph in under a minute.[3]

Applications

For small samples of explosive, it is convenient to carry out mechanical testing in the Brazilian test geometry,[4,5] as illustrated in figure 1.

The test involves the diametral compression of a disc of PBX approximately 10mm in diameter. The sample fails in tension across the line of compression. In this test, the upper anvil is moved downwards at a constant rate of $0.83\mu m\,s^{-1}$ which gives rise to a straining rate of ca. $10^{-4}s^{-1}$.

---

* Now at FMBRA, Rickmansworth Road, Chorleywood, Hertfordshire, WD3 5SH, U.K.

$$\sigma_t = \frac{2P}{\pi Dt}\left\{1 - \left(\frac{b}{R}\right)^2\right\}, \qquad (1)$$

where P is the failure load, b is the contact half-width of the anvils, and D, R and t are the diameter, radius, and thickness of the specimen respectively.

The validity of this equation is based on the assumptions that failure occurs at the point of maximum tensile stress (that is, at the centre) and that the compressive stress has no influence on the failure.
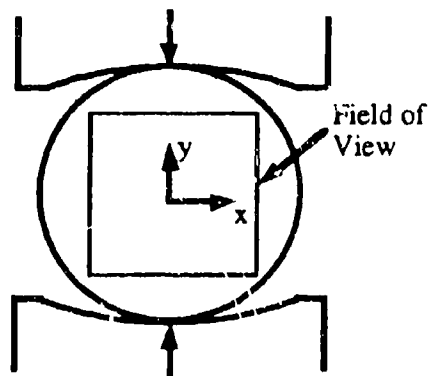

FIGURE 1. BRAZILIAN TEST GEOMETRY

With such a small sample, and with a typical strain-to-failure of a PBX of order 1 millistrain, the displacements which must be measured are only a few microns. The laser speckle technique can measure displacements across the whole of the specimen to an accuracy of better than $0.1\mu m$, and is non-contacting. For these reasons it has proved to be a useful technique for routine testing of PBXs.

Application 1 - Mechanical Testing of PBXs

Figure 2a,b shows the u_x and u_y displacement components of a sample of PBX, (X-0344, composition TATB/HMX/Kel-F 800/dye in the proportions 71.1/23.7/5.0/0.2% by mass), supplied by the Los Alamos National Laboratory. The sample dimensions $(D \times t)$ were 6.5×2mm, and the sample had been under load in the Brazilian test for 270 s. The contour spacing is $0.5\mu m$ in figure 2(a), and $1.0\mu m$ in figure 2(b). The region illustrated corresponds to the square in figure 1. From the displacement fields illustrated in figure 2, the strain fields can be deduced by numerical differentiation. The tensile strain distribution ε_{xx} at the centre of the same disc under increasing load is illustrated in figure 3. Plates (a)–(d) represent ε_{xx} at 108, 162, 216 and 270 s respectively. The contour spacing is 0.25 millistrain. Strain at the centre of the sample can be measured from these maps, and stress can be calculated from the load measured by a load cell in the testing machine. Thus stress-strain curves can be plotted as illustrated in figure 4.

Application 2 — Perforated Propellant Grains

A second illustration of the technique is the study of inert samples supplied by the United States Army Research Laboratory at Aberdeen, of perforated propellant grains, in order to study the contribution of the hexagonal array of burn holes to the mechanical properties. The sample was placed between two flat anvils, with its circular face (containing the array of burn holes) lying in the plane of the anvils. The specimen was loaded in compression by moving the upper anvil at a constant rate of $0.83\mu m\,s^{-1}$ up to a maximum load of 40kg. The field of view is illustrated in figure 5.
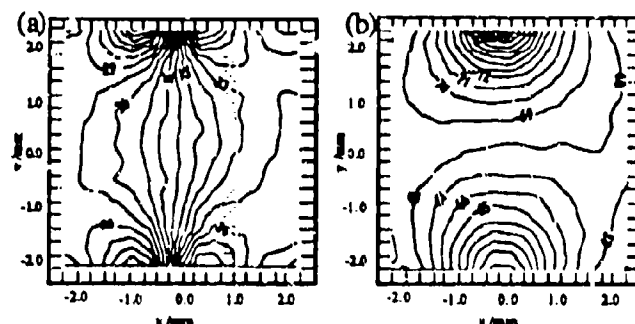

FIGURE 2. u_x (a) AND u_y (b) DISPLACEMENT COMPONENTS OF X-0344 UNDER LOAD IN THE BRAZILIAN TEST
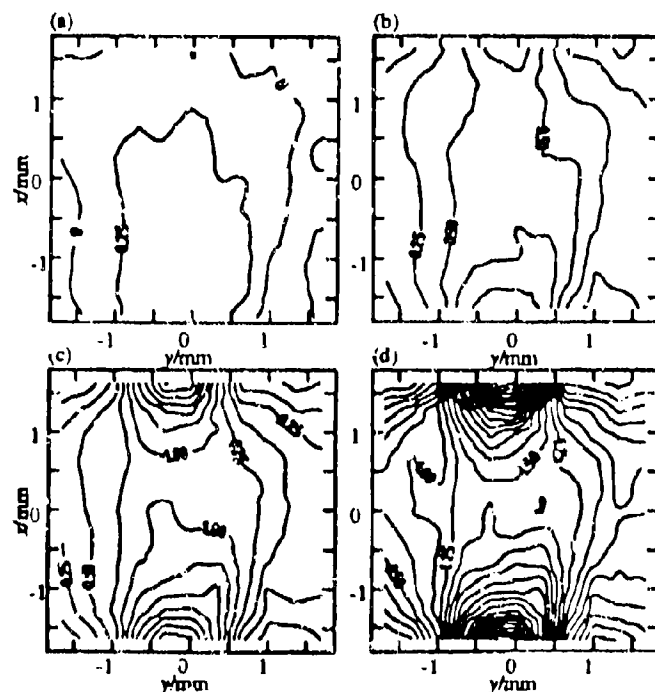

FIGURE 3. TENSILE STRAIN DISTRIBUTION ε_{xx} AT THE CENTRE OF A DISC OF X-0344
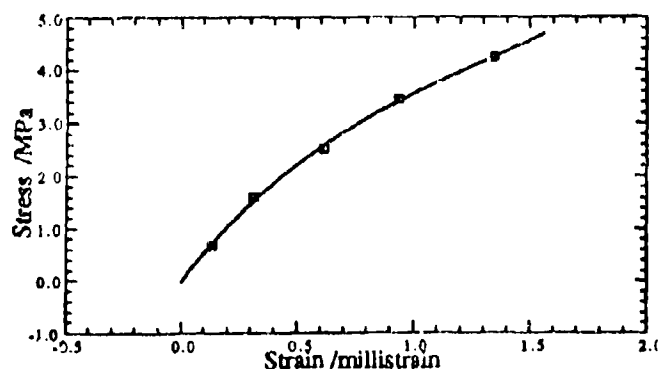
FIGURE 4. STRESS/STRAIN CURVE FOR X-0344
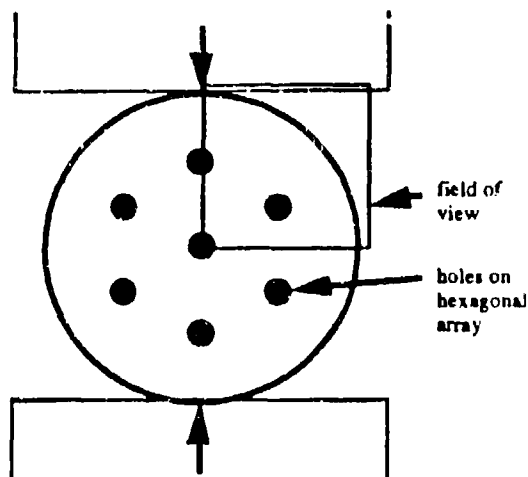DERIVED FROM BRAZILIAN TEST

FIGURE 5. LOADING GEOMETRY FOR
PERFORATED PROPELLANT GRAINS.

In the displacement maps which appear as figure
6, it can be seen that strain is beginning to build up in
the region under the anvil, the compressive strains
here being approximately 2.0 millistrain. The u_x plot
also shows some stress concentration between the
burn holes.

Application 3 — High Speed Speckle Photography

The previous applications have all dealt with
quasi-static deformation of the sample. It is also
possible to use speckle photography to record
dynamic deformation events. A Beckman & Whitley
189 rotating-mirror high-speed camera and pulsed
ruby laser have been modified for such a study.[6]

A pulse of light from a small flash tube placed
inside the camera is arranged to illuminate a
photodiode at the edge of each of the 25 relay lenses
in the camera. This can only happen when the
rotating mirror is pointing directly at the appropriate
frame. The photodiodes then repeatedly Q-switch a
ruby laser, which illuminates the sample, and records
a speckle pattern. The camera is run once with the
sample stationary, and once with the event in
progress, thus double exposure speckle photographs

are produced. These are then developed and
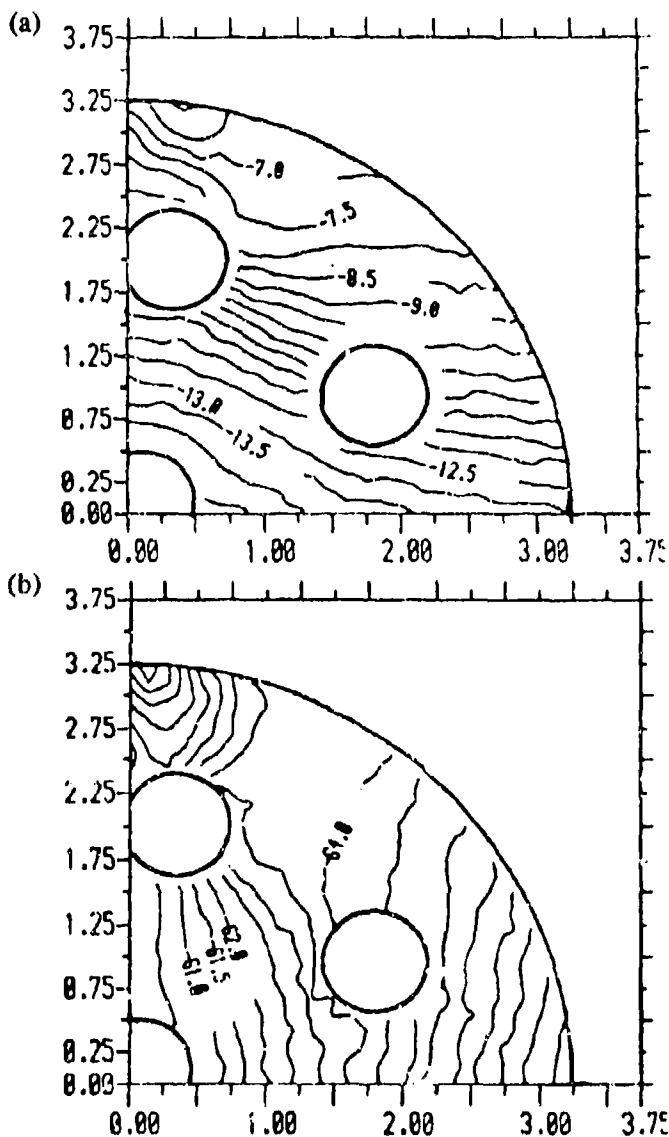analysed as before.

(a)

(b)

FIGURE 6. CONTOUR PLOTS OF IN-PLANE
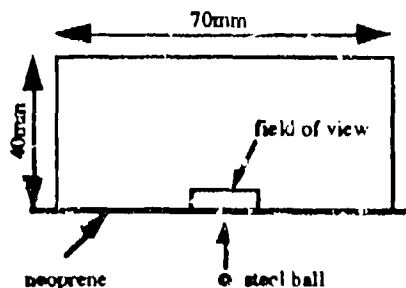DISPLACEMENT COMPONENTS u_x (a) AND u_y
(b) AT A LOAD OF 31.9 kg

FIGURE 7. SPECIMEN GEOMETRY
FOR BALL IMPACT EXPERIMENTS.

In this example, experiments were carried out to
measure the displacement field induced in a plate by
solid particle impact. Figure 7 illustrates the
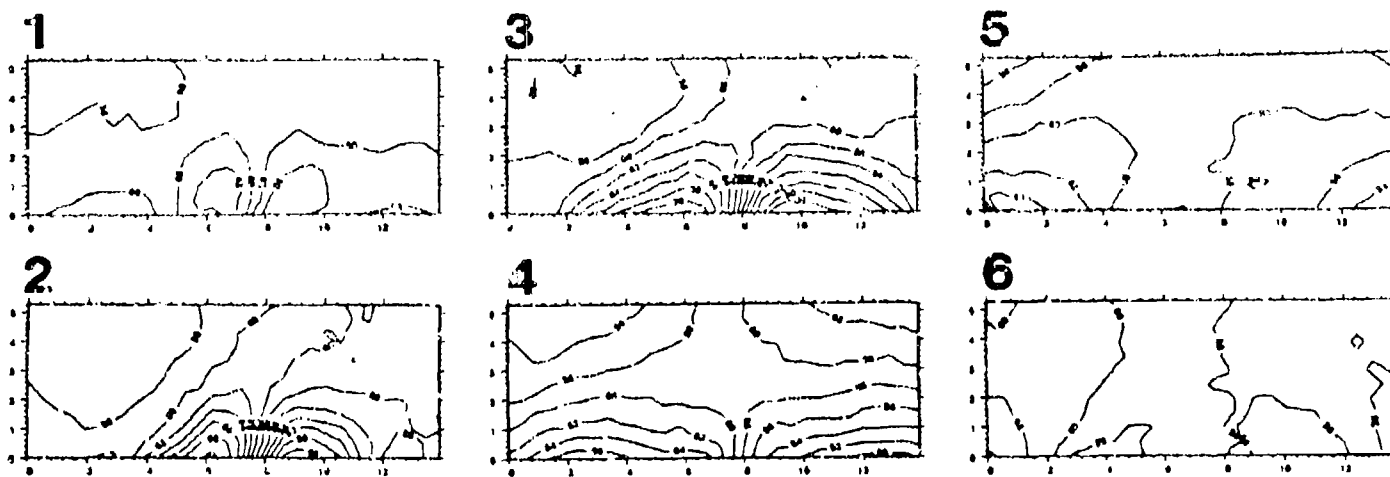geometry. The specimen was machined from a 6 mm

FIGURE 8. HORIZONTAL DISPLACEMENT COMPONENT FROM BALL IMPACT ON PMMA.

sheet of cast polymethyl methacrylate (PMMA). The projectile, a 2mm steel ball impacted with a velocity of 115 ± 10 m s^{-1}.

The results giving the horizontal displacement field from this experiment are illustrated in figure 8. The interframe time is 1.65 µs, the field of view is 14×5.5 mm^2, and the contour interval is 2 µm.

HIGH RESOLUTION MOIRE PHOTOGRAPHY

When two gratings are superimposed, beating between the gratings gives rise to a so-called moiré fringe pattern. In experimental mechanics this effect is used to measure in-plane displacements, out-of-plane slope, and surface form.[7] For example, in-plane displacements are determined by bonding a grating to the specimen surface. The fringe pattern formed by superimposing a stationary reference grating, either by direct contact or by imaging through a relay lens, then represents a contour map of the displacement component perpendicular to the grating lines. The sensitivity (i.e. fringe contour interval) is equal to the pitch of the specimen grating: with conventional moiré photography the maximum practical grating frequency is around 40 lines mm^{-1} (l mm^{-1}), corresponding to a sensitivity of 25 µm fringe^{-1}. In the high resolution moiré technique[8,9] a masked lens is used to image the specimen grating. The lens and mask are designed to operate at a magnification of 1:1, with a frequency of 150 l mm^{-1} in both the specimen and image planes. Real time fringes are then recorded with a high speed camera allowing displacements to be measured with a sensitivity of 6.7 µm fringe^{-1}, and with microsecond time resolution. This masked lens is illustrated in figure 9.
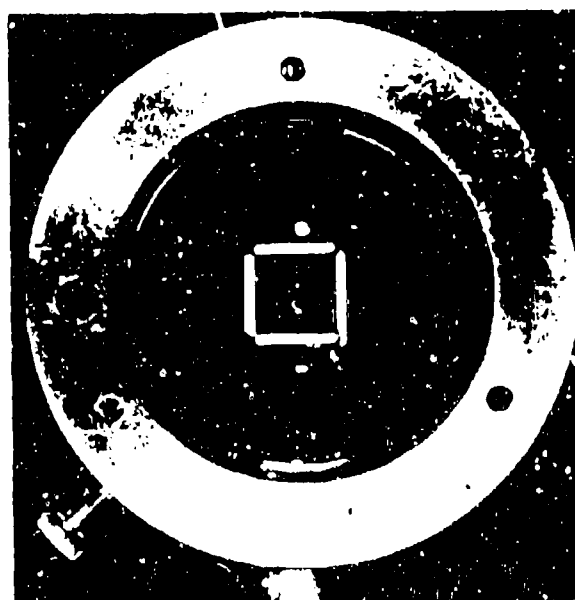
FIGURE 9. OBJECTIVE LENS WITH SLOTTED MASK FOR IMAGING HIGH FREQUENCY (150 LINES MM^{-1}) SPECIMEN GRATINGS

Figure 10 shows the imaging system used. The masked lens (OL$_i$) images the specimen grating (SG) onto the reference grating (RG), forming real-time moiré fringes, which are recorded by a high speed camera (HSC), an Imacon 792. Illumination is provided by a Xenon flash lamp (X) and beam-splitter (BS). FL$_1$ and FL$_2$ are field lenses. The theory of fringe formation is described in reference 9. The specimen grating is a thin reflective phase grating, formed either in epoxy resin, or (for low modulus samples) silicone rubber.

The recorded patterns are digitised and then analysed by computer, using a 2-D Fourier transform technique[8,9].

One problem to which the high resolution moiré photography technique has been applied is the study of dynamic fracture of a rectangular PMMA plate containing a long crack. When loaded by a tensile stress pulse along one edge, a dilatational pulse enters the plate, trailed by shear waves which initiate at the plate edges as the pulse passes. High resolution moiré photography has been used to measure the displacement field in the vicinity of the (stationary) crack tip as the pure dilatational pulse passes. Figure 11 shows the high resolution moiré fringe patterns recorded by a high speed camera over a 25 mm × 25 mm field of view centred on the crack tip. The first fringe pattern was recorded only 10.5 μs after the arrival of a dilatational pulse incident from the left. Thus little displacement has occurred, and the fringes are only slightly modified from the mismatch fringes. Towards the end of the sequence, the fringes become more closely spaced, indicating increasing tensile horizontal strain (ε_{xx}). The interframe time is 5 μs.

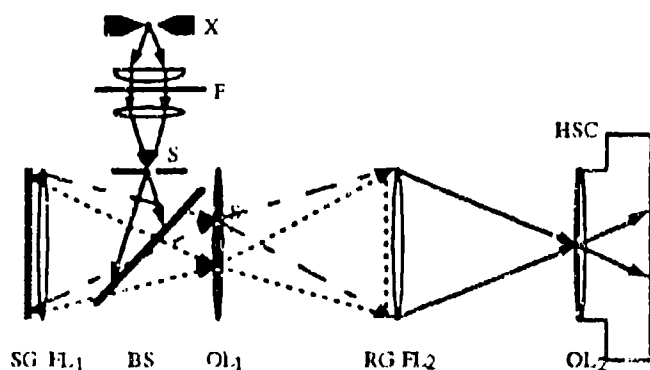FIGURE 10. EXPERIMENTAL ARRANGEMENT FOR HIGH RESOLUTION MOIRE PHOTOGRAPHY.
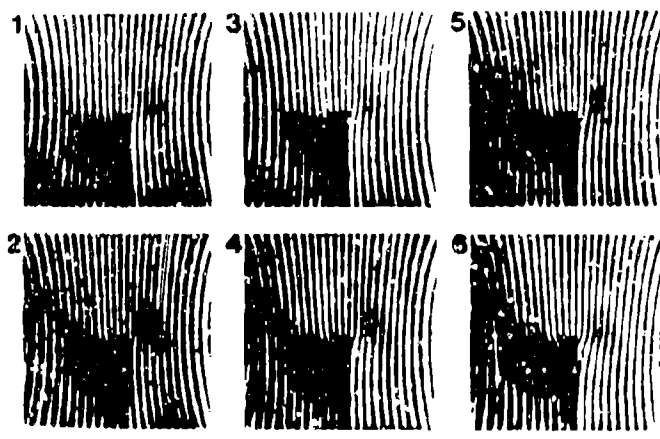

FIGURE 11. MOIRE FRINGE PATTERNS OBSERVED AT THE CRACK IN A PMMA PLATE

The horizontal component of the in-plane displacement field has been calculated as a function of time from these fringe patterns and from the corresponding mismatch fringes; it is shown in figure 12 as a sequence of contour maps, where dimensions are in mm, and the contour heights are in μm. The magnitude of the strain field can be seen to increase with time from the initial application of the dynamic load.
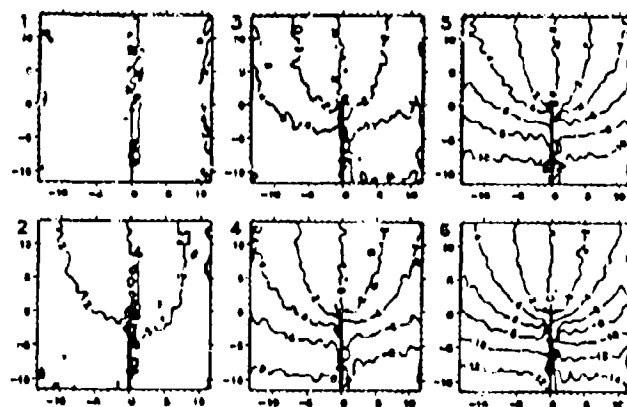
FIGURE 12. CONTOUR PLOTS OF THE HORIZONTAL IN-PLANE DISPLACEMENT COMPONENT OBTAINED FROM ANALYSIS OF FIGURE 11.

From these displacement fields, the mode-I stress intensity factor K_I^d can be calculated. It was compared with a theoretical solution based on a strain-gauge record of the input stress profile and the expected response for step pulse loading of an elastic plate. The predicted and measured K values are in agreement to within 5 to 10%.

Application 2

A second example is given by experiments carried out to investigate the effect of impact by rectangular projectiles on composite disc specimens. The discs simulate 2-D sections through artillery shells. The discs are 5 mm thick and consist of a central polycarbonate region with a diameter of 15.9 mm, 19.1 mm, or 22.2 mm, surrounded by a copper ring of external diameter 25.4 mm and wall thickness 1.6 mm. The intervening region was filled with a silicone rubber liner. Epoxy reflection gratings were applied to the polycarbonate region, and the aim was to measure the level of strains that were present in the polycarbonate region for different thicknesses of rubber. Phosphor bronze projectiles were fired by means of a rectangular bore gas gun, giving projectile velocities of 56.0 ± 1.1 m s^{-1}. High speed sequences, corresponding to each of the rubber thicknesses were recorded. By way of example, figure 13 shows the 19.1mm disc with a rubber thickness of 1.55 mm. The impact occurred horizontally from the left; the gratings were vertical so the fringes represent the horizontal displacement component, and compressive strains show up as a decrease in the fringe spacing. With a specimen grating frequency of 150 lines mm^{-1}, the sensitivity is 6.7 μm fringe^{-1}. Only the central

polycarbonate region is visible. The interframe time is 5 µs. A compressive stress wave can be seen entering the polycarbonate from the left, crossing the disc in approximately 15 µs. Figure 13 was analysed by the Fourier transform method, and the displacement field measured from the eight frames is shown in figure 14, where the contour interval is 2 µm. Though not all the results are shown here, these experiments demonstrated the substantial reduction in strains which can be achieved through the use of a liner.

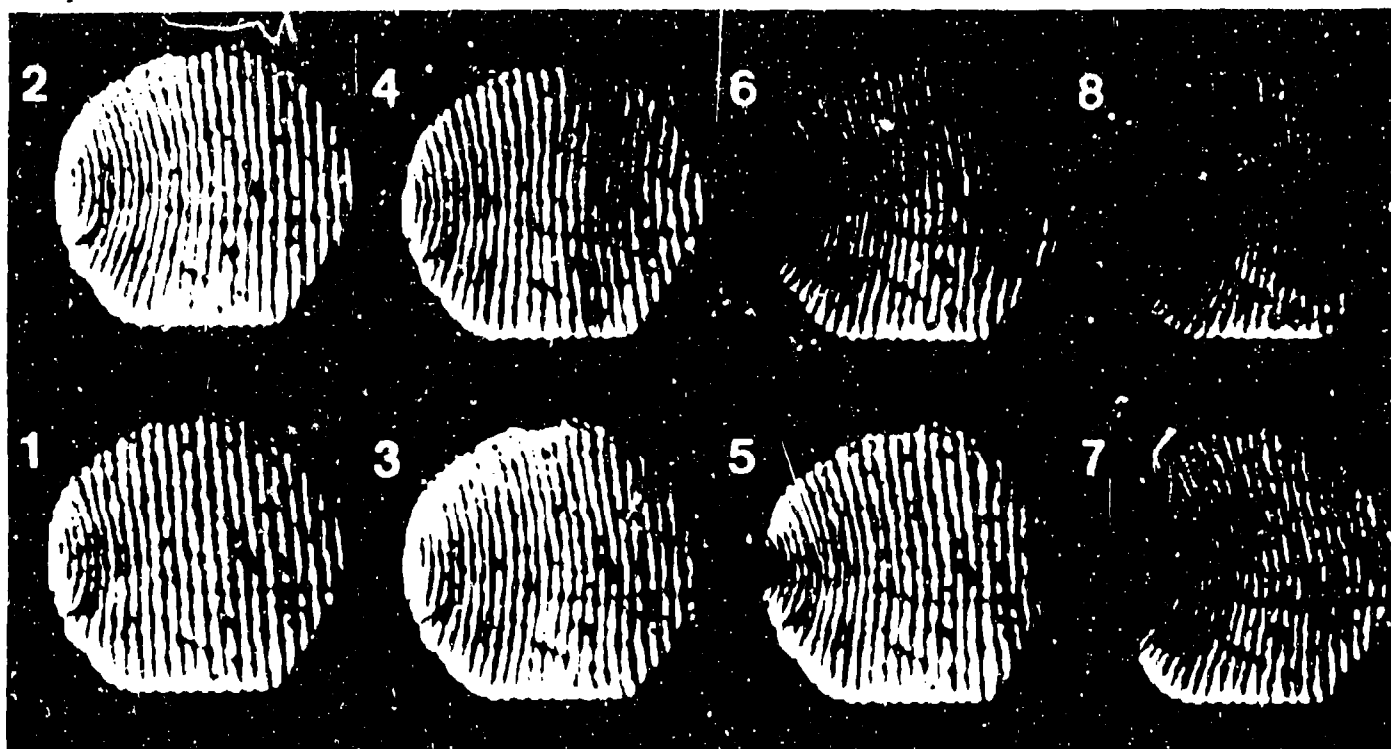FIGURE 13. HIGH SPEED MOIRE SEQUENCE OF A COMPOSITE DISC UNDERGOING SLIDER IMPACT FROM LEFT TO RIGHT. INTERFRAME TIME = 5µs.
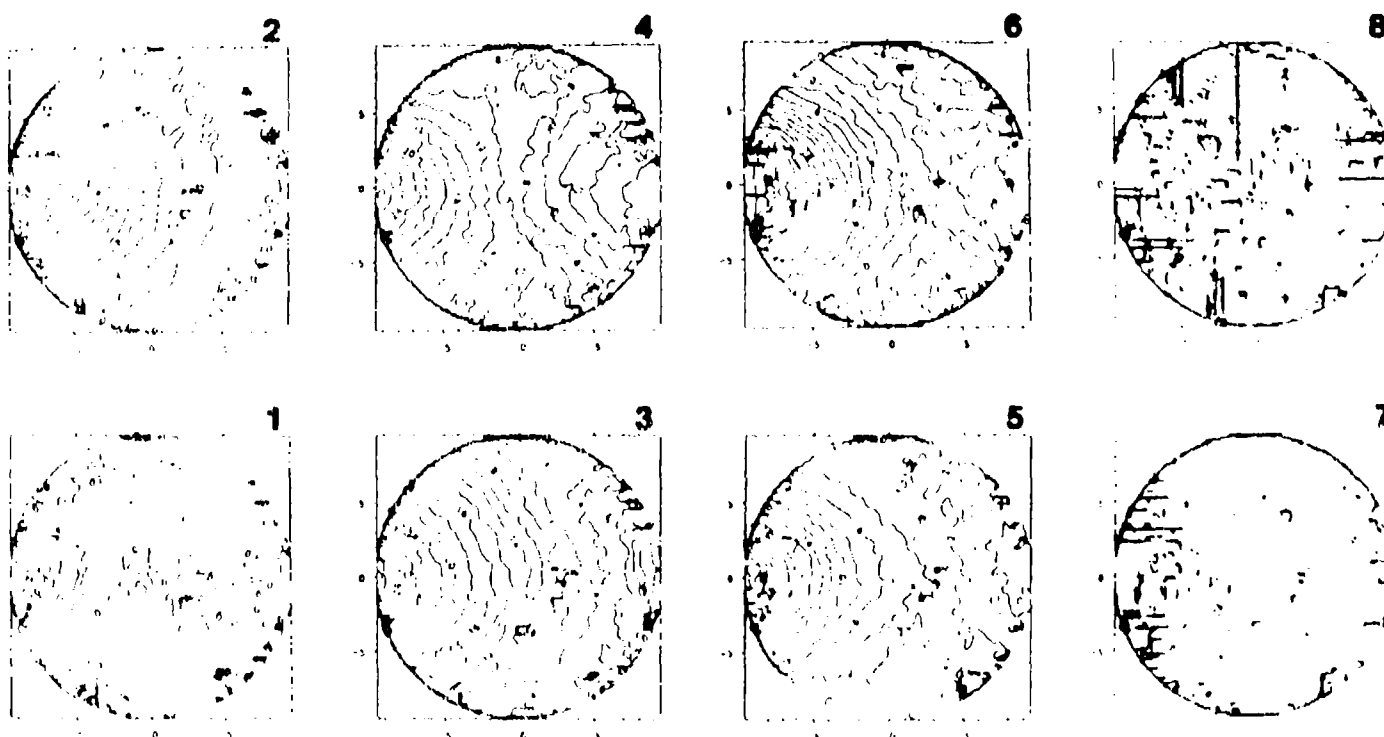

FIGURE 14. CONTOURS OF HORIZONTAL DISPLACEMENT COMPONENT FOR THE HIGH SPEED SEQUENCE SHOWN IN FIGURE 13. CONTOUR INTERVAL = 2µm.

DIGITAL SPECKLE PATTERN INTERFEROMETRY

In digital speckle pattern interferometry, the sample is illuminated by two collimated beams of light as shown in figure 15. The resulting pattern of illumination is a set of cosine-squared fringes, modulated by a speckle pattern which is formed as described earlier. The camera of an image-processing system is focused on the surface of the specimen to observe these patterns. The fringe spacing is $\lambda/(2\sin\alpha)$ where λ is the wavelength of light being used, 633nm in this case and α is the angle of incidence. If α is approximately 20° then the grating spacing is approximately 1μm. This is too fine for the camera to resolve and only the speckle pattern is visible.

If the sample is subjected to an in-plane displacement, then the speckles move as has already been noted with speckle photography. However, as the points contributing to their intensity move across the fine cosine grating, the intensity of the speckle will also vary sinusoidally at the grating frequency. If a speckle moves by 1μm, then it will change from bright to dark, and then to bright again. If the phase angle of the speckle along this sinusoid can be determined, then so too can the motion. There are three unknowns in this determination: the minimum intensity, the maximum intensity, and the phase angle, so one observation will not yield sufficient information to determine the phase uniquely. To provide this extra information, the length of one arm of the interferometer is altered by known fractions of a wavelength using the phase modulator shown in figure 15 and at least three measurements must be made. A sensitivity of order tens of nanometers is possible.
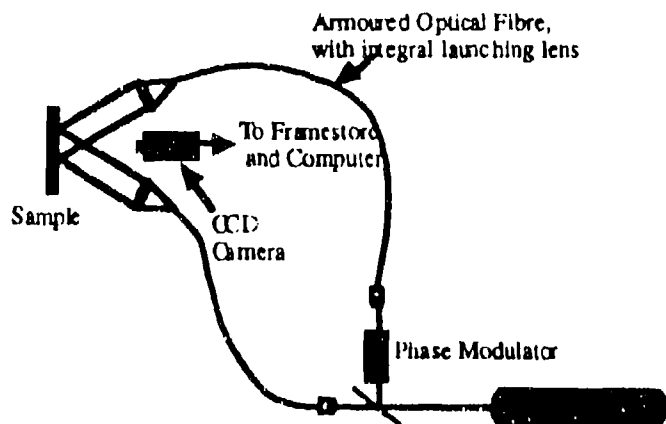
FIGURE 15. OPTICAL ARRANGEMENT FOR SPECKLE INTERFEROMETRY

The main disadvantages of this are that at least three phase-stepped images must be acquired between which the specimen must not undergo any significant motion, so restricting the method to quasi-static tests, and that only one component of displacement can be obtained.

Applications

Brazilian test experiments were performed on inert PBX simulants in order to compare the effect of the polymer binders on the mechanical properties. The interferometer was configured to measure horizontal in-plane displacements with a sensitivity of 0.433 μm fringe[-1]. The Brazilian test loading rig was started, and phase-stepped speckle patterns were recorded every 25 s during the deformation. A sequence of such incremental phase maps for a composition with an hydroxy-terminated polybutadiene binder is shown in figure 16 in which black represents phase values of $-\pi$, and white is $+\pi$. Each map shows the change in horizontal displacement component that occurred in the 25 s between successive exposures. One fringe corresponds to a phase change of 2π and a relative displacement of 0.433 μm. The initial fringes are essentially horizontal, indicating rigid body rotation of the disc. Tensile strain in the horizontal direction is proportional to the phase gradient in the x direction; the build-up of strain at the centre of the disc is clear from the tilting of the fringes to the vertical in that region. In the last frame the phase map has become very noisy at the centre of the disc.

FIGURE 16. WRAPPED PHASE MAPS OF INERT PBX IN THE BRAZILIAN TEST

We believe this to be due to fracturing of the specimen, giving rise to excessive displacement and surface tilt, and hence to speckle decorrelation

.Subsequent analysis involves phase unwrapping (i.e. removal of the 2π phase discontinuities) and numerical differentiation to calculate strain fields. Figure 17 shows maps of ε_{xx} calculated from the frames of figure 16. The contour interval is 1 millistrain.
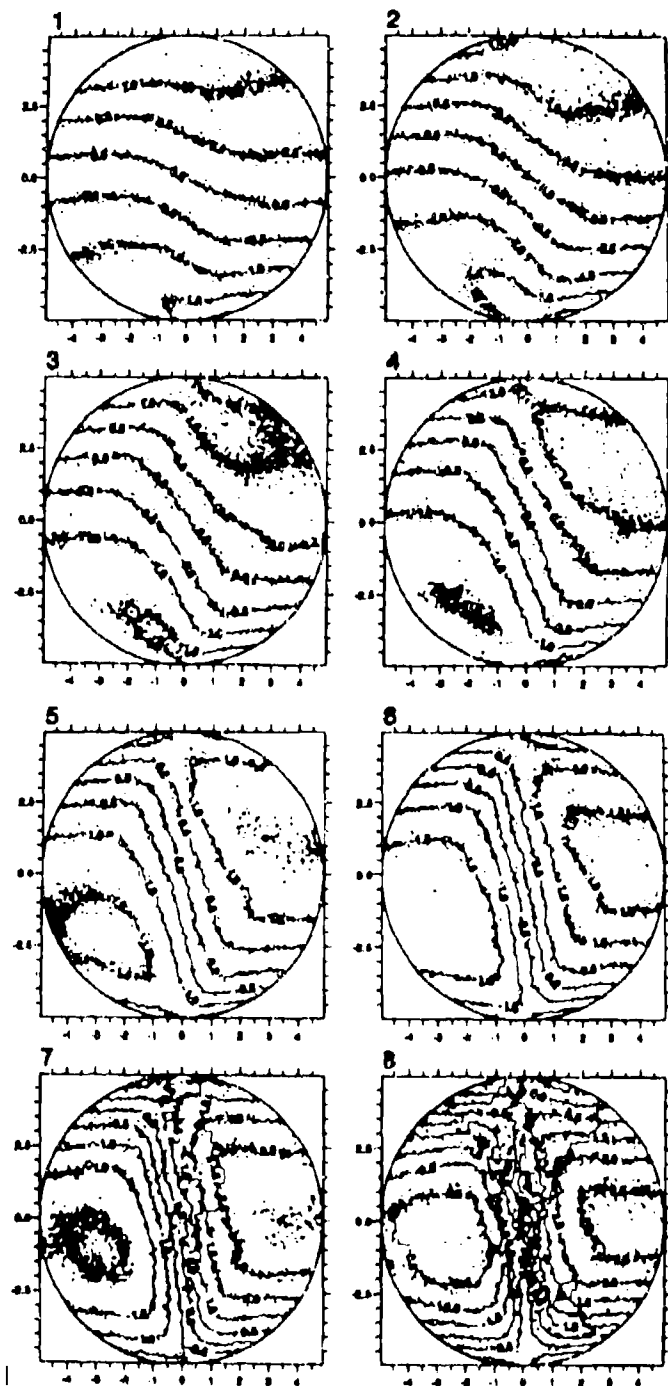
FIGURE 17. STRAIN MAPS DERIVED FROM FIGURE 16

REFERENCES

1. Dainty, J.C., Ed., *Laser Speckle and Related Topics in Applied Physics* Vol. 9, Springer Berlin, 1975, pp. 203-253.

2. Huntley, J.M., Palmer, S.J.P., Field J.E., "Automatic Speckle Photography Fringe Analysis: Application to Crack Propagation and Strength Measurement", *Proc. SPIE*, Vol. 814. 1987, pp.153-160.

3. Huntley, J.M., Goldrein, H.T., Benckert, L.R., "Parallel processing system for rapid automated analysis of speckle photography and particle image velocimetry data", *Applied Optics* (in press).

4. Field, J.E., Parry, M.A., Palmer, S.J.P., Huntley. J.M., "Deformation and Explosive Properties of HMX Powders and Polymer Bonded Explosives", *9th Symposium (International) on Detonation*, Office of Naval Research, Portland. Oregon, Sept 1989, pp. 886-896.

5. Palmer, S.J.P., Field, J.E., and Huntley, J.M., "Deformation, strengths and strains to failure of polymer bonded explosives", *Proceedings of the Royal Society of London A*, Vol. 440, 1993, pp. 339-419.

6. Huntley, J.M., and Field, J.E., "High speed laser speckle photography, *Proc SPIE*, Vol. 1554A, 1991, pp. 756-765.

7. Sciammarella, C. A., "The moiré method - a review," *Experimental Mechanics*, Vol. 22, 1982, pp. 418-433.

8. Huntley, J.M., and Field, J.E., "High resolution moiré photography: application to dynamic stress analysis", *Optical Engineering*, Vol. 28, 1989, pp. 926-933.

9. Whitworth, M.B., and Huntley, J.M., "Dynamic stress analysis by high resolution reflection moiré photography", *Optical Engineering*, (submitted April 1993).

SIMULATED FRAGMENT ATTACK ON CASED MUNITIONS

Pauline Roberts*, J.E. Field.

Cavendish Laboratory,
Madingley Road,
Cambridge, CB3 0HE.
England.

*also DRA, Fort Halstead, Nr. Sevenoaks, Kent, England.

The mechanisms which, under simulated fragment attack, can lead to ignition in sections of cased charges have been studied using high-speed photography. The front-end geometry and velocity of the projectiles, the casing material and explosive filling of the target were altered to determine their effect on these mechanisms.

INTRODUCTION

The response of cased munitions to high velocity impact is an area of major concern to weapon designers. The impact, caused by bullet or shrapnel fragment during either intentional or accidental attack can elicit a variety of responses from the munition. The most violent response is the prompt shock initiation of the explosive filling, leading to detonation of the whole charge. If the shock pressure resulting from the impact is not high enough to shock initiate the charge, it may nevertheless penetrate the casing and cause ignition of the charge within. This may or may not be followed by a deflagration-to-detonation transition (DDT), depending upon the degree of confinement, which will in any case have been reduced by the impact, and the nature of the explosive filling. The impact, whether it penetrates the casing or not, may not cause a sustained ignition of the filling though it is still possible that the damage which results from this impact may increase the sensitivity of the charge to further impacts.

The series of experiments detailed here address the problem of observing inside a cased charge whilst it is undergoing simulated fragment attack at impact velocities below which shock initiation is caused. Shock initiation mechanisms have been extensively investigated due to the seriousness of response. Early work by Dewey and Slade[1] and Brown and Whitbread[2] using right circular cylinders fired at bare and lightly-covered explosives, impacting on the flat end of the cylinders, showed that the critical velocity for initiation of the sample was independent of the length of the projectile, as long as the length was greater than about half the diameter. If the material of the projectile was changed, then the critical velocity was altered so that the impact shock pressure remained constant.

If the charges were more heavily confined, Howe et al.[3] found that shock initiation did not always explain the detonation thresholds that were observed, and that the length of the projectile was important when considering explosive fillings such as TNT, where shear effects were also found to contribute to the initiation process.

Cook et al.[4] have carried out much work in this area, particularly on the effect of the charge casing on the munition's response. They have shown that for thin barriers of steel and aluminium, it is possible to model initiation using a modified 1-D critical energy-per-unit-area criterion, but that for initiation through thicker barriers, this model is not applicable. Liang et al.[5] used the DEFEL 2-D finite element dynamic code incorporating the Mie-Gruneisen equation of state to calculate the pressure and temperature distributions within explosive charges impacted by flat-ended projectiles. They found that shock initiation mechanisms were dominant for bare charges, but that for heavily confined charges, viscoplastic heating of the explosive was important and that adiabatic shear band heating in the explosive near the periphery of the plug was a possible ignition mechanism.

Using thin barriers, Haskins et al.[6], in projectile attack trials on PE4, investigated whether altering the front-end projectile geometry affected the critical velocity for initiation. They concluded from theoretical and experimental results that flat-ended projectiles, which transmit a 1-D shock into the explosive, were the most efficient at causing initiation. Projectiles with cone angles of less than ~120°, which have a subsonic contact periphery velocity, and flat-ended projectiles impacting thick barriers, produce divergent shocks in the explosive material and are therefore less efficient at causing initiation. They also investigated the effect of charge-liner materials and found that rubber liners reduced the impact shock, providing the rubber's Hugoniot curve did not lie between that of the casing and the explosive.

At impact velocities below the shock initiation threshold, there is the possibility of the charge undergoing a wide variety of reactions from DDT to

ricochet of the projectile with no apparent reaction. Although the hazard will generally decrease with lowering impact velocity, any response, from DDT to burning leading to case venting, may be transmitted to other munitions stored in close proximity. The initial impact may thus escalate from a small-scale event into a more devastating large-scale accident. Much work has been carried out by Boggs et al.[7] into quantifying the range of responses a munition may exhibit under various stimuli, including bullet and fragment attack, so that a mechanistic understanding of the reactions and predictive capability could be achieved for a given munition. Whilst most of the research effort has understandably been concentrated on the most hazardous SDT and DDT responses, the aim of the experiments detailed in this paper was to investigate and understand the mechanisms which cause ignition of the charge in the first place. Further responses were noted but are not the primary interest of this work.

EXPERIMENTAL

There are a number of putative mechanisms for ignition, including heating due to rapid viscous flow ahead of the projectile, adiabatic shear band formation and heating of the explosive filling in contact with the points of casing failure. In order to isolate the effects of these mechanisms, various parameters and conditions in the experimental arrangement were altered. High-speed photography was used to observe directly the ignition sites and give a photographic insight into the ignition mechanisms.

The front-end geometry of the impacting projectile was varied in three ways to alter the flow conditions and shear stresses ahead of the projectile. The projectiles were either flat-ended, hemispherical-ended or 30° cone-ended (see Table 1). A flat-ended projectile would be expected to cause shear failure of the casing and push the plug of casing ahead of the projectile into the explosive. This geometry was also expected to cause the highest amount of shear stress and viscous flow in the filling. At the other extreme, a 30° cone-ended projectile should cause tensile failure of the casing, followed by penetration of the filling by the projectile and the deformed points at casing fracture. In the case of the hemispherical-ended projectile, the

casing should undergo tensile and shear failure under impact and the explosive filling would be affected by shear stresses and rapid viscous flow ahead of the projectile though to a lesser extent than for the flat-ended projectile.

In order to isolate the effect of whether the casing fracture surfaces cause ignitions in the explosive, the casing of the target was cut at the projectile entry point, leaving effectively a bare charge. The targets were then tested for their response to the three types of projectile.

The effect of casing material (see Table 2) was also investigated by using both copper and steel. Due to the different physical properties of these two materials and their different modes of failure (copper undergoing ductile failure at higher strain rates than steel, which is more prone to brittle fracture) it was thought that the casing material may alter the likelihood of ignition.

Voids were introduced between the casing and the filling and at varying distances from the casing within the filling to assess their effect on the sensitivity of the target to ignition. These voids were included to simulate the effect of voids occurring in charges through debonding from the casing and imperfect processing.

The impact experiments were performed using a single-stage, twin-solenoid operated gas-gun with helium as the propellant gas because of its low molecular weight. The gun barrel was 2 m long and of 13.2 mm bore. The projectiles were made of silver steel (density 7.8 g cm^{-3}) and sabot-driven to keep the mass of explosive to a minimum to comply with safety constraints. The sabots were made of nylon 666 rod (density 1.1 g cm^{-3}) with a recess for the projectile at the front and material reamed out at the rear to reduce the weight of the combination, as shown in figure 1. The projectile was fired at the target at velocities in the range 350 to 650 m s^{-1}. Although the flat-ended projectile imparts a shock into the explosive filling, it is below the critical shock initiation pressure and therefore shock initiation was not expected to occur.

In addition to varying the front-end geometry of the

TABLE 1. FRONT-END GEOMETRY AND DIMENSIONS OF PROJECTILES

front-end geometry	diameter (mm)	length (mm)	mass (g)
flat	5.2	16	2.6
hemispherical	5.2	16	2.4
30° cone	5.2	20	2.3

TABLE 2. PHYSICAL PROPERTIES OF THE TARGET CASING MATERIALS

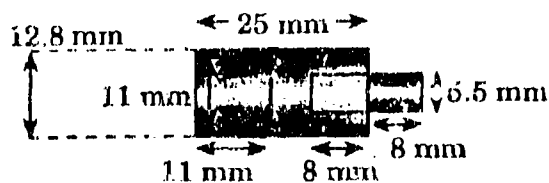| casing material	density (g cm^{-3})	Young's modulus (GPa)	thermal conductivity (J s^{-1} m^{-1}K^{-1})	specific heat capacity (J kg^{-1} K^{-1})
copper	8.91	130	390	390
steel (mild)	7.86	210	50	470

FIGURE 1. SCHEMATIC DIAGRAM OF THE SABOT-PROJECTILE COMBINATION.

projectiles, the impact velocities were varied to determine whether different mechanisms become more dominant at different velocities.

There were 5 types of explosive filling used as targets. as detailed in table 3.

The targets were 19 mm diameter × 6 mm thick discs of explosive, encased by 1.5 mm of either copper or mild steel and sandwiched between two 10 mm thick blocks of polycarbonate, as shown in figure 2. The blocks also acted as sabot strippers, although as a result,

TABLE 3. TARGET FILLINGS.

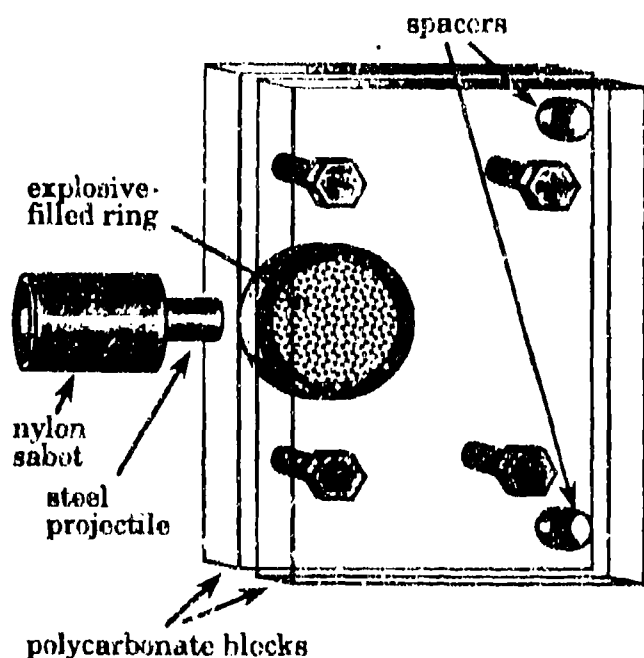| explosive	composition (wt %)	density ($g\,cm^{-3}$)
PE4	RDX (88%)/grease (12%)	1.60
cyclotol	RDX (60%)/TNT(40%)	1.68
octol	HMX(70%)/TNT(30%)	1.80
LX-14	HMX (95.5%)/estane (4.5%)	1.83
PBX	HMX (88%)/binder (12%)	1.74

FIGURE 2. SCHEMATIC DIAGRAM OF THE TARGET ARRANGEMENT.
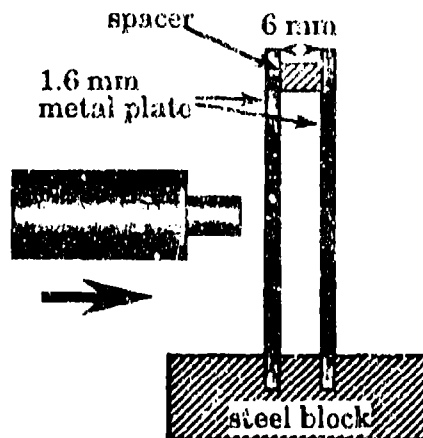
FIGURE 3. SCHEMATIC DIAGRAM OF THE PROJECTILE PENETRATION TARGET ARRANGEMENT.

a second shock was imparted to the explosive on impact of the sabot. The effect of this impact is clearly visible in some shots, but since it occurred at least 15 µs after the projectile had impacted, it had no effect on the initial ignition mechanisms.

Projectile penetration experiments, to determine the amount of kinetic energy lost by the projectile in this process, were also performed on sheets of copper and steel of the same thickness as the target casings. These experiments were performed using metal sheet/air gap/metal sheet and metal sheet/cyclotol/metal sheet arrangements for comparison (see figure 3).

The velocity of the projectile was measured by timing it between two laser beams a known distance apart. The timer was connected to an up-down counter which was used to fire the camera at the correct time, irrespective of projectile velocity.

The impacts on targets were recorded using an Imacon 792 camera operating in framing mode, with framing rates of between 5×10^4 and 1×10^6 frames per second, and those for the projectile penetration experiments using an Imacon 790 in streak mode at 1100 ns mm^{-1}. In addition, an IMCO Ultranac camera, with programmable interframe and exposure times, was used for some of the cyclotol filled target experiments.

EXPERIMENTAL RESULTS

Projectile penetration of steel and copper casings

At the impact velocities in this study, the flat-ended projectiles produced sufficiently high shear strain rates in both metals to shear out a plug of casing, with initially relatively little deformation of the surrounding material. Figure 5 shows a steel projectile penetrating an unfilled copper casing, with the plug (p) clearly visible after penetration. Photographs obtained of the same event with a steel ring were almost identical, and examination of the rings and plugs afterwards confirmed that the failure was very similar in the two cases, although the subsequent deformation around the point of failure was rather greater for the copper rings.

FIGURE 4. SCHEMATIC DIAGRAM OF THE EXPERIMENTAL ARRANGEMENT.

| 0 μs | 5 μs | 10 μs | 15 μs | 20 μs | 25 μs |

FIGURE 5. FLAT-ENDED PROJECTILE IMPACT OF AN UNFILLED COPPER CASING AT 400 m s⁻¹.
(FRAMING RATE 2×10^5 fps)

With pointed projectiles, the strain rates in the metal during penetration are far less than for the flat-ended projectiles. The copper casing undergoes ductile failure and the projectile emerges relatively undamaged. However, the harder steel casing causes the point to be deformed by the initial impact, and it does not survive the penetration, emerging with a rounded profile as shown in Figure 6.

Hemispherical-ended projectiles impacting copper led to predominantly ductile failure on penetration, with a thin layer of copper being stretched across the front of the projectile. On impacting mild steel, the penetration occurred by plugging, with a well-defined plug of steel being removed in a similar manner to that seen with the flat-ended impacts. This may involve a combination of ductile and adiabatic shear failure.

From streak photographs of the penetration of flat-ended projectiles through steel and copper plates, the kinetic energy lost in the process was estimated. Steel projectiles of 2.5g impacting 1.6 mm steel plate with a velocity of 500 m s⁻¹ were estimated to have lost 100 J of kinetic energy. If this energy is deposited adiabatically into a thin region (~ 50 μm) of shear band at the edge of the plug, then an initial temperature rise of greater than 2000 K would be achieved, and although this would be quenched very quickly by conduction into the body of the plug, it might be expected to constitute a viable ignition source for the explosive within. Repeating these tests with explosive sandwiched

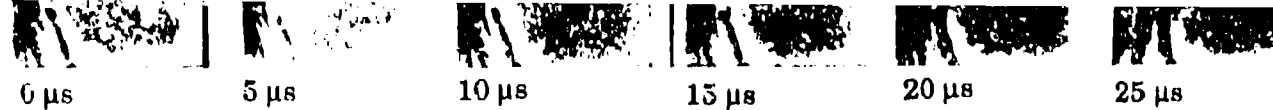| 0 μs | 5 μs | 10 μs | 15 μs | 20 μs | 25 μs |

FIGURE 6. 30° CONE-ENDED PROJECTILE IMPACT OF AN UNFILLED STEEL CASING AT 400 m s⁻¹.
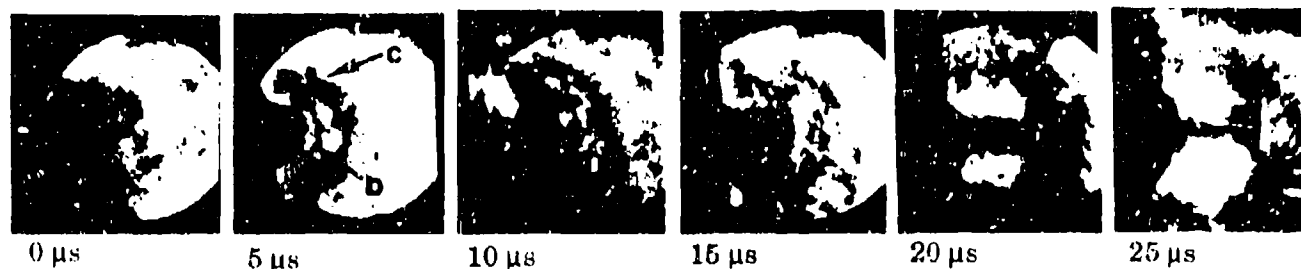(FRAMING RATE 2×10^5 fps)

| 0 μs | 5 μs | 10 μs | 15 μs | 20 μs | 25 μs |

FIGURE 7. FLAT-ENDED PROJECTILE IMPACT OF A COPPER-CASED LX-14 TARGET AT 506 m s⁻¹.
(FRAMING RATE 2×10^5 fps)

between the plates enabled the amount of energy lost by the projectile in passing through the explosive layer to be calculated. For a cast cyclotol composition, this was of the order of $10 - 20$ J mm⁻¹.

Ignition tests on explosive compositions

Table 4 shows threshold flat-ended impact velocities for observed ignition sites for the compositions tested. Values are given for both bare and cased charges. Where ignition was not observed in the high-speed photographs, the composition was usually recovered unburned from the test-box.

Subsequent experiments, to observe different types of ignition mechanism, were mostly restricted to cyclotol, octol and LX-14, which had the lower threshold velocities.

Effect of projectile front-end geometry

Above the threshold velocity for flat-ended projectiles quoted in table 4, similar ignition sites were

readily observed in the cyclotol, octol and LX-14 compositions in the absence of any voids. The main source of ignition appeared to be due to the rapid flow of the explosive around the front of the projectile, with additional reaction sometimes seen associated with the compressive wave moving ahead of the projectile into the surrounding material. Figure 7 shows reaction in a target of LX-14 and the outbreak of burning (b) in the damaged material ahead of the projectile, together with some possible ignition behind the compressive wave front (c). There is further ignition at the failed edge of the casing on impact of the sabot (frame 3). There does not seem to be ignition associated with the initial failure of the casing.

Figure 8 shows a similar impact on a target with cut and removed casing, and the ignition is very similar to that observed in the fully cased sample. The bright flash of light in frame 4 is probably due to compression of air trapped under the end of the casing by the sabot.

Further ignition due to sabot impact is apparent in

TABLE 4. THRESHOLD VELOCITIES FOR FLAT-ENDED IMPACTS

| Composition | Threshold velocity (m s⁻¹) | | | Comments |
	Copper	Steel	B.	
PE4	> 610	> 610	> 610	some ignition with voids
cyclotol	530	550	520	
octol	550	--	540	tests in steel inconclusive
LX-14	400	--	< 500	not yet tested in steel
PBX	> 580	> 580	> 580	not yet tested with voids

0 µs   5 µs   10 µs   15 µs   20 µs   25 µs

FIGURE 8. FLAT-ENDED PROJECTILE IMPACT OF A CUT COPPER-CASED LX-14 TARGET AT 506 m s⁻¹ . (FRAMING RATE 2 × 10⁵ fps)

FIGURE 8. FLAT-ENDED PROJECTILE IMPACT OF A CUT COPPER-CASED LX-14 TARGET AT 506 m s^{-1} . (FRAMING RATE 2×10^5 fps)

0 µs   5 µs   10 µs   15 µs   20 µs   25 µs

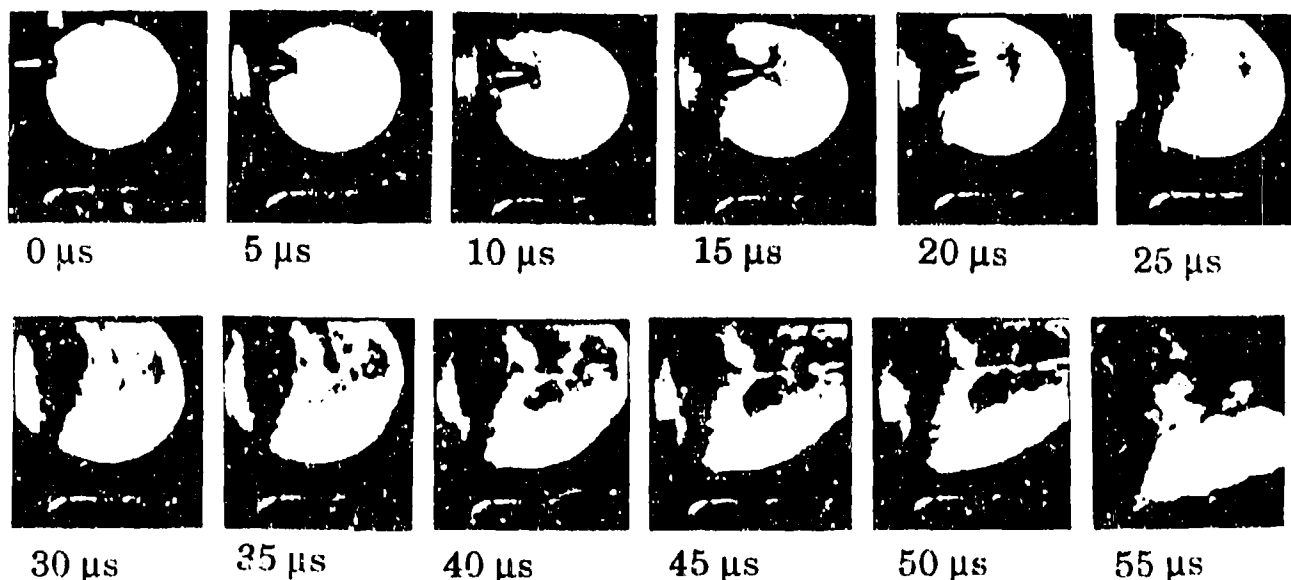30 µs   35 µs   40 µs   45 µs   50 µs   55 µs

FIGURE 9. FLAT-ENDED PROJECTILE IMPACT OF A COPPER-CASED OCTOL TARGET AT 570 m s^{-1} . (FRAMING RATE 2×10^5 fps)

some of the high-speed photographs. Figure 9 is a sequence showing a flat-ended projectile impacting a cased sample of octol, taken using an IMCO Ultranac image converter camera. The sabot impact occurs in frame 3. In the later frames, two regions of burning are clearly visible, one in the damaged material behind the projectile as it crosses the ring and the other across a broader area moving away from the sabot impact.

No ignitions were observed with either pointed or hemispherical-ended projectiles up to the maximum velocities tested (~ 610 m s⁻¹), nor were there any subsequent ignitions due to sabot impact on the already damaged material of the type observed with the flat-ended projectiles.

Effect of voids

Voids of diameter 1.5 mm were introduced into samples of octol and cyclotol at various distances from the point of projectile impact. Since the mechanism by which a void acts as an ignition site is by heating due to shock induced adiabatic collapse of the void, it would be expected that the effectiveness of the void would decrease with distance from the point of impact.

Figure 10 shows the collapse of a void at the casing under the point of impact of a flat-ended projectile on a sample of cyclotol. There is a second, similar void at 12 mm from the point of impact. The heating of the trapped gas in the first void causes it to luminesce, and burning of the surrounding material is apparent in frame 4. The second void does not undergo such strong compression as it is much further away from the point of impact and thus similar luminescence does not occur. Almost all of the explosive was burned in this test, in contrast to those tests in which no voids were present when most of it was recovered, indicating that the first void was the main source of ignition.

Figure 11 shows the effect of a flat-ended projectile impacting a sample of cased octol with a void 3 mm from the point of impact. The projectile is below the surface of the charge and cannot be seen, but the shock wave causing the collapse is visible as a darkening of the surface of the charge, and the collapse of the void is complete, as indicated by the flash of light, roughly 6 µs after the shock wave reaches it. Burning of the surrounding material is visible in the subsequent frames. Impact of the sabot, with further associated reaction, is visible in frame 7.
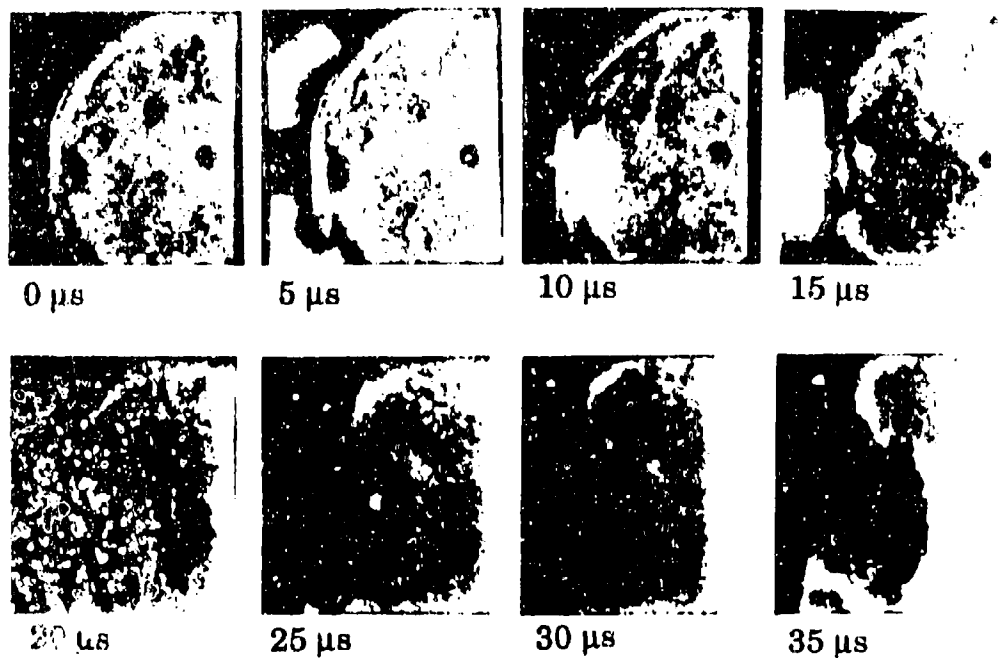
0 μs   5 μs   10 μs   15 μs

20 μs   25 μs   30 μs   35 μs

FIGURE 10. FLAT-ENDED PROJECTILE IMPACT AT 556 m s⁻¹ OF A STEEL-CASED CYCLOTOL TARGET WITH A VOID AT THE SITE OF IMPACT AND SECOND VOID NEAR THE TARGET CENTRE. (FRAMING RATE 2 × 10⁵ fps)

0 μs   2 μs   4 μs   6 μs
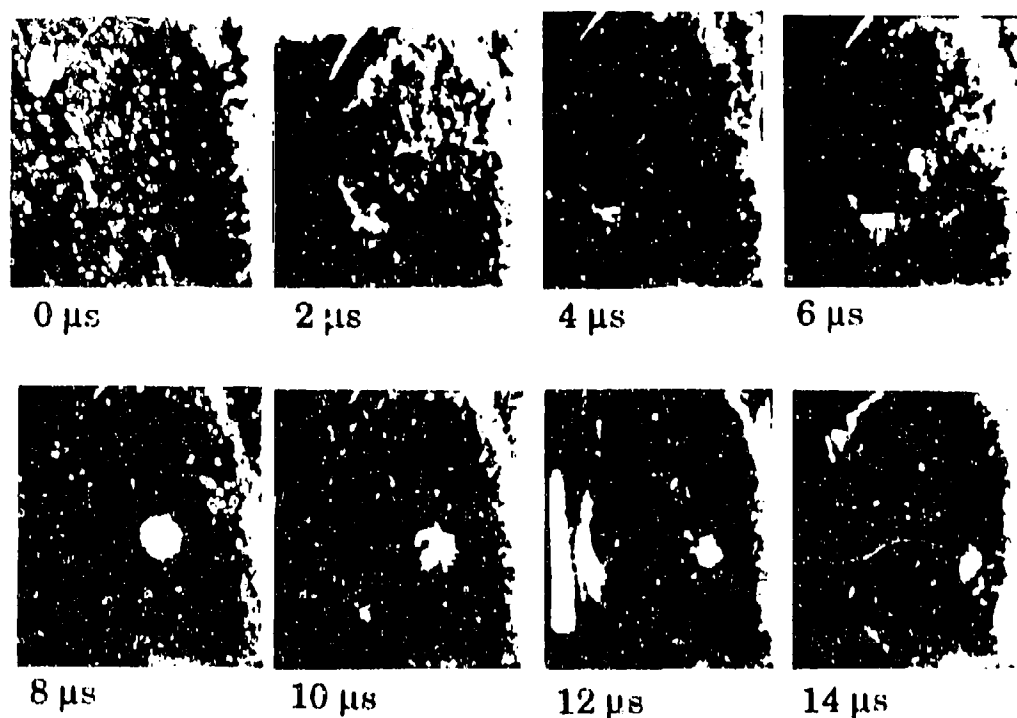
8 μs   10 μs   12 μs   14 μs

FIGURE 11. FLAT-ENDED PROJECTILE IMPACT AT 564 m s⁻¹ OF A STEEL-CASED OCTOL TARGET WITH A VOID 3 mm FROM THE SITE OF IMPACT. (FRAMING RATE 5 × 10⁵ fps)

Impacts with pointed and hemispherical-ended projectiles were far less effective at rapidly collapsing voids, giving little or no light output and no ignitions.

DISCUSSION

High-speed photography of the impact of flat-ended projectiles on copper and steel targets shows that at the impact velocities studied, the projectile penetrates by shearing a plug of metal from the target. Assuming that this is basically an adiabatic shear process, the fracture energy will lead to the edges of the plug being hot, and this might provide a possible source of ignition as the plug is driven through the explosive composition.

Calculation of the temperature rise at the edge of the plug from measurement of the energy lost by the projectile suggests that very high temperatures may be achieved. However, even if quenching of this hot region by conduction of heat into the body of the plug is ignored, which may be justifiable on the timescales involved, the temperature rise in any one small region of the explosive which comes into contact with the edge of the plug will be limited by the duration of that contact. This duration is roughly determined by the impact velocity and the casing thickness if the filling is assumed to be stationary as the plug moves through it; in these experiments it would be of the order of 4 μs.

The high-speed photographs of ignition in LX-14 and octol show that the outbreak of reaction is associated with the leading edge of the projectile or plug. However, there is little difference between the observed ignition mechanisms for cased and uncased explosives, despite the lack of a hot plug in the latter case, which suggests that the source of ignition is more to do with the rapid flow of the material ahead of the projectile. This should be similar for the two situations, though with a bare charge, the projectile will be moving faster through not having been slowed by collision with the casing, and the edges of the leading face will be sharper than the slightly rounded edge of the sheared plug. Both of these effects will tend to produce higher material flow velocities in the bare charge than in the cased charge for any given impact velocity.

The threshold velocity for ignition of octol appeared to be lower for copper casing than for steel, despite the higher thermal conductivity of copper, which should lead to a much more rapid cooling of the edges of the plug and make it less effective as a source of ignition. This also suggests that the hot plug may not be the predominant source of ignition in these impacts.

Changing the front end of the projectile to a conical shape alters the nature of the casing failure, the strength and divergence of the shock wave which is transmitted to the explosive through the casing, and reduces the flow velocity of the material around the projectile once it has entered the explosive. The rapid adiabatic shear failure of the casing seen with the flat-ended projectile is absent; in the case of the copper casing, the projectile penetrates reasonably intact by ductile failure of the metal whereas with steel, the front of the projectile is flattened by the impact and it is quite blunt when it reaches the explosive. All these factors should reduce the effectiveness of the projectile as an ignition source, and this was indeed found to be the case, with no observed ignitions up to 610 m s⁻¹. Hemispherical-ended projectiles, which caused ductile failure in copper but shear failure in steel, also failed to produce ignitions even in steel casings, again indicating that the fractured plug may be less important than the material flow.

These observations are not inconsistent with the calculations of Liang *et al.*[5] who showed that the temperature rise in an explosive due to the shear and flow of material ahead of a projectile could be expected to produce local temperatures high enough to cause ignition.

CONCLUSIONS

High-speed photography of projectile impacts on cased and uncased charges has permitted direct observation of the ignition sites within the explosive. These observations suggest that the rapid flow of material around the front of the projectile may be more important as an ignition source than the hot fracture surface of the plug of casing which is sheared out in the course of casing penetration.

ACKNOWLEDGEMENTS

REFERENCES

1. Dewey, J. and Slade, D., "High order initiation of two military explosives by projectile impact", ARBRL-TB-1021, 1957, Ballistic Research Laboratory, Aberdeen Proving Ground, MD.

2. Brown, S. and Whitbread, E., "The initiation of detonation by shock waves of known intensity and duration", Colloque Internationale C.N.R.S., Les Ondes de Detonation, editions Du Centre National De la Recherche Scientifique 15,Paris, 1962, p.97.

3. Howe, P.M., Watson, J. and Frey, R.B.,' "Response of confined explosive charges by projectile impact", Seventh Symposium (International) on Detonation, Annapolis, MD, 1981, pp. 1048-1054.

4. Cook, M.D., Haskins, P.J. and James, H.R., "Projectile impact initiation of explosive charges", Ninth Symposium (International) on Detonation, Portland, Oregon, 1989, pp.1441 1450.

5. Liang, D., Chou, P.C. and Hashemi, J., "Shock and shear effects in explosives due to impact", Shock compression of condensed matter, Williamsburg, Virginia, 1991, pp. 345-348.

6. Haskins, P.J., Cook, M.D. and James, H.R., "Effect of case thickness and projectile geometry on the shock initiation threshold for a given explosive", AGARD Conference preprints, Bonn, Germany, 1991, paper 18.

7. Boggs, T.L. et al, "Hazards of energetic materials and their relation to munitions survivability", AGARD conference preprints, Bonn, Germany, 1991, paper 16.